

MEASUREMENT OF THE BRANCHING FRACTION
FOR THE DECAY $K_L^0 \rightarrow \pi^+\pi^-e^+e^-$
IN THE HIGH $M_{\pi\pi}$ INVARIANT MASS REGION

A Dissertation

Presented to

The Faculty of the Department of Physics
The College of William and Mary in Virginia

In Partial Fulfillment

Of the Requirements for the Degree of
Doctor of Philosophy

by

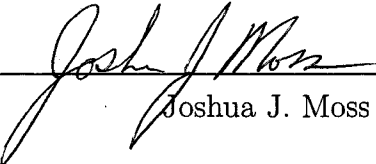
Joshua J. Moss

May, 2007

APPROVAL SHEET

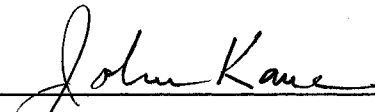
This dissertation is submitted in partial fulfillment of
the requirements for the degree of

Doctor of Philosophy

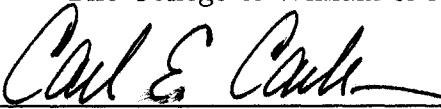


Joshua J. Moss

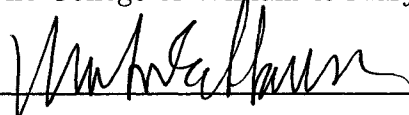
Approved by the Committee, April 2007



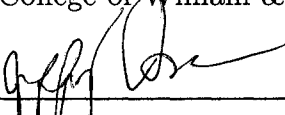
Committee Chair
Professor John Kane, Physics
The College of William & Mary



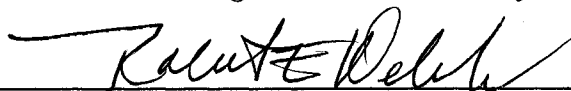
Professor Carl Carlson, Physics
The College of William & Mary



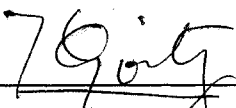
Emeritus Professor Morton Eckhause, Physics
The College of William & Mary



Assistant Professor Jeffrey Nelson, Physics
The College of William & Mary



Chancellor Professor Robert Welsh, Physics
The College of William & Mary



Associate Professor Jose Goity, Physics
Hampton University

ABSTRACT

A measurement of the branching fraction for the rare decay $K_L^0 \rightarrow \pi^+\pi^-e^+e^-$ was performed using data collected from experiment E871 which ran at the AGS of Brookhaven National Laboratory. Analysis of the data revealed 27.7 ± 7.4 signal events in the signal region, $0.4905 \text{ GeV} < M_{\pi\pi ee} < 0.505 \text{ GeV}$ together with 13.3 ± 3.7 background events. The branching fractions of $(8.5_{\pm 1.0}^{\pm 2.3(stat)}) \times 10^{-6}$ using the phenomenological model acceptance and $(2.3_{\pm 0.3}^{\pm 0.6(stat)}) \times 10^{-6}$ using the chiral perturbation model represent the first measurements for $K_L^0 \rightarrow \pi^+\pi^-e^+e^-$ in the dipion invariant mass region $0.475 \text{ GeV} < M_{\pi\pi} < 0.497 \text{ GeV}$. These results support the prediction of chiral perturbation theory rather than that of the phenomenological model.

TABLE OF CONTENTS

| | Page |
|---|-----------|
| Abstract | iii |
| List of Tables | vii |
| List of Figures | ix |
| Acknowledgments | xvi |
| CHAPTER | |
| I Introduction and Motivation | 2 |
| 1 Introduction | 3 |
| 2 Theoretical Motivation | 6 |
| 2.1 Overview | 6 |
| 2.2 Neutral Kaons | 6 |
| 2.3 CP Violation | 9 |
| 2.4 $K_L^0 \rightarrow \pi^+\pi^-e^+e^-$ Models | 10 |
| 2.4.1 Phenomenological Model | 10 |
| 2.4.2 Chiral Perturbation Model | 21 |
| II Hardware and Software | 25 |
| 3 BNL E871 Detector | 26 |
| 3.1 Overview | 26 |

| | | |
|----------|--|-----------|
| 3.2 | Neutral Beam Production | 27 |
| 3.2.1 | Primary Proton Beam | 27 |
| 3.2.2 | Production Target | 30 |
| 3.2.3 | Neutral Beam Creation and Colimation | 32 |
| 3.2.4 | Decay Tank | 33 |
| 3.3 | Spectrometer | 35 |
| 3.3.1 | Straw Drift Chambers | 35 |
| 3.3.2 | Momentum Analyzing Magnets | 38 |
| 3.3.3 | Drift Chambers | 40 |
| 3.3.4 | Beam Stop | 41 |
| 3.4 | Trigger Counters and Particle Identification | 43 |
| 3.4.1 | Trigger Scintillator Counters | 44 |
| 3.4.2 | Cerenkov Counter | 47 |
| 3.4.3 | Lead Glass Calorimeter | 49 |
| 3.4.4 | Muon Identification | 52 |
| 3.4.5 | Muon Rangefinder | 56 |
| 4 | Trigger System | 57 |
| 4.1 | Overview | 57 |
| 4.2 | Level 0 | 58 |
| 4.3 | Level 1 | 60 |
| 4.4 | Level 3 | 61 |
| 5 | Offline Analysis | 63 |
| 5.1 | Overview | 63 |
| 5.2 | Pattern Recognition | 64 |
| 5.3 | Track-Counter Association | 69 |
| 5.4 | Event Fitting | 69 |

| | | |
|---|---|------------|
| 5.4.1 | FT Fitter | 70 |
| 5.4.2 | QT Fitter | 72 |
| III Branching Fraction Measurement | | 75 |
| 6 | Monte Carlo Studies | 76 |
| 6.1 | Overview | 76 |
| 6.2 | $K_L^0 \rightarrow \pi^+\pi^-e^+e^-$ Event Signature | 77 |
| 6.3 | Primary Pion Tracks | 79 |
| 6.4 | Partial Tracking Stub Search | 95 |
| 6.5 | Acceptances | 111 |
| 7 | Background | 119 |
| 7.1 | $K_L^0 \rightarrow \pi^+\pi^-\pi^0$ | 119 |
| 7.2 | Pileup Events | 120 |
| 7.3 | $K_L^0 \rightarrow \pi^+\pi^-\gamma$ | 122 |
| 7.4 | $K_L^0 \rightarrow \ell^+\ell^-\gamma$ and $K_L^0 \rightarrow (\ell^+\ell^-)(\ell^+\ell^-)$ | 125 |
| 8 | Event Counting | 130 |
| 8.1 | Overview | 130 |
| 8.2 | Normalization Sample | 130 |
| 8.3 | $K_L^0 \rightarrow \pi^+\pi^-e^+e^-$ Sample | 138 |
| 9 | Results | 151 |
| 9.1 | Branching Fraction Measurement | 151 |
| 9.2 | Conclusions | 155 |
| APPENDIX A | | |
| | E871 Collaboration | 157 |
| BIBLIOGRAPHY | | 158 |
| Vita | | 161 |

LIST OF TABLES

| Table | | Page |
|-------|---|------|
| 2.1 | $K_L^0 \rightarrow \pi^+\pi^-e^+e^-$ phenomenological model parameters extracted from the full data set of KTeV [1] | 20 |
| 3.1 | Transverse momentum for K_L decay modes | 40 |
| 3.2 | Threshold momenta for Cerenkov Radiation in Hydrogen | 48 |
| 3.3 | Muon range stack material placement and stopping momentum by detector plane | 54 |
| 6.1 | Particle identification routine requirements for full tracks in the E871 detector. | 93 |
| 6.2 | Cut values and efficiencies associated with a good pion track in the spectrometer (FT fitter). | 94 |
| 6.3 | Cut values and efficiencies associated with a good pion track in the spectrometer (QT fitter). | 94 |
| 6.4 | Cut values and efficiencies for the four-body reconstruction in each fitter and model. | 111 |
| 6.5 | Acceptance summary for events reconstructed using the FT and QT fitter. | 118 |
| 7.1 | Branching fractions for the decay channels used in the pileup event simulation. | 122 |

| | | |
|-----|--|-----|
| 7.2 | Properties of materials prior to the second layer of straws in SDC1 for use in pair production calculations. | 127 |
| 7.3 | Properties of the leptonic background decay modes along with the expected number of background events for each. | 128 |
| 8.1 | Selection criteria for reconstructing normalization events. | 132 |
| 8.2 | $K_L^0 \rightarrow \pi^+\pi^-$ events in the normalization sample when reconstructed with the FT and QT fitters. | 137 |
| 8.3 | The number of background events in the $K_L^0 \rightarrow \pi^+\pi^-e^+e^-$ FT candidate event sample extracted using the fits of Figures 8.8 and 8.9. | 148 |
| 8.4 | The number of background events in the $K_L^0 \rightarrow \pi^+\pi^-e^+e^-$ QT candidate event sample extracted using the fits of Figures 8.10 and 8.11. | 149 |
| 9.1 | The quantities used in the branching fraction calculations and their statistical uncertainty. | 153 |

LIST OF FIGURES

| Figure | Page |
|--|------|
| 2.1 Production of a K^0 and a Λ^0 via the strong interaction. | 7 |
| 2.2 K^0 and \bar{K}^0 shared final states and $\Delta S = 2$ mixing | 8 |
| 2.3 Feynman diagrams contributing to the phenomenological model of $K_L^0 \rightarrow \pi^+\pi^-e^+e^-$ | 13 |
| 2.4 Definitions of the kinematic variables used to describe the phase space of the decay $K_L^0 \rightarrow \pi^+\pi^-e^+e^-$ | 16 |
| 2.5 The differential decay spectrum $\frac{d\Gamma}{dM_{\pi\pi}}$ in the phenomenological model | 18 |
| 2.6 Experimental $M_{\pi\pi}$ distributions from KTeV and NA48 | 19 |
| 2.7 Tree-level Feynman diagrams contributing to the $F_{\pm}^{(1)}$ term of the chiral perturbation form factors. | 23 |
| 2.8 Monte Carlo Differential decay spectrum using the chiral perturbation model of $K_L^0 \rightarrow \pi^+\pi^-e^+e^-$ | 24 |
| 3.1 E871 experimental hall diagram. | 28 |
| 3.2 An overhead schematic of the E871 experimental hall. | 29 |
| 3.3 Brookhaven National Lab AGS | 30 |
| 3.4 E871 Production target and Base | 32 |
| 3.5 Side view of the E871 neutral beamline. | 34 |
| 3.6 E871 two-armed magnetic spectrometer. | 36 |

| | | |
|------|---|----|
| 3.7 | The layout of the straw drift chambers with x and y -viewing straws. . . | 38 |
| 3.8 | The Dipole Magnets D02 and D03. | 39 |
| 3.9 | The cross section of the x -viewing layers of a traditional drift chamber. | 41 |
| 3.10 | An x - z cross section of the neutral beam stop. | 42 |
| 3.11 | Single channel hit rates for the drift chambers | 43 |
| 3.12 | Focusing of a two-body event in the E871 spectrometer | 45 |
| 3.13 | The trigger scintillating hodoscope | 45 |
| 3.14 | A drawing of the layout of TSC2. | 46 |
| 3.15 | The light cone produced through the Cerenkov effect | 47 |
| 3.16 | The E871 threshold Cerenkov counter external and internal geometry. | 49 |
| 3.17 | The E871 lead-glass calorimeter with an external cooling system. . . . | 50 |
| 3.18 | Examples of electromagnetic and hadronic showers. | 51 |
| 3.19 | The muon hodoscope and muon rangefinder. | 52 |
| 3.20 | The layout of the six planes of scintillators used in the muon hodoscope. | 55 |
| 3.21 | A cross section of an 8-channel extruded aluminum segments used in the 52 proportional counters planes of the muon rangefinder. | 56 |
| 4.1 | E871 DAQ system overview. | 59 |
| 4.2 | An example of a L0/L1 trigger. | 60 |
| 5.1 | A Flow chart for the stages in the E871 offline analysis software. . . | 65 |
| 5.2 | An Illustration of three clusters in a drift chamber which demonstrate the meaning of “geometrically contiguous”. | 66 |
| 5.3 | An illustration of 5 segments (red cells) inside 1 cluster (yellow cells). Each segment is mutually exclusive in that no segment can be fully contained in another. | 67 |

| | | |
|------|---|----|
| 6.1 | Possible $K_L^0 \rightarrow \pi^+\pi^-e^+e^-$ events accepted into the front half of the spectrometer. | 79 |
| 6.2 | FT fitter χ_T^2 distributions for $K_L^0 \rightarrow \pi^+\pi^-$ and $K_L^0 \rightarrow \pi^+\pi^-e^+e^-$ with K_L^0 form factors are presented. | 81 |
| 6.3 | QT fitter χ_T^2 distributions for $K_L^0 \rightarrow \pi^+\pi^-$ and $K_L^0 \rightarrow \pi^+\pi^-e^+e^-$ with K_L^0 form factors are presented. | 82 |
| 6.4 | Pion momentum distributions for $K_L^0 \rightarrow \pi^+\pi^-$ and $K_L^0 \rightarrow \pi^+\pi^-e^+e^-$ with K_L^0 form factors calculated using the FT fitter are presented. . . | 84 |
| 6.5 | Pion momentum distributions for $K_L^0 \rightarrow \pi^+\pi^-$ and $K_L^0 \rightarrow \pi^+\pi^-e^+e^-$ with K_L^0 form factors calculated using the QT fitter are presented. . . | 85 |
| 6.6 | Top: The neutral beam profile from the platinum target is shown as defined by the brass collimators. | 87 |
| 6.7 | Angular vertex position distributions for v_x , v_y and v_z calculated using the FT fitter are shown for $K_L^0 \rightarrow \pi^+\pi^-$ and $K_L^0 \rightarrow \pi^+\pi^-e^+e^-$ with the cut values represented by the dashed lines. | 88 |
| 6.8 | Angular vertex position distributions for v_x , v_y and v_z calculated using the QT fitter are shown for $K_L^0 \rightarrow \pi^+\pi^-$ and $K_L^0 \rightarrow \pi^+\pi^-e^+e^-$ with the cut values represented by the dashed lines. | 89 |
| 6.9 | The distribution of the FT-reconstructed vertices in the v_x - v_y plane for the normalization Monte Carlo. This plot is typical of results for the QT-fitted events as well as for the two models of signal Monte Carlo. | 90 |
| 6.10 | The χ_{vtx}^2 distribution of the FT-reconstructed vertices for the pion tracks from Monte Carlo data is shown. | 91 |
| 6.11 | The χ_{vtx}^2 distribution of the QT-reconstructed vertices for the pion tracks from Monte Carlo data is shown. | 92 |
| 6.12 | A simplified example of the search for stub candidates with three extra segments found in SDC1 and two extra segments in SDC2. . . | 96 |
| 6.13 | An illustration of the collinearity angles and vectors used to calculate the momentum of the e^+e^- momentum sum. | 97 |

| | | |
|------|--|-----|
| 6.14 | The Monte Carlo distribution for the momentum carried by the electron and positron in the lab frame is shown in (a). The momentum difference, $ p_{e^+}^{\vec{}} - p_{e^-}^{\vec{}} $, for all events in (a) is shown in (b). | 98 |
| 6.15 | An illustration of the vectors used to calculate the DOCA value of a track to a point using the minimization technique. | 99 |
| 6.16 | Distributions for the number of partial track candidates per event and the e^+/e^- to vertex DOCA for each are shown for the phenomenological model using the FT fitter. Plots using the chiral perturbation model and the QT fitter show similar results. | 101 |
| 6.17 | Stub to vertex DOCA of the stub candidate with the smallest stub to vertex DOCA for each event. | 102 |
| 6.18 | Stub to vertex DOCA of the stub candidate with the second smallest stub to vertex DOCA for each event. | 103 |
| 6.19 | An illustration of the $\pi^+\pi^-$ and e^+e^- decay planes formed by the momentum vectors of the $\pi^+\pi^-$ and e^+e^- pairs, respectively. | 104 |
| 6.20 | The stub to primary decay plane angle for the best two stub candidates using the FT fitter. | 106 |
| 6.21 | The stub to primary decay plane angle for the best two stub candidates using the QT fitter. | 107 |
| 6.22 | Stub to stub opening angle between the best two stub candidate for each event. | 108 |
| 6.23 | Stub to stub DOCA between the best two stub candidate for each event. | 110 |
| 6.24 | Invariant mass versus transverse momentum distributions for Monte Carlo events which pass all two and four body cuts are shown. | 114 |
| 6.25 | Invariant mass distributions for Monte Carlo events which pass all two and four body cuts are shown. | 115 |
| 6.26 | Invariant mass versus transverse momentum distributions for Monte Carlo $K_L^0 \rightarrow \pi^+\pi^-$ events which pass all two-body cuts are shown in (a) and (c). (b) and (d) are the projections of the distributions in (a) and (c) onto the mass axis. | 116 |

| | | |
|------|--|-----|
| 6.27 | Transverse momentum squared distributions for Monte Carlo $K_L^0 \rightarrow \pi^+\pi^-$ events which pass all two-body cuts are shown for the FT and QT fitters. | 117 |
| 7.1 | Invariant mass spectrum for pileup background events which pass the $K_L^0 \rightarrow \pi^+\pi^-e^+e^-$ acceptance criteria. | 123 |
| 7.2 | $K_L^0 \rightarrow \pi^+\pi^-\gamma$ background characteristics | 125 |
| 7.3 | Fractional Interaction lengths and pair production probabilities for photons in the material prior to the second layer of x-viewing straws in SDC1. | 126 |
| 7.4 | The Photon energy distribution for $K_L^0 \rightarrow \pi^+\pi^-\gamma$ in the lab frame, from Geant3 MC. | 127 |
| 8.1 | Mis-identified $K_{\mu 3}$ and K_{e3} reconstruction under a $\pi^+\pi^-$ hypothesis. | 133 |
| 8.2 | Background subtraction results for the $K_L^0 \rightarrow \pi^+\pi^-$ sample analyzed with the FT fitter. | 135 |
| 8.3 | Background subtraction results for the $K_L^0 \rightarrow \pi^+\pi^-$ sample analyzed with the QT fitter. | 136 |
| 8.4 | Candidate samples for the FT and QT fitters. None of the events in the samples are part of the normalization sample and have passed two and four-body selection requirements as well as particle ID. | 138 |
| 8.5 | The pileup event sample from Monte Carlo plotted against four-body invariant mass was fit using three functions and three separate bin widths. | 140 |
| 8.6 | The pileup event sample from Monte Carlo plotted against four-body invariant mass was fit using three functions and three separate bin widths. | 141 |
| 8.7 | Gaussian fits to the $K_L^0 \rightarrow \pi^+\pi^-e^+e^-$ Monte Carlo data for each fitter and model are shown. | 143 |
| 8.8 | The candidate event sample for the FT fitter plotted against four-body invariant mass was fit to the distribution defined in Eq. (8.7). | 144 |

- 8.9 The candidate event sample for the FT fitter plotted against four-body invariant mass was fit to the distribution defined Eq. (8.7). . . . 145
- 8.10 The candidate event sample for the QT fitter plotted against four-body invariant mass was fit to the distribution defined in Eq. (8.7). . 146
- 8.11 The candidate event sample for the QT fitter plotted against four-body invariant mass was fit to the distribution defined in Eq. (8.7). . 147

DEDICATION

For Melanie

“Where there is love, distance doesn’t matter.”

- Mata Amritanandamayi

ACKNOWLEDGMENTS

The work presented here was made possible by the hard work and dedication of many individuals, most of whom I have not had the opportunity to thank in person. I would like to express my gratitude to the all of those involved in the E871 experiment: faculty, staff, post-docs, graduate students, and undergraduate students from the University of Texas, Stanford University, the University of California at Irvine, the University of Richmond, and the College of William and Mary. The E871 data was obtained with the help of George Irwin at SLAC.

Special thanks to John Kane, my thesis advisor, for his support and encouragement through the years of lost research projects and difficult analysis. He has given me the knowledge and guidance necessary to complete this work. I would like to thank Morton Eckhause for the tireless help he has given me in my time at the College of William and Mary. He has shown incredible patience through many hours of revisions that helped shape this document. The many conversations I have had with Jeff Nelson have helped make this analysis a success and have made me a better researcher. For which, I am very grateful.

Andrew Norman has spent an incredibly generous amount of time mentoring me on all things related to E871 and to physics in general. I have benefited greatly from the hours spent on the phone and in emails. This work was made easier by his knowledge and support. For all of this, thank you.

I would like to express my thanks to my family and friends for all of their encouragement during my time as a graduate student. My parents, Carol Slagle and Dan Moss, have given me inspiration and have taught me to believe in myself. Their love and support have made me the person I am today.

Finally, my loving thanks to Melanie. She has been the rock on which my life has been built since our undergraduate days together at Hiram College. Through all my declarations that I would be finishing “soon”, she has shown infinite love, patience, and emotional support. A thank you could never truly express the gratitude I feel for everything she does for me.

MEASUREMENT OF THE BRANCHING FRACTION
FOR THE DECAY $K_L^0 \rightarrow \pi^+\pi^-e^+e^-$
IN THE HIGH $M_{\pi\pi}$ INVARIANT MASS REGION

Part I

Introduction and Motivation

CHAPTER 1

Introduction

This thesis describes the measurement of the branching fraction for the rare decay $K_L^0 \rightarrow \pi^+\pi^-e^+e^-$ in the phase space for which the pion pair has greater than 0.475 GeV of the invariant mass. Interest in this decay mode began in the late 1960's when it was predicted by Dolgov and Ponomarev [2] that a CP violating effect would be manifested as an asymmetry in the angle between the $\pi^+\pi^-$ and e^+e^- decay planes. A phenomenological model was developed based on a one photon intermediate state, $K_L^0 \rightarrow \pi^+\pi^-(\gamma^* \rightarrow e^+e^-)$. Predictions from this model have been presented in papers by Sehgal *et al.* [3], [4] in the early 1990's. A second model based on the framework of chiral perturbation theory (χ PT) has also made predictions for the branching fraction in this channel. This model shows an enhancement to the decay rate in the high dipion invariant mass region compared with the phenomenological model. An experimental measurement of the branching ratio in this phase space region can be used as a test of the predictive powers of the two models as the detector acceptances are model-dependent.

The first measurement of the $K_L^0 \rightarrow \pi^+\pi^-e^+e^-$ branching fraction was based on 37 events observed by the KTeV collaboration at the Fermi National Laboratory

in 1998 [5]. Further observations by KTeV [1], the NA48 experiment at CERN [6], and the E162 experiment at KEK brought the total event sample for this decay channel to 6175 events. These experiments were designed to accept events throughout the majority of the dipion invariant mass spectrum but had small acceptances above $M_{\pi\pi} > 0.475$ GeV. The world average branching fraction determined from this sample used acceptances calculated from the phenomenological model. The world average and the theoretical predictions agree for dipion invariant mass region investigated, $0.279 < M_{\pi\pi} < 0.475$ GeV. A branching fraction based upon the predictions of the chiral perturbation model was not evaluated for the 6175 events in the world sample.

Experiment E871 was performed at the Alternating Gradient Synchrotron (AGS) at the Brookhaven National Laboratory in 1995 and 1996 and included a collaboration of scientists from five universities (Appendix A contains a list of researchers, institutions and publications). The detector was designed to search for the rare leptonic decays $K_L^0 \rightarrow \mu^+\mu^-$ [7] and $K_L^0 \rightarrow e^+e^-$ [8], and for the forbidden decay $K_L^0 \rightarrow \mu^\pm e^\mp$ [9] using a two-armed spectrometer and particle identification system. Although the acceptance was maximized for two-body decays, three and four body decays can be measured if two of the decay products carry the majority of the invariant mass. The final data set from E871 was reduced such that all events contained a pair of tracks that carried at least 0.475 GeV of the kaon's invariant mass. Thus, the $K_L^0 \rightarrow \pi^+\pi^-e^+e^-$ branching fraction measurement was limited to the region least sensitive in KTeV, NA48, and E162.

The work described here was further motivated by a measurement of the branching fraction for $K_L^0 \rightarrow \mu^+\mu^-e^+e^-$ in 2004 by A. Norman on E871[10]. In that work, an enhancement to the decay rate in the high $\mu^+\mu^-$ invariant mass region was observed, which was consistent with the chiral perturbation model for a four-lepton final state. It was also demonstrated that a four-body decay event could be recon-

structed from the two-body data set of E871.

This thesis is broadly organized into three parts. The first part includes the introduction and the theoretical overview which includes the kaon phenomenology and a description of the $K_L^0 \rightarrow \pi^+\pi^-e^+e^-$ decay models. In the second part, the hardware and software that was built to perform the E871 experiment is described in detail. The final part provides information on the components necessary to perform the branching fraction calculations. This includes a chapter on the Monte Carlo simulation of the phenomenological and chiral perturbation models, a chapter on the analysis of the signal and normalization samples, and a chapter with the conclusions.

CHAPTER 2

Theoretical Motivation

2.1 Overview

In this chapter, the theoretical basis for this measurement is given. The first sections comprise a summary of the important properties of the neutral kaon system. Extensive reviews on the history and phenomenology of the neutral kaon and CP violation can be found in [11],[12], and [13]. Following this summary, the phenomenological and chiral perturbation models are described for the $K_L^0 \rightarrow \pi^+\pi^-e^+e^-$ decay.

2.2 Neutral Kaons

In 1946, the neutral kaon was discovered by G. Rochester and C. Butler [14] in a cosmic-ray cloud chamber experiment. Two charged tracks, now known to be pions, were observed to originate from a neutral particle whose mass was approximately 900 times the mass of the electron. This was the first observation of a hadron which we now know contains a quark other than the up or down quark. The concepts developed from this and subsequent discoveries of heavier hadrons form the basis of the quark model.

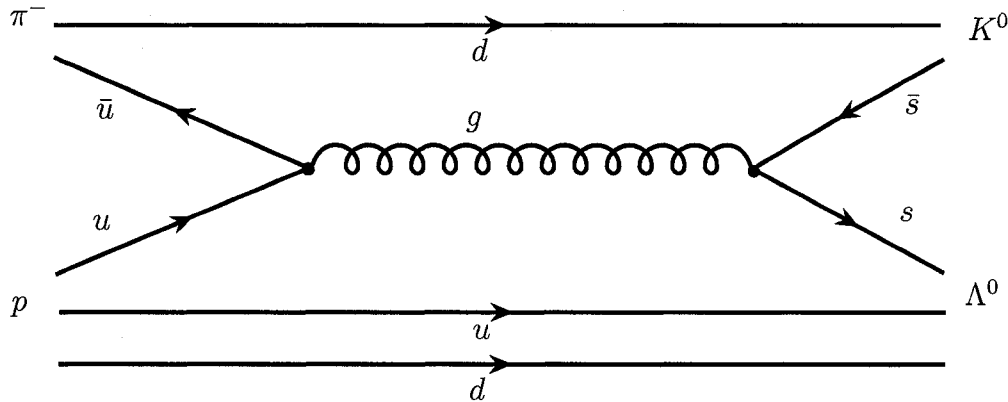


Figure 2.1: Production of a K^0 and a Λ^0 via the strong interaction.

There are two forms of the neutral kaon, the K^0 and its antiparticle, the \bar{K}^0 . In the quark model they are described by

$$|K^0\rangle = |\bar{s}d\rangle \quad S = +1 \quad (2.1)$$

$$|\bar{K}^0\rangle = |s\bar{d}\rangle \quad S = -1. \quad (2.2)$$

Both states have the same mass, charge, spin, and parity but are distinguished by their strangeness quantum number S . The strangeness of a hadron is defined by its strange quark content S , with $+1$ defining a particle with one anti-strange quark. The strong interaction conserves strangeness. In order to produce particles with $S = 1$, an associated particle must also be produced with $S = -1$. A typical process by which this occurs is

$$\pi^- + p \rightarrow \Lambda + K^0. \quad (2.3)$$

The Feynman diagram for this process can be found in Figure 2.1. This process is the dominant method of producing neutral kaons for E871.

Due to the strangeness-conserving nature of strong and electromagnetic interactions, the K^0 and \bar{K}^0 are unable to decay via those forces, as they are the lightest

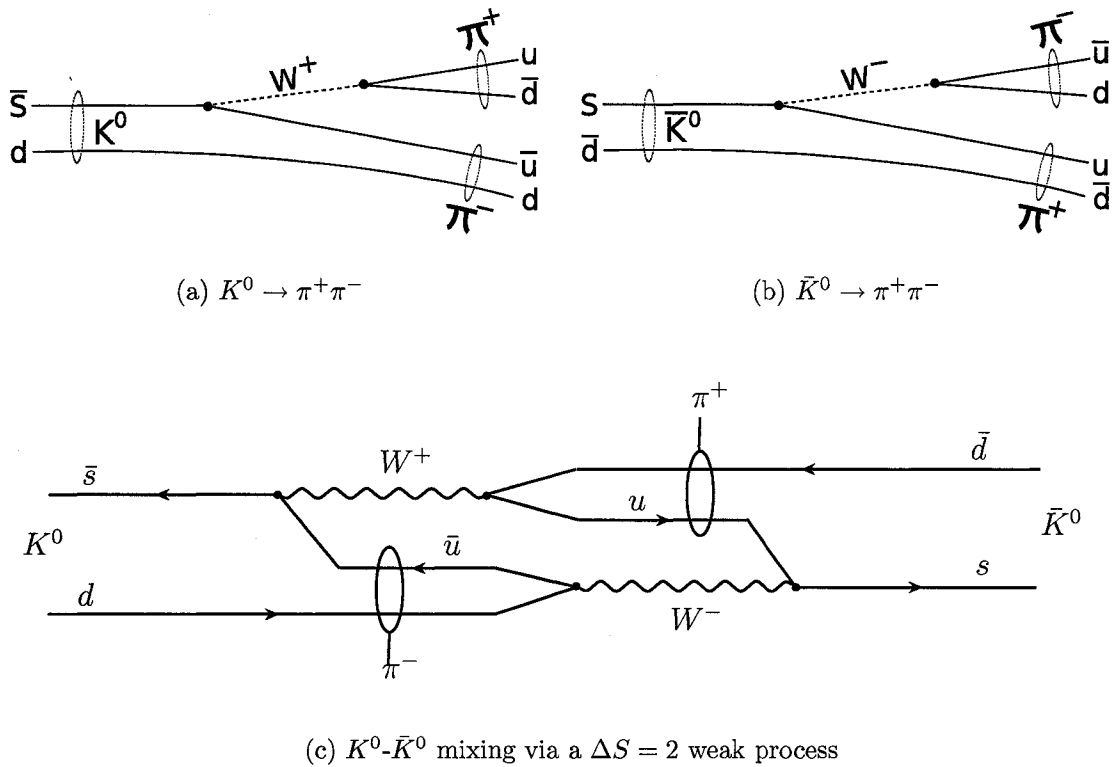


Figure 2.2: Since K^0 (a) and \bar{K}^0 (b) share final states, mixing between the two is possible through the second order weak interaction shown in (c).

mesons containing a strange quark. The weak force does not conserve strangeness, and thus K^0 and \bar{K}^0 decays can proceed by $\Delta S = 1$ channels. As shown in Figures 2.2(a) and 2.2(b), both neutral kaons can decay into the same final states. This leads to second-order weak interaction processes which allow K^0 and \bar{K}^0 to mix (Figure 2.2(c)). For an observed final state, the initial state which created it cannot be known with certainty, and thus the experimentally observed particles must be a linear combination of the $|K^0\rangle$ and $|\bar{K}^0\rangle$ states.

Weak interactions do not conserve parity (\hat{P}), as first confirmed in the beta decay of Co^{60} [15], nor do they conserve charge conjugation (\hat{C}) due to the explicit handedness of the neutrino but, to an approximate extent, the combined symmetry operation of $\hat{P}\hat{C}$ is conserved in the weak processes. K^0 and \bar{K}^0 are not eigenstates

of CP,

$$\text{namely, } \text{CP} |K^0\rangle = -|\bar{K}^0\rangle \quad \text{and} \quad \text{CP} |\bar{K}^0\rangle = -|K^0\rangle. \quad (2.4)$$

We can form linear combinations which are CP eigenstates:

$$|K_1^0\rangle = \frac{1}{\sqrt{2}}(|K^0\rangle - |\bar{K}^0\rangle) \quad \text{with} \quad \text{CP} |K_1^0\rangle = +|K_1^0\rangle \quad (2.5)$$

$$|K_2^0\rangle = \frac{1}{\sqrt{2}}(|K^0\rangle + |\bar{K}^0\rangle) \quad \text{with} \quad \text{CP} |K_2^0\rangle = -|K_2^0\rangle. \quad (2.6)$$

If CP invariance is assumed to hold for weak interactions, the decays of K_1^0 and K_2^0 can be distinguished by noting the parity of the final state. In pionic decays, a final state of 2π 's must have originated from a K_1^0 since the pion has an intrinsic parity of -1, whereas a final state of 3π 's must have originated from a K_2^0 . By examining the allowed phase space for each final state (215 MeV/c for 2π and 78 MeV/c for 3π), it was predicted that $\tau_{K_1^0} < \tau_{K_2^0}$ by Gell-Mann and Pais [16] and later confirmed in experiment by Lande *et al.* [17].

2.3 CP Violation

In 1964, J. Christenson, J. Cronin, V. Fitch, and R. Turlay detected one $K_2^0 \rightarrow \pi^+\pi^-$ event in 500 decays of the long-lived neutral kaon [18]. Up to this point, the CP eigenstates were thought to be equivalent to the weak eigenstates due to CP invariance in the weak interaction. Due to the fact that the violation is at such a small level ($\sim 2 \times 10^{-3}$), the weak states are expected to differ from the CP states by only a small amount which can be accounted for by including a small admixture of the opposite CP state. The new states are called K_S^0 and K_L^0 and are defined as

$$|K_S^0\rangle \equiv |K_1^0\rangle + \epsilon |K_2^0\rangle \quad (2.7)$$

$$|K_L^0\rangle \equiv |K_2^0\rangle + \epsilon |K_1^0\rangle, \quad (2.8)$$

where the normalization has been ignored and $\epsilon \approx 2.284 \times 10^{-3}$ [19]. CP violation can originate from two sources in the neutral kaon system. In *indirect* CP violation, the weak state decays via the admixture of the minority CP state for that system. For example in a $K_L^0 \rightarrow \pi^+\pi^-$ event, CP = +1 final state can be reached if the decay occurs through the $\epsilon|K_1^0\rangle$ sector of the initial K_L^0 state. In *direct* CP violation, ϵ' is non-zero if either the K_1^0 or K_2^0 decays to a final state of opposite CP. The ratio ϵ'/ϵ has been measured in $K \rightarrow \pi\pi$ decays [20, 21, 22] and is given by

$$\frac{\epsilon'}{\epsilon} = (1.72 \pm 0.18) \times 10^{-3} \quad [19]. \quad (2.9)$$

The small level at which direct CP violation contributes, it will not be relevant to this study and therefore, any further references to CP violation will be for the indirect contribution only.

The degree to which CP violation contributes is found by measuring the amplitude ratio of shared final states as in

$$\eta_{\pm} = \frac{A(K_L^0 \rightarrow \pi^+\pi^-)}{A(K_S^0 \rightarrow \pi^+\pi^-)} = |\eta_{\pm}|e^{-i\phi_{\pm}} \quad (2.10)$$

$$\eta_{00} = \frac{A(K_L^0 \rightarrow \pi^0\pi^0)}{A(K_S^0 \rightarrow \pi^0\pi^0)} = |\eta_{00}|e^{-i\phi_{00}}. \quad (2.11)$$

The parameters $|\eta_{\pm}|$ and ϕ_{\pm} are relevant to the $K_L^0 \rightarrow \pi^+\pi^-e^+e^-$ models discussed in this thesis. Their measured values [19] are

$$|\eta_{\pm}| = 2.286 \times 10^{-3} \quad \text{and} \quad \phi_{\pm} = 43.51^\circ. \quad (2.12)$$

2.4 $K_L^0 \rightarrow \pi^+\pi^-e^+e^-$ Models

2.4.1 Phenomenological Model

In the late 1960's papers by Dolgov *et al.* [2] and Majumdar *et al.* [23] established the phenomenological model of the decay $K_L^0 \rightarrow \pi^+\pi^-e^+e^-$ based on the

CP violating decays $K_L^0 \rightarrow \pi^+\pi^-$ and $K_L^0 \rightarrow \pi^+\pi^-\gamma$. In $K_L^0 \rightarrow \pi^+\pi^-\gamma$ decays, an interference between the CP violating and CP conserving decays leads to a CP violating asymmetry in the polarization of the external photon. In $K_L^0 \rightarrow \pi^+\pi^-e^+e^-$, the phenomenological model predicts this same interference, carried now by a virtual photon. The asymmetry in the polarization propagates through the decay and manifests itself as an asymmetry in the $\pi^+\pi^-$ and e^+e^- decay planes. In the early 1990's, work by Sehgal *et al.* in [3, 4] gave predictions for the branching ratio and asymmetry as the first experiments to measure both for $K_L^0 \rightarrow \pi^+\pi^-e^+e^-$ were about to begin. The model described here was taken from P. Heiliger and L. Sehgal [4]. Modifications made by the KTeV, and NA48 brought the model into agreement with the experimental results.

The decay amplitude of

$$K_L^0(\mathcal{P}) \rightarrow \pi^+(p_+) \pi^-(p_-) e^+(k_+) e^-(k_-) \quad (2.13)$$

is described as the sum of the five distinct processes. Four are shown in Figure 2.3 while the fifth is a direct CP violating term. The matrix element has the form

$$\mathcal{M} = \mathcal{M}_{BR} + \mathcal{M}_{M1} + \mathcal{M}_{E1} + \mathcal{M}_{CR} + \mathcal{M}_{SD}. \quad (2.14)$$

The bremsstrahlung amplitude, \mathcal{M}_{BR} , and the direct emission amplitude, \mathcal{M}_{M1} and \mathcal{M}_{E1} , are analogues of the corresponding amplitudes for $K_L^0 \rightarrow \pi^+\pi^-\gamma$ where the photon is virtual and decays to an e^+e^- pair. The internal bremsstrahlung term is

$$\mathcal{M}_{BR} = e|f_s|g_{BR} \left[\frac{p_{+\mu}}{p_+ \cdot k} - \frac{p_{-\mu}}{p_- \cdot k} \right] \frac{e}{k^2} \bar{u}(k_-) \gamma^\mu v(k_+) \quad (2.15)$$

and corresponds to an E1 virtual photon emitted from either of the pion legs as shown in [a] of Figure 2.3. The form factor $|f_s|$ is determined from the decay rate

$$\Gamma(K_S^0 \rightarrow \pi^+\pi^-) = \frac{|f_s|}{16\pi m_k} \left[1 - \frac{4m_\pi^2}{m_k^2} \right]^{\frac{1}{2}}. \quad (2.16)$$

The parameter g_{BR} is

$$g_{BR} = \eta_{\pm} e^{i\delta_0(m_k)} \quad (2.17)$$

where η_{\pm} is the CP violating parameter described in the previous section and $\delta_J(M_{\pi\pi})$ is the phase shift for the final state strong interaction between the pion pair having an angular momentum J and an invariant mass $M_{\pi\pi}$.

The direct emission amplitude ([b] and [c] in Figure 2.3) is separated into a CP conserving piece in which the photon is emitted in the $CP = -1$ M1 state,

$$\mathcal{M}_{M1} = e|f_s| \frac{g_{M1}}{m_k^4} \epsilon_{\mu\nu\rho\sigma} k^\nu p_+^\rho p_-^\sigma \frac{e}{k^2} \bar{u}(k_-) \gamma^\mu v(k_+) \quad (2.18)$$

and a CP violating piece where the photon is in the $CP = +1$ E1 state,

$$\mathcal{M}_{E1} = e|f_s| \frac{g_{E1}}{m_k^4} [(\mathcal{P} \cdot k) p_+^\mu - (p_+ \cdot k) \mathcal{P}_\mu] \frac{e}{k^2} \bar{u}(k_-) \gamma^\mu v(k_+) \quad (2.19)$$

where k_μ is the four-momentum of the virtual photon and the parameter g_{M1} is

$$g_{M1} = i|g_{M1}| e^{i\delta_1(s_{\pi\pi})}. \quad (2.20)$$

The kinematic parameter $s_{\pi\pi}$ is the square, $M_{\pi\pi}^2$, of the invariant mass of the pion pair. In the models of [3, 4], $|g_{M1}|$ was assumed to be constant and was determined empirically from the ratio g_{M1}/g_{BR} to be 0.76. But, in order to fit the experimental results of $K_L^0 \rightarrow \pi^+\pi^-\gamma$ [24, 25, 26] and $K_L^0 \rightarrow \pi^+\pi^-e^+e^-$ [1, 6], $|g_{M1}|$ was modified to include a ρ -propagator vector meson dominance form factor, which is dependent on the energy of the lepton pair. Now, in modified form,

$$|g_{M1}| = \tilde{g}_{M1} \left[1 + \frac{a_1/a_2}{(m_\rho^2 - m_k^2) + 2m_k(E_{e^+} + E_{e^-})} \right] \quad (2.21)$$

where m_ρ is the mass of the ρ meson and \tilde{g}_{M1} and a_1/a_2 are parameters extracted from a fit of the data.

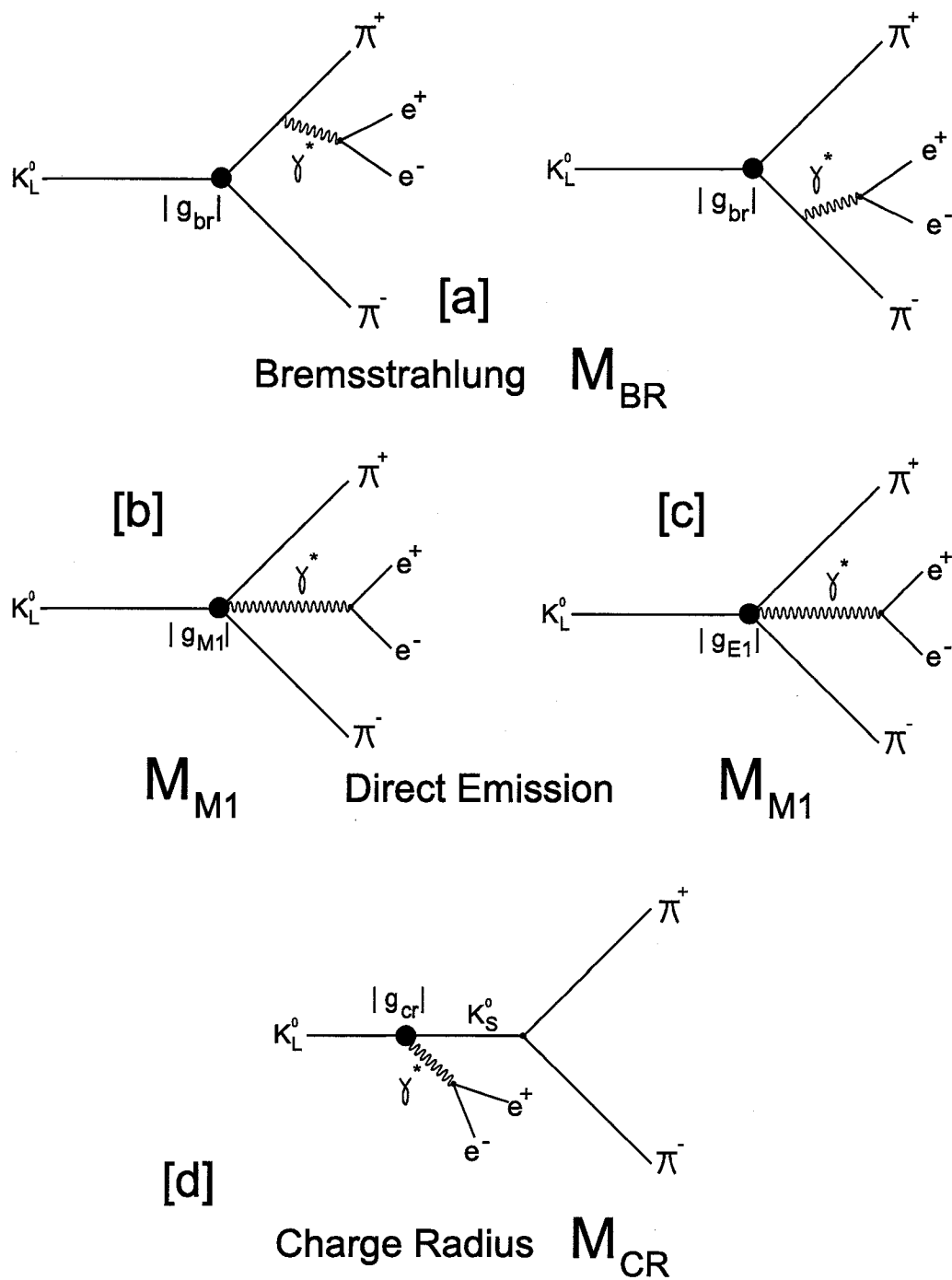


Figure 2.3: Diagrams illustrating the contributions of bremsstrahlung, direct emission M1 and E1, and K^0 charge radius terms to the matrix element of Eq. (2.14)

The parameter g_{E1} in Eq. (2.19) has the same form as Eq. (2.20), but due to the suppression imposed by the kinematics of a three-body decay over the two-body final state of the bremsstrahlung component and the suppression from the CP violating nature of the decay, the ratio of the E1 to M1 direct emission amplitudes is negligible and has been measured in KTeV [1] to have an upper limit of

$$\left| \frac{g_{E1}}{g_{M1}} \right| < 0.04. \quad (2.22)$$

Due to the dominance of g_{M1} over g_{E1} , the amplitude \mathcal{M}_{E1} is not included in the model.

The term \mathcal{M}_{CR} in Eq. (2.14) represents the K^0 charge radius contribution shown in diagram [d] of Figure 2.3. This amplitude includes the transition $K_L^0 \rightarrow K_S^0 \gamma^*$ which is forbidden due to energy-momentum conservation in the case where the photon is real. This is followed by the CP conserving decay of the K_S^0 into two pions. The amplitude for this process is

$$\mathcal{M}_{CR} = e|f_s| \frac{g_p}{m_k^2} \left(\frac{s_{\pi\pi} - m_\pi^2}{m_k^2 - m_\pi^2} \right) \left(\frac{1}{s_{\pi\pi} - m_k^2} \right) [k^2 \mathcal{P}_\mu - (\mathcal{P} \cdot k) k_\mu] \frac{e}{k^2} \bar{u}(k_-) \gamma^\mu v(k_+) \quad (2.23)$$

where

$$g_p = -\frac{1}{3} \langle R^2 \rangle_{K^0} m_k^2 e^{i\delta_0(s_{\pi\pi})} \quad (2.24)$$

and $\langle R^2 \rangle_{K^0}$ is the mean square charge radius of the K^0 determined from experiment.

The final term in Eq. (2.14) involves the direct CP violation in the decay $K_2^0 \rightarrow \pi^+ \pi^- e^+ e^-$. From Eq. (2.6), the amplitude can be determined from the linear combination of the $K^0 \rightarrow \pi^+ \pi^- e^+ e^-$ and $\bar{K}^0 \rightarrow \pi^+ \pi^- e^+ e^-$ matrix elements originating in the short-distance Hamiltonian of the weak interaction describing $s \rightarrow d$ transitions. From [4], the result is

$$\mathcal{M}_{SD} = -\frac{G_f}{\sqrt{2}} \sin(\Theta_C) \frac{\alpha}{m_k} g_{SD} (p_+ - p_-)_\mu \bar{u}(k_-) \gamma^\mu (1 - \gamma_5) v(k_+) \quad (2.25)$$

where

$$g_{SD} = i[\sin(\theta_2)\sin(\theta_3)\sin(\delta)]i\sqrt{2}\left(\frac{m_k}{f_\pi}\right)e^{i\delta_1(M_{\pi\pi})}, \quad (2.26)$$

θ_2 , θ_3 , and δ are CKM parameters, Θ_C is the Cabbibo angle, and $f_\pi = 130$ MeV is the pion decay constant.

From the spin-sum of the matrix elements in Eq. (2.14), the differential decay rate for $K_L^0 \rightarrow \pi^+\pi^-e^+e^-$ decays is

$$d\Gamma = \left(\frac{1}{2m_k(2\pi)^{12}}\right)|\bar{\mathcal{M}}|^2 \frac{d^3p_+}{2E_{\pi^+}} \frac{d^3p_-}{2E_{\pi^-}} \frac{d^3k_+}{2E_{e^+}} \frac{d^3k_-}{2E_{e^-}} \delta^{(4)}(\mathcal{P} - p_+ - p_- - k_+ - k_-). \quad (2.27)$$

The differential phase space volume elements, d^3p_i are not independent of one another and can be re-expressed as a function of five independent variables: $s_{\pi\pi} = (p_+ + p_-)^2$, $s_{ee} = (k_+ + k_-)^2$, Θ_π , Θ_e , and ϕ . The first two are the invariant masses of the $\pi^+\pi^-$ and e^+e^- pairs while the last three are angles which depend on the frame of reference, as shown in Figure 2.4. Θ_π is the angle between the positive pion's momentum vector \vec{p}_+ , and the e^+e^- decay plane in the $\pi^+\pi^-$ center of mass frame. Θ_e is the angle between the positron's momentum vector \vec{k}_+ and the $\pi^+\pi^-$ decay plane in the e^+e^- center of mass frame, and ϕ is the angle between the $\pi^+\pi^-$ and the e^+e^- decay planes in the K_L^0 center of mass frame. Rewriting Eq. (2.27) in terms of these five phase space variables gives

$$d\Gamma = I(s_{\pi\pi}, s_{ee}, \Theta_\pi, \Theta_e, \phi) ds_{\pi\pi} ds_{ee} d\Theta_\pi d\Theta_e d\phi. \quad (2.28)$$

The CP violating observable in $K_L^0 \rightarrow \pi^+\pi^-e^+e^-$ decays arises from the interference between the inner bremsstrahlung and M1 direct emission portions which are the dominant contributions to the matrix element. By integrating Eq. (2.28) over all variables except ϕ , the differential decay rate can be reduced to the sum of three terms,

$$\frac{d\Gamma}{d\phi} = A \cos^2(\phi) + B \sin^2(\phi) + C \sin(\phi)\cos(\phi). \quad (2.29)$$

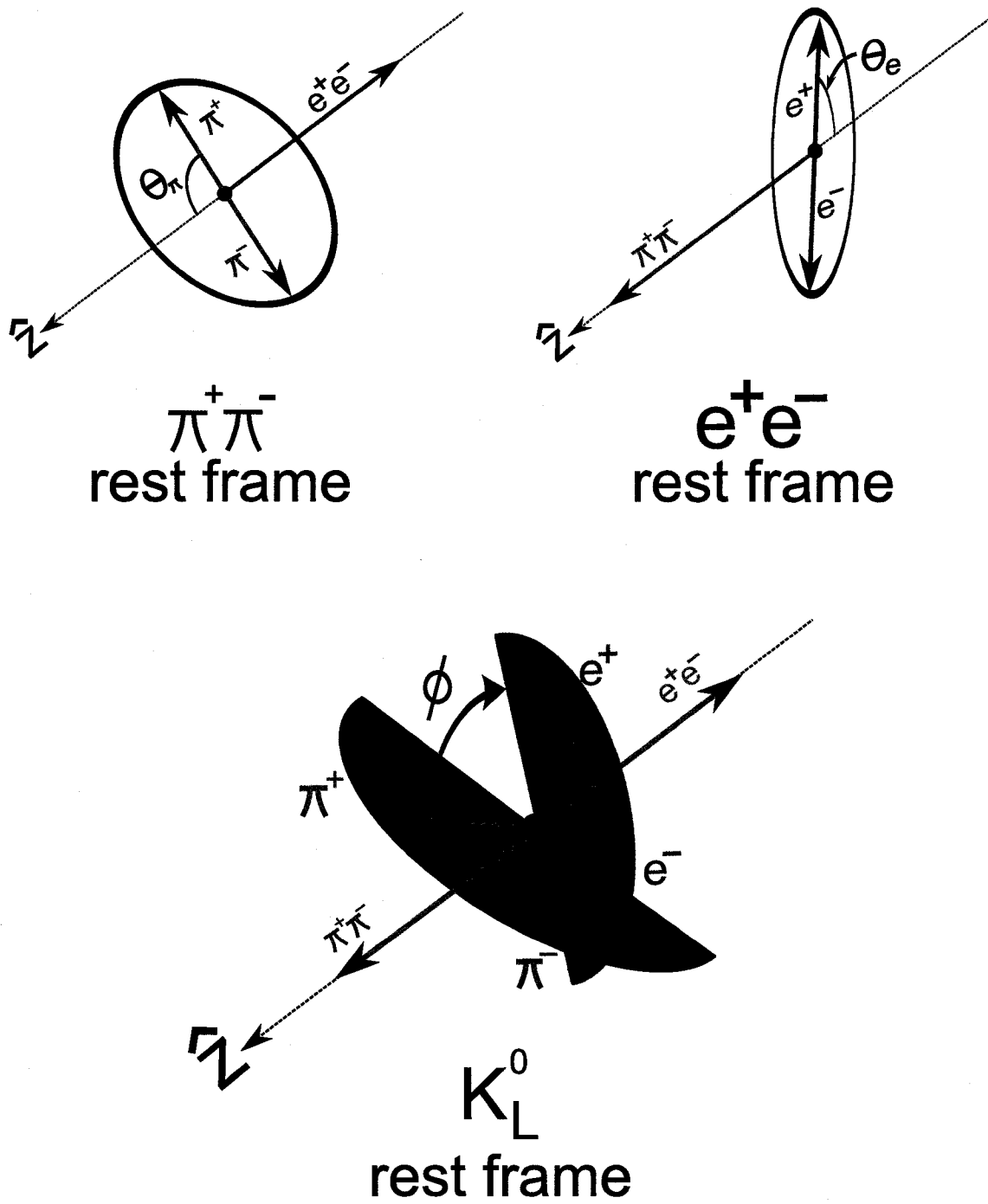
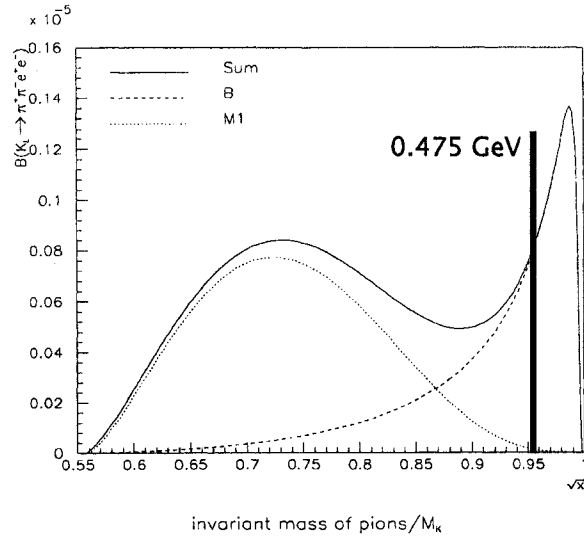


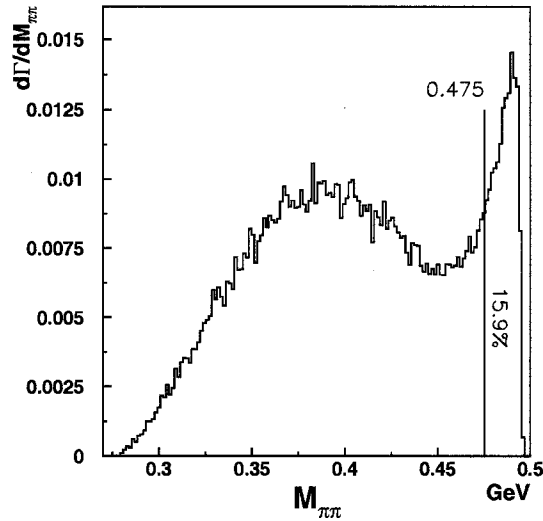
Figure 2.4: Definitions of the kinematic variables used to describe the phase space of the decay $K_L^0 \rightarrow \pi^+\pi^-\pi^+\pi^-$

Under CP, the last term changes sign and leads to an asymmetry in the angle between the $\pi^+\pi^-$ and e^+e^- decay planes in the K_L^0 center of mass. Unfortunately, the method used to identify $K_L^0 \rightarrow \pi^+\pi^-e^+e^-$ decays in E871 (described in Sec. 6.4) does not allow for a precise reconstruction of the e^+e^- decay plane in the K_L^0 center of mass frame, and thus an asymmetry measurement is not possible. Without the capability to make an asymmetry measurement, there was no need to implement either the phenomenological or the chiral perturbation model as a function of the angular variables and the differential decay rate was integrated over Θ_π , Θ_e , and ϕ .

Figure 2.5 shows the dependence of the differential decay rate on the invariant mass of the pion pair. The first experiments to measure the $K_L^0 \rightarrow \pi^+\pi^-e^+e^-$ branching fraction, KTeV and NA48, had detector acceptances which corresponded to the broad peak of Figure 2.5, but dropped off at higher invariant masses so that the narrow peak near the K_L^0 mass was not observed. The pion invariant mass spectra from the full results of KTeV [1] and NA48 [6] are shown in Figure 2.6 and include the acceptance of the detectors. In the phenomenological model, 15.9% of the decay rate is above $M_{\pi\pi} = 475$ MeV where KTeV and NA48 have less than 1% of their data. The acceptance for E871 is limited to a region of phase space where $M_{\pi\pi} > 475$ MeV which gives E871 the ability to examine the narrow peak shown in Figure 2.5. The phenomenological model parameters \tilde{g}_{M1} and a_1/a_2 in the magnetic form factor of Eq. (2.21) as well as $\langle R^2 \rangle_{K^0}$ in the charge radius form factor of Eq. (2.24) were extracted from a fit to the results from KTeV [1] and are shown in Table 2.1. Although the model fits the experimental results for the pion invariant mass region shown in Figure 2.6, it is unknown how well this model predicts the $K_L^0 \rightarrow \pi^+\pi^-e^+e^-$ phase space region that is accessible in E871.

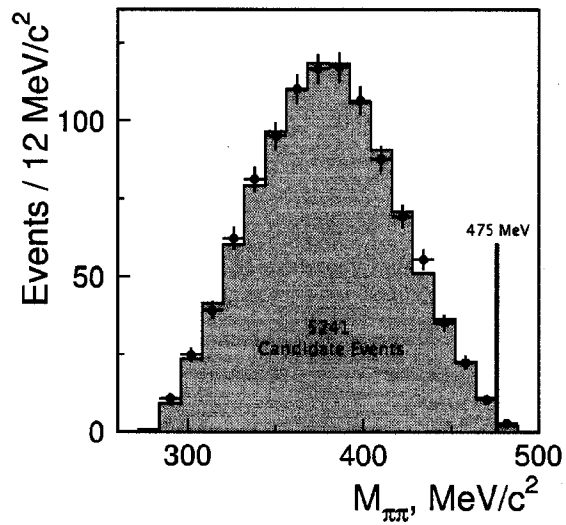


(a) $\frac{d\Gamma}{dM_{\pi\pi}}$, calculated from theory. Reprinted figure with permission from Heiliger, P. and Sehgal L. M., Phys. Rev. D, Vol 48, 4146, 1993. Copyright 1993 by the American Physical Society.

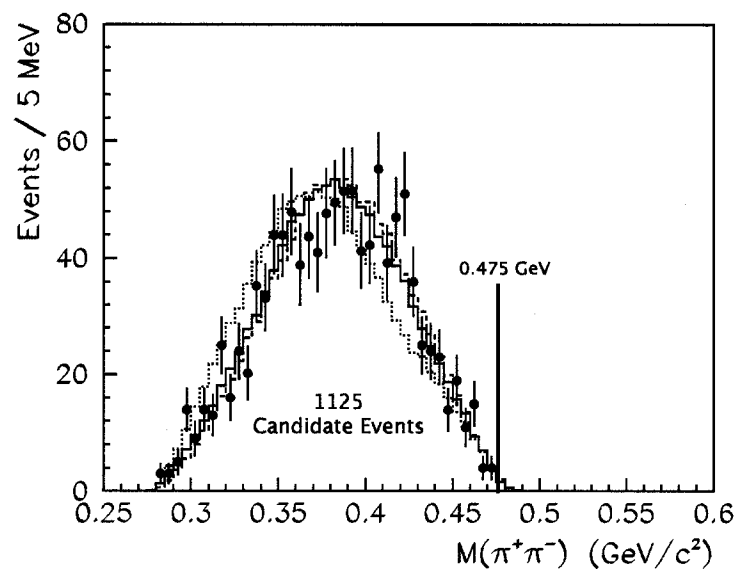


(b) $\frac{d\Gamma}{dM_{\pi\pi}}$, generated from Monte Carlo

Figure 2.5: The differential decay spectrum from the paper by Heiliger and Sehgal [4] and from Monte Carlo generated events after integrating over s_{ee} , Θ_π , Θ_e , and ϕ . The broader peak from 0.270 GeV to 0.450 GeV has been used to fit the data from KTeV and NA48, whose acceptances match in this region. The present work looks at the $M_{\pi\pi}$ region above 0.475 GeV and corresponds to the narrow peak which makes up 15.9% of the decay rate in this model.



(a) $M_{\pi\pi}$, KTeV 2006. Reprinted figure with permission from Abouzaid *et al.*, Phys. Rev. Lett., Vol 96, 101801, 2006. Copyright 2006 by the American Physical Society.



(b) $M_{\pi\pi}$, NA48 2003 Reprinted figure with permission from Lai *et al.*, Eur. Phys. J. C30, 33-49, 2003. Copyright 2003 by

Figure 2.6: Pion invariant mass distributions from KTeV [1] and NA48 [6]. These experiments have little acceptance in the region above 475 MeV, the region of relevance for this work.

| | |
|-----------------------------|--|
| \tilde{g}_{M1} | 1.11 ± 0.12 (stat) ± 0.08 (syst) |
| a_1/a_2 | $(0.744 \pm 0.027$ (stat) ± 0.032 (syst)) GeV^2/c^2 |
| $\langle R^2 \rangle_{K^0}$ | $(0.077 \pm 0.007$ (stat) ± 0.011 (syst)) fm^2 . |

Table 2.1: $K_L^0 \rightarrow \pi^+\pi^-e^+e^-$ phenomenological model parameters extracted from the full data set of KTeV [1]

2.4.2 Chiral Perturbation Model

In quantum chromodynamics (QCD), interactions involving the strong force are calculated in terms of quarks and gluons which are the fundamental degrees of freedom in the theory. At high energies, QCD can be applied perturbatively due to the asymptotically-free nature of the couplings. But at low energies such as those involved in kaon decays, the quarks are confined due to the increasing coupling constants, making QCD calculations in this regime difficult. Instead, strong interactions at energies below 1 GeV can be described in terms of the lowest-lying octet of pseudoscalar mesons (π, K, η) and the approximate chiral symmetry of QCD. This framework, called chiral perturbation theory (χ PT), is an effective field theory in which external momenta and quark masses are treated as small expansion parameters compared with the chiral symmetry breaking scale of 1 GeV, allowing perturbation theory to be performed in this energy region. Detailed accounts of χ PT can be found in reviews by Scherer [27], Pich [28], Leutwyler [29], and Ecker [30]. The model used in this experiment is from the work by Elwood, Wise, and Savage [31] in 1995, but is further described in papers by Savage [32], Pichl [33], and Ecker and Pichl [34].

Similar to the phenomenological model, the $K_L^0 \rightarrow \pi^+\pi^-e^+e^-$ amplitude in χ PT is dominated by the single virtual photon process $K_L^0 \rightarrow \pi^+\pi^-\gamma^* \rightarrow \pi^+\pi^-e^+e^-$ which has the form

$$\mathcal{M}_{1\gamma} = \frac{\sin(\Theta_C)G_f\alpha}{4\pi f_\pi q^2} [iG\epsilon^{\mu\lambda\rho\sigma} p_{+\lambda} p_{-\rho} q_\sigma + F_+ p_+^\mu + F_- p_-^\mu] \bar{u}(k_-) \gamma^\mu v(k_+). \quad (2.30)$$

The Lorentz scalar form factors G and F_\pm are functions of the hadronic kinematic invariants $q^2, q \cdot p_+$ and $q \cdot p_-$. The contributions from the K_1^0 and K_2^0 components of the K_L^0 can be examined separately and must have the correct CP symmetry properties. The form factors can be expanded as a power series in terms of the

external momenta and masses,

$$G = G^{(1)} + G^{(2)} + G^{(3)} + \dots \quad (2.31)$$

$$F_{\pm} = F_{\pm}^{(1)} + F_{\pm}^{(2)} + F_{\pm}^{(3)} + \dots \quad (2.32)$$

The superscript in the expansion denotes the order in χ PT with $F_{\pm}^{(i)}$ representing Q^{2i-1} powers of momenta and mass.

The diagrams containing the lowest order contributions to the form factors are shown in Figure 2.7 and correspond to the CP violating K_1^0 decays giving

$$G^{(1)} = 0 \quad (2.33)$$

and

$$F_{\pm}^{(1)} = \mp \frac{32g_8 f_{\pi}^2 (m_k^2 - m_{\pi}^2) \pi^2}{q^2 + 2(q \cdot p_{\pm})} \epsilon. \quad (2.34)$$

The parameter g_8 is a constant determined by measuring the decay rate for $K_S^0 \rightarrow \pi^+ \pi^-$ with a value of $|g_8| = 5.1$. The CP conserving decays from K_2^0 enter into the series at for $i = 2$ through the one-loop diagrams of the decay rate for $K_L^0 \rightarrow \pi^+ \pi^- \gamma$ in which higher order momentum-dependent contributions are neglected. From [32], we use a value of 39.3 for $G^{(2)}$.

For this work, only the lowest non-zero contributions for each form factor, $G^{(2)}$ and $F_{\pm}^{(1)}$, were taken into account. The second order term in F_{\pm} is included in the papers of Elwood *et al.* [31], Savage [32], and Pichl [33] and was implemented in the model. However, due to the insensitivity of the branching ratio in the phase space region of E871, the second order electric terms were subsequently removed from the model and excluded from this study. The differential decay rate was calculated by using the spin-summed squared matrix element of Eq. (2.30) and integrating over the angular phase space variables, as in the phenomenological model.

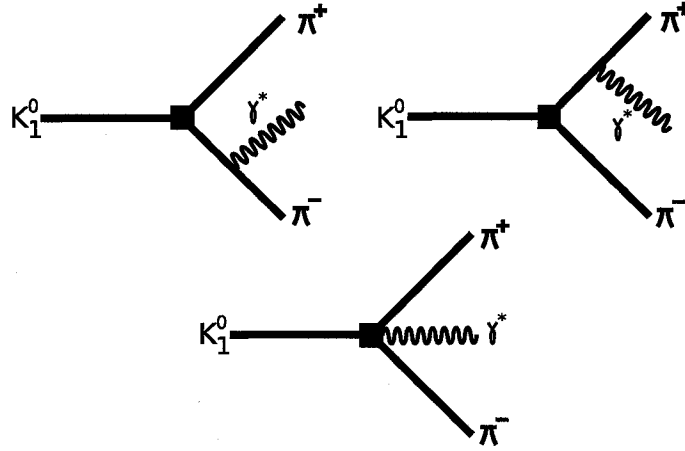


Figure 2.7: Tree-level Feynman diagrams contributing to the $F_{\pm}^{(1)}$ term of the chiral perturbation form factors.

The acceptance for $K_L^0 \rightarrow \pi^+\pi^-e^+e^-$ events to enter the E871 data stream is dependent on the dipion invariant mass spectrum of the decay. As shown in Figure 2.8(a), 52.6% of the events in the χ PT model have a pion pair that carries more than 475 MeV of the invariant mass. This is a factor of three increase over that of the phenomenological model Figure 2.8(b), which gives E871 the ability to distinguish between the two models. If we naively assume all other factors to be equal, the number of $K_L^0 \rightarrow \pi^+\pi^-e^+e^-$ events observed in the phase space region with $M_{\pi\pi} > 475$ MeV should be three times greater if the χ PT model is favored over the phenomenological model. The acceptance ratio for the models determined through Monte Carlo simulation in the E871 software shows the enhancement expected in the total number of events observed. In this work, the number of $K_L^0 \rightarrow \pi^+\pi^-e^+e^-$ events measured will be normalized to extract the branching ratios for the decay mode in the χ PT and phenomenological models so that a comparison to the world average can be performed.

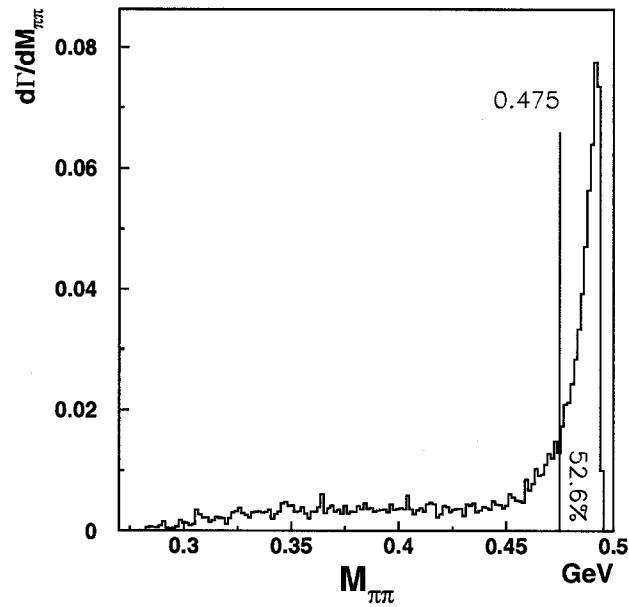
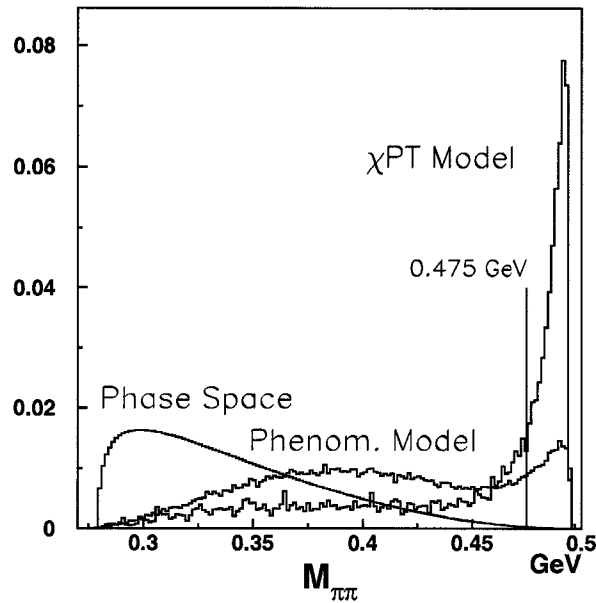
(a) $M_{\pi\pi}$, χ PT model(b) $M_{\pi\pi}$, model comparison

Figure 2.8: (a) The differential decay spectrum $\frac{d\Gamma}{dM_{\pi\pi}}$ from Monte Carlo generated events. The phase space of interest in E871, $M_{\pi\pi} > 0.475 \text{ GeV}$, has 52.6% of the decay rate accessible. (b) $M_{\pi\pi}$ spectra from Monte Carlo generated events for the phenomenological model, χ PT model, and a kinematic model which assumes no structure in the decay. The enhancement in the region above 0.475 GeV is evident.

Part II

Hardware and Software

CHAPTER 3

BNL E871 Detector

3.1 Overview

Experiment E871 began taking data at Brookhaven National Lab's Alternating Gradient Synchrotron (AGS) in early 1995. Situated in the B5 secondary beamline of the AGS, E871 was allocated 5600 hours of running time using a 24 GeV/c high intensity proton beam. Its primary purpose was to measure the branching fraction for the rare dileptonic decays of the long lived neutral kaon. To achieve this required achieving a single event sensitivity of 10^{-12} . A neutral kaon beam was created through associated production by impinging a proton beam on a high Z target. The background byproducts were removed through a series of magnets and lead foils designed to eliminate all charged products and photons in the beam path. The kaons decayed in the vacuum environment of the neutral beamline and decay tank over the a first 21 meters. The E871 detector was situated downstream of the decay tank and allowed for tracking, momentum, and particle identification information to be collected. The E871 experimental layout is given in Figure 3.1.

In order to reach a single event sensitivity of 10^{-12} , much care had to be put

into the design of the experiment. First, the intensity of the neutral beam needed to be maximized in order to measure as many K_L^0 decays as possible in the limited run time. This was accomplished by increasing the intensity of the primary proton beam, but at the cost of more background neutrons being produced. Second, the detector had to accept and reconstruct as many of the signal decays as possible while rejecting background. In order to efficiently record the signal, the decay product's momentum, direction and particle type had to be measured accurately to ensure proper event reconstruction. Redundancies in the detector allowed for a good tracking resolution and efficient particle identification. The experimental setup can be broken into three components: kaon production and beamline, momentum and tracking measurements, and trigger counters and particle identification. A compressed plan of the E871 neutral beamline and detector is found in Figure 3.2. Each part will be addressed in this chapter.

3.2 Neutral Beam Production

3.2.1 Primary Proton Beam

Brookhaven's Alternating Gradient Synchrotron (AGS) provided 24 GeV/c protons to multiple beamlines and experimental halls in spills that lasted approximately 1.5 seconds and had a variable repetition time ranging from 3.2 to 3.8 seconds. Each spill contained 15×10^{12} protons (15 Tp). The process of creating the primary proton beam began with the acceleration of H^- ions in the tandem facility from 25 keV to 750 keV. These were injected into the LINAC which boosted the H^- beam to 200 MeV using the accelerating fields of 286 drift tube cells resonating at 200 Mhz [35]. These spanned a distance of 145 m. At this point, the electrons of the H^- ions were removed by a stripper foil which allowed bare protons to enter the

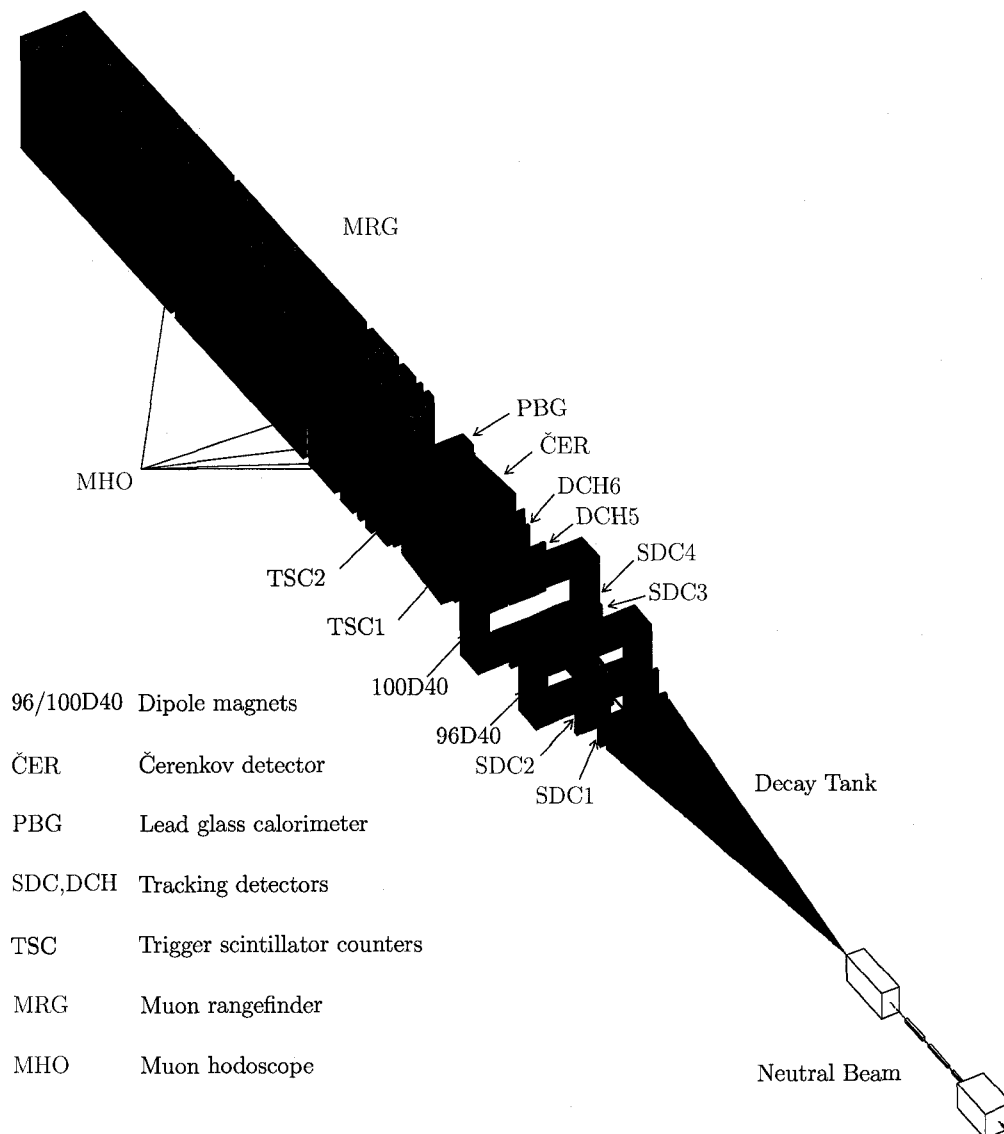


Figure 3.1: E871 experimental hall diagram.

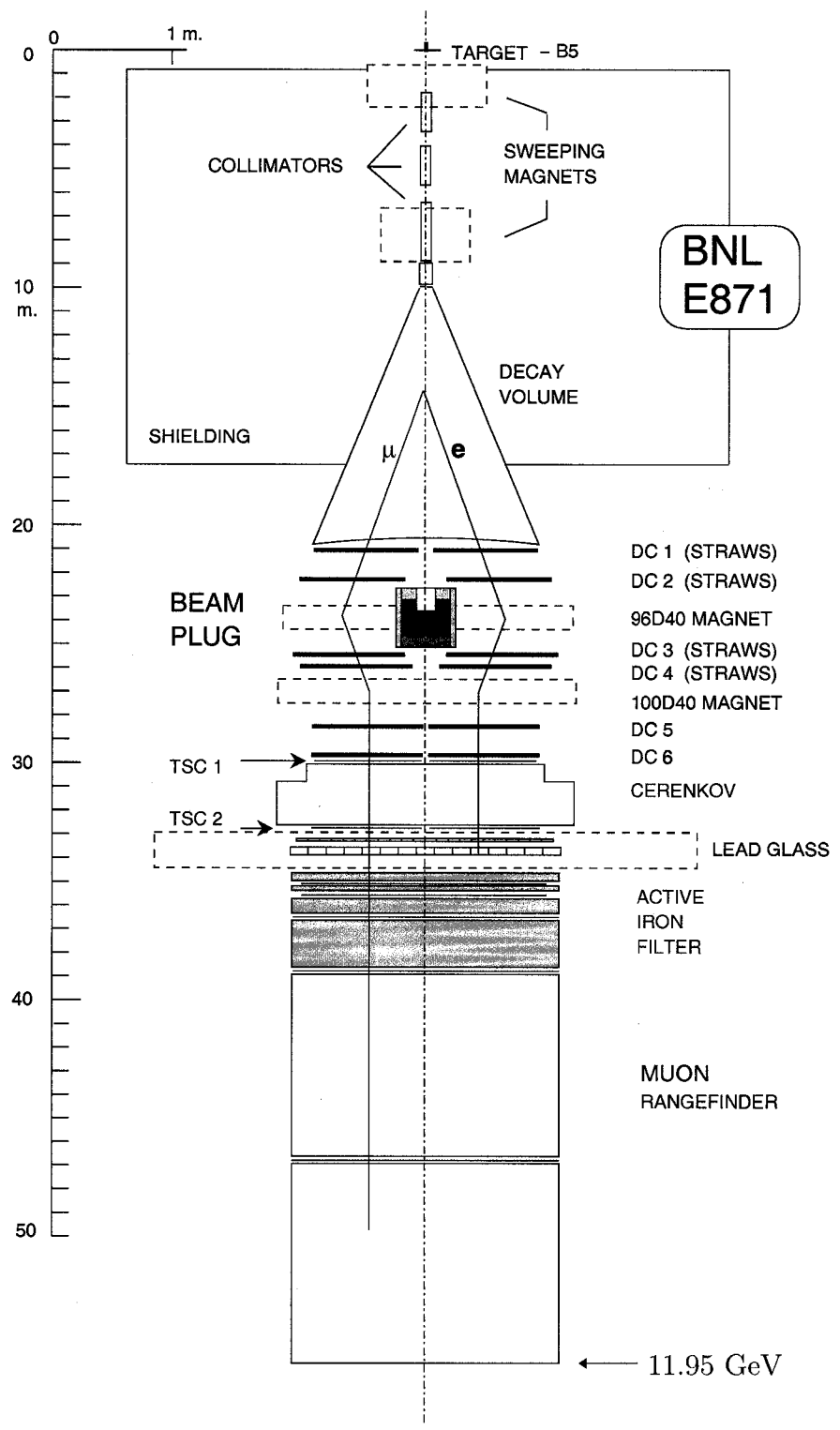


Figure 3.2: An overhead schematic of the E871 experimental hall. A compressed plane view of the neutral beamline, decay tank, spectrometer and particle identification apparatus.

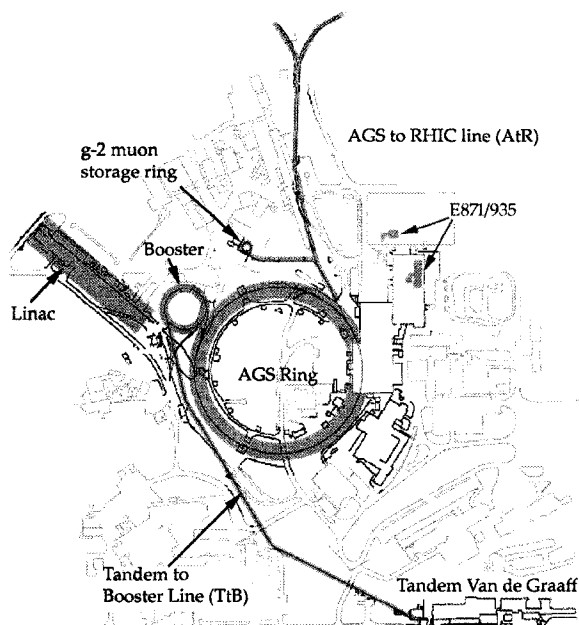


Figure 3.3: Brookhaven National Lab AGS The Layout of the AGS, support rings, and experimental halls at BNL.

AGS Booster ring. This ring had a circumference of 201.8 m, and increased the proton's kinetic energy to 1.5 GeV while grouping them into pulses of 15 Tp at a repetition rate of 7.5 Hz. From the Booster, the pulses were sent into the AGS, whose circumference was four times that of the Booster, and could hold four 15 Tp pulses for further acceleration. In the AGS, the protons were accelerated to an energy of 24 GeV/c and sent into a switch-yard of splitting magnets. The primary proton beam was then delivered to the B5 beamline, and onto the E871 target. The layout of AGS and these other preliminary systems can be seen in Figure 3.3.

3.2.2 Production Target

As described in Chapter 2, kaons are produced in the strangeness-conserving strong interaction $p^+ + \pi^- \rightarrow K^0 + \Lambda$. To ensure a high rate of production, the target material needed to have a high Z, so that the the proton beam would interact

in a relatively short distance. The E871 production target was made from platinum ($Z=78$), which has a density of 21.45 g/cm^3 and a hadronic interaction length of 189.7 g/cm^2 . As the primary beam entered beamline B, a series of quadrupole and dipole magnets focused and directed the beam onto the production target at a slight downward angle which could vary from $1\text{-}4.5^\circ$. In changing the angle at which the proton beam impacted the target, a trade-off between beam intensity and the neutron to kaon ($n : K^0$) ratio was made. A small angle allowed for a large beam intensity but also for a higher $n : K^0$ ratio. A larger angle decreased the $n : K^0$ ratio but at the cost of overall kaon beam intensity. To this end, a nominal operating angle of 3.75° was chosen to maximize the number of K^0 while minimizing the number of background-inducing neutrons. For a nominal incident flux of 15Tp/spill , the neutral beam consisted of $2 \times 10^8 K^0$ and 12×10^9 neutrons, for an $n : K^0$ ratio of approximately 60 [35].

The initial E871 target had dimensions of 127 mm length by 3.15 mm width by 2.54 mm height and was brazed onto a water cooled beryllium base with a Ag-Cu-Sn alloy (60-30-10%) for efficient heat transfer. A diagram of the target and base can be found in Figure 3.4. To allow for asymmetric thermal expansion over the 1.44 hadronic interaction lengths of the target, the platinum was divided length-wise into 5 segments. The target cross section was kept small to produce a tight secondary beam with a well known origin. To reduce the interaction of the primary beam with the target's base, beryllium ($Z = 4$) was used in its construction to reduce background contamination. In March of 1995, the target overheated during a high intensity test (25Tp/pulse). This resulted in the Ag-Cu-Sn alloy melting under the front two sections of the target which then fell off of the base. For the remainder of the 1995 run and the first half of the 1996 run, a backup target of the same design was installed. In May of 1996, a improved target was installed with a larger heat sink and a Ag-Cu-Li (92-7.5-0.025%) brazing alloy which could withstand a

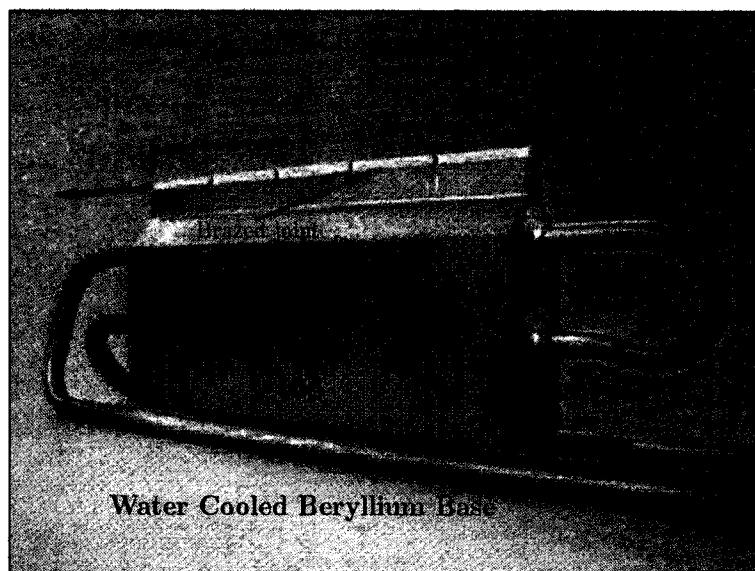


Figure 3.4: E871 Production target and Base The platinum neutral beam production target with the water-cooled beryllium base.

higher temperature environment. The new target had the same cross section as the original, but was divided into 15 sections, each 10mm long, corresponding to 1.70 hadronic interaction lengths of platinum.

3.2.3 Neutral Beam Creation and Colimation

A 10 meter long neutral beamline (Figure 3.5) consisting of two dipole magnets, a set of lead foils and 3 brass collimators was used to remove extraneous charged particles and photons, and to confine the secondary neutral beam to a tight cross section. Immediately following production in the platinum target, the beam consisted of neutrons, protons, pions, lambdas, photons, hyperons, and kaons. A sweeping magnet (B5P5) was centered one meter downstream of the target to remove charged particles and send them into a concrete and steel beam dump located below the beamline. Inside this magnet, 17 lead foils (2.5mm thick) were spaced at one centimeter intervals to induce photon conversion to electron-positron pairs

which were removed by the dipole magnets. The beam then traveled through the first of three precision, lead lined, brass collimators which confined the opening angle to 5 milliradians (mrads) in the horizontal (x) direction and 20 mrads in the vertical (y) direction. Following the last collimator, a second dipole magnet eliminated any remaining charged particles. At this point, the beam covered a solid angle of 100 milliradians and consisted of only neutrons and neutral kaons, as neutral pions were eliminated upstream due to their rapid decay to two photons ($\tau_{\pi^0 \rightarrow \gamma\gamma} \sim 10^{-17}$ s).

3.2.4 Decay Tank

Once the neutral beam was established, a interaction-free drift volume was needed in which the K_L^0 's could decay before reaching the front of the spectrometer. A trapezoidal decay tank was constructed to encompass the neutral beam for 10.9 m ($z=10$ m to $z=20.9$ m) following collimation. The upstream end had a cross section of 10 cm (x) by 16 cm (y) and it expanded to 193 cm (x) by 86.4 cm (y) at the downstream end. To make this region relatively interaction-free, the air was evacuated from the tank and a vacuum was held at 2×10^{-4} torr by a mechanical turbo pump for the entire run. The side walls were constructed of 5 cm thick, welded steel plates and concrete. In order to aid in the absorption of neutrons moderated in the side walls, the concrete was borated. To guard against any deflection of the neutral beam or the decay products, the upstream and downstream windows of the decay tank needed to be as thin as possible while still being strong enough to withstand the 775 torr of external air pressure. A 0.0127 cm layer of Mylar was sufficient to cover the upstream opening, but the downstream end was reinforced by 0.0381 cm of Kevlar to withstand the 1.72×10^5 Newtons of force exerted on this window. But despite this, during the final week of the 1995 run, the downstream window failed, resulting in the implosion of the 18.123 m³ decay tank. The tank was

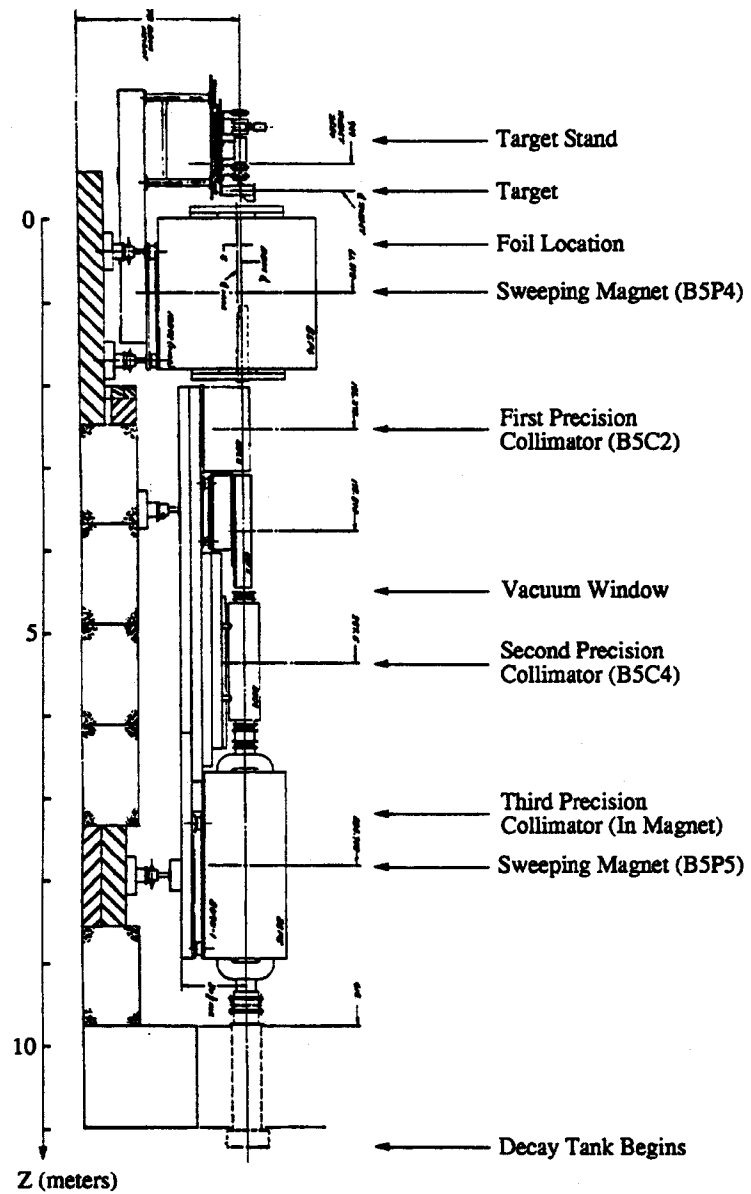


Figure 3.5: Side view of the E871 neutral beamline.

rebuilt for the 1996 run, along with the majority of the straw drift chambers which were damaged in the implosion. The downstream window's 0.381 cm of Kevlar was replaced with a stronger, ballistic grade of Kevlar at 0.4318 cm thickness.

Of the 4×10^8 K^0 produced, half were K_S^0 with a lifetime of 0.8935×10^{-10} s and half were K_L^0 with a lifetime of 5.17×10^{-8} s. The length and location of the tank was selected to maximize the number of K_L^0 decaying inside the tank while minimizing the contamination caused by K_S^0 decays. The average decay length ($c\tau$) of the K_L^0 is 15.51 m, which is situated at the center of the decay tank, while the K_S^0 's decay length is 0.023 m, well upstream of the decay region.

3.3 Spectrometer

In order to fully reconstruct a K_L^0 that decays in the vacuum tank, its daughters must be identified and tracked to obtain direction, momentum, and energy information. The particle identification of the tracks downstream in the final section of the detector is described in Sec. 6.3. E871 uses a two armed spectrometer, Figure 3.6, which consisted of two dipole magnets to redundantly measure a particle's momentum as it curves through the magnetic fields. Tracking is accomplished by measuring the hits in 4 left/right pairs of straw drift chambers upstream of the second magnet, followed by 2 left/right pairs of conventional wire drift chambers downstream of the last magnet. Precise measurement of the daughters' properties allows for proper decay vertex reconstruction in the decay tank as well as the ability to associate tracks in the spectrometer with hits in the downstream particle identification counters.

3.3.1 Straw Drift Chambers

A straw drift chamber consists of several layers of tightly packed, gas filled cylindrical straws which measure the distance a charged particle passes from the

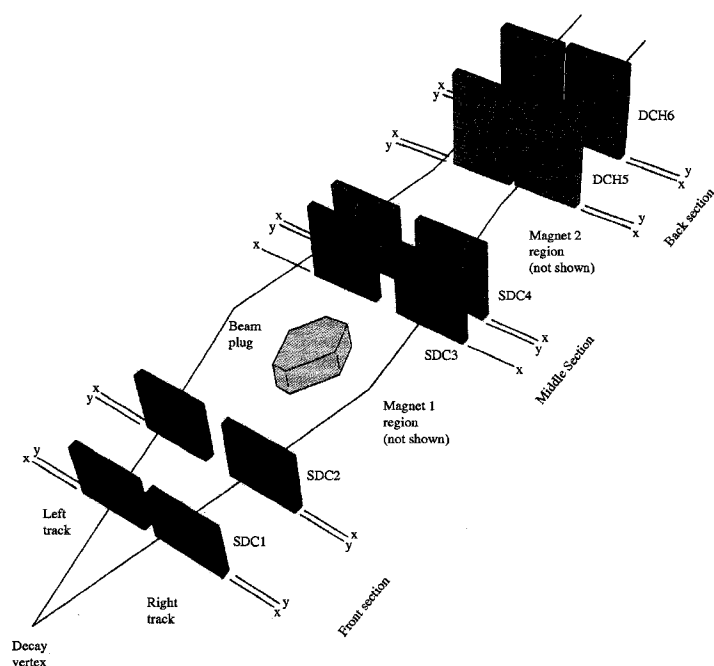


Figure 3.6: E871 two-armed magnetic spectrometer.

central axis. Each conducting straw is held at ground potential and acts as a cathode while a thin tungsten wire stretched down the center of the straw is held at a high potential and acts as an anode. As a charged particle passes through a straw, it ionizes the gas inside. The freed electrons then move inward along the radial electric field lines toward the sense wire. As they travel, the electrons ionize more of the drift gas and the process is repeated. The resulting avalanche of charge is collected on the sense wire and read out by electronics that calculates the drift time of the electrons needed to reach the sense wire. Using the known drift velocity of the electrons in the gas along with the measured drift time, the minimum radial distance between the charged particle track and the sense wire can be found. Although the cylindrical symmetry of the straw creates an ambiguity over which side of the sense wire the particle went through, the ambiguity is overcome by using staggered layers of the straws as shown in Figure 3.7. Vertical planes of straws give the x -coordinate while

horizontal planes give the y -coordinate. Sets of horizontal and vertical planes of straws are used in a chamber to give the y and x position of a track over a short distance in z .

Due to the large hit rates in the forward spectrometer produced by the undecayed neutral beam and by background decays, the highly segmented nature of the straw chambers makes them ideal to provide a low single-cell occupancy for tracking in the region close to the decay tank. As with the conventional drift chambers described later, they are low mass, which minimizes the chance for interaction or multiple scattering that can degrade the ability to accurately reconstruct the event.

Four left/right pairs of straw chambers are used in E871 in the forward region of the spectrometer as seen in Figure 3.6. SDC1, SDC2, and SDC4 each contain horizontal (y -coordinate) and vertical (x -coordinate) planes of straws while SDC3 only has a vertical plane to reduce the cost and mass of the spectrometer. Each vertical plane consists of three layers of straws for precise determination of the x -position of each track, while each horizontal plane has only two layers for the y -position. The momentum calculation depends on the curvature of the track in the x direction, and the extra layer of straws increases the likelihood of a chamber making a good position measurement. Each chamber contains between 400 and 500 straws whose length range from 80 cm to 120 cm to keep the same solid angle as the particle moves downstream.

Each straw was 5 mm in diameter and was made from 25 μm thick Mylar. The interior of the straws was coated with a 1000 \AA layer of copper oxide. The 20 μm diameter sense wires were made from gold-plated tungsten and centered in the straws under tension. The voltage on the anode wire varied from 1850 V (out of spill) to 1950 V (in spill) to prevent charge accumulation when the beam was not present. A 50/50 combination of carbontetrafluoride (freon) and ethane gases was used in the straws to provide a fast ionizing environment while quenching the

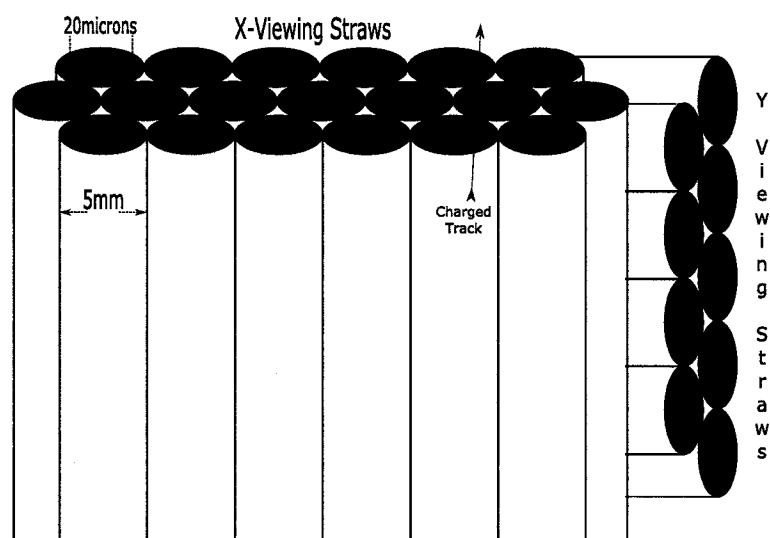


Figure 3.7: The layout of the straw drift chambers with x and y -viewing straws.

de-excitation photons. At 1950 V, the freon-ethane mixture gives a drift velocity of $100 \mu\text{m}/\text{ns}$ which is adequate to deal with the 200 kHz rates per straw typical in the drift chambers. The single wire resolution was measured at $160 \mu\text{m}$ with a efficiency of 96%. After the chambers were damaged by the implosion of the decay tank at the end of the 1995 run, they were rebuilt to the same specifications for the 1996 run except Kapton was used for the straw material instead of Mylar.

3.3.2 Momentum Analyzing Magnets

Two dipole magnets were used to give the K_L^0 decay products a net 200 MeV/c inward kick of transverse momentum as they travel through the spectrometer. Both magnets consisted of an iron yoke and two vertically aligned, water-cooled coils that produced a uniform field in the vertical (y) direction (Figure 3.8). Iron plates were attached to the upstream and downstream faces of the yoke which acted as magnetic mirrors to contain the field to the region defined by the coils. The magnets were placed on pedestals to match the beamline with the axis of the iron yoke. The

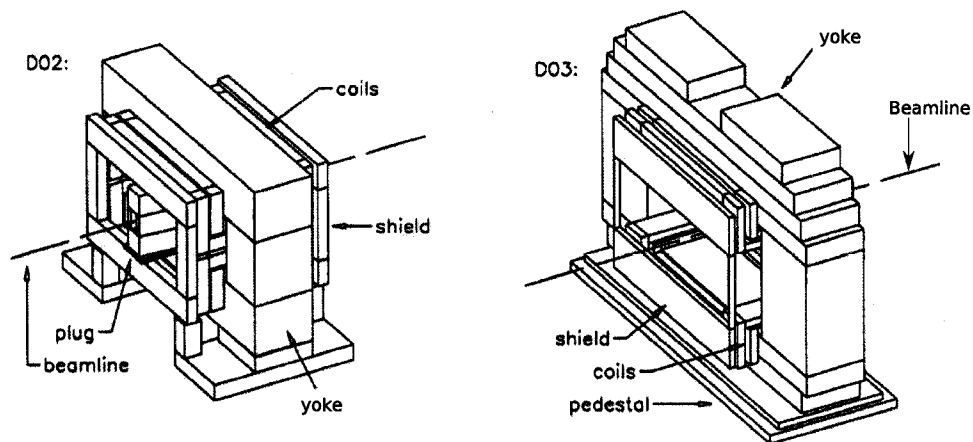


Figure 3.8: The Dipole Magnets D02 and D03.

upstream magnet, D02, carried a current of 3600 A and produced a field of $1.4 \text{ T} \cdot \text{m}$ along the vertical. This field imparted $416 \text{ MeV}/c$ of transverse momentum in such a way that negatively charged particles entering the region beam left and positively charged particles entering the region on the beam right would be bent inward toward the beam axis. The downstream magnet, D03, carried a current of 1900 A and produced a field of $-0.7 \text{ T} \cdot \text{m}$ along the vertical. This field imparted a $216 \text{ MeV}/c$ kick outward from the beam axis so that the in-bent particles from D02 would be out-bent for a net transverse momentum change of $200 \text{ MeV}/c$. The spectrometer magnets were specifically tuned to provide this momentum change to maximize the acceptance for two body K_L^0 decays. The maximum transverse momenta for the decays of interest in E871 are shown in Table 3.1. Daughters from a K_L^0 decay that enter the spectrometer at the maximum p_T , will emerge from the second magnet nearly parallel. This specific tuning of the magnets also allows for 4-body decays with two tracks carrying the majority of the K_L^0 invariant mass to be accepted. A decay with the maximum transverse momentum produces tracks that traverse the spectrometer and enter the rear of the detector parallel to the beamline.

| Decay Branch | Fraction | Decay p_t (MeV/c) |
|---|---------------------------------------|---------------------|
| $K_L^0 \rightarrow \pi^\pm e^\mp \nu_e$ | $(38.78 \pm 0.27)\%$ | 229 |
| $K_L^0 \rightarrow \pi^\pm \mu^\mp \nu_\mu$ | $(27.17 \pm 0.25)\%$ | 216 |
| $K_L^0 \rightarrow \pi^+ \pi^-$ | $(2.067 \pm 0.035) \times 10^{-3}$ | 206 |
| $K_L^0 \rightarrow \pi^+ \pi^- \gamma$ | $(4.17 \pm 0.15) \times 10^{-5}$ | 206 |
| $K_L^0 \rightarrow e^+ e^-$ | $(9.4_{-4.6}^{+5.9}) \times 10^{-12}$ | 249 |
| $K_L^0 \rightarrow \mu^+ \mu^-$ | $(7.2 \pm 0.5) \times 10^{-9}$ | 225 |
| $K_L^0 \rightarrow \mu^\pm e^\mp$ | $< 4.7 \times 10^{-12}$ | 238 |
| $K_L^0 \rightarrow \mu^+ \mu^- e^+ e^-$ | $\approx 2.9 \times 10^{-9}$ | 225 |
| $K_L^0 \rightarrow \pi^+ \pi^- e^+ e^-$ | $\approx 3.5 \times 10^{-7}$ | 206 |

Table 3.1: Transverse momentum for K_L decay modes

3.3.3 Drift Chambers

Downstream of the first magnet, the single cell rates experienced by the chambers drops to an average of 100 kHz because of the effectiveness of the compact neutral beam stop, which will be discussed in Sec. 3.3.4. These rates are low enough to permit the use of conventional wire drift chambers for the final two pairs of position sensitive detectors in the spectrometer. Wire chambers give a better single wire resolution and efficiency than the straws, and also add a smaller mass to the path a particle travels, reducing the level of multiple scattering. DC5 and DC6 were created identically, with 3 planes of 152 cm long x measuring wires and 2 planes of 92 cm long y measuring wires in each left/right pair. Unlike the cylindrical straws, these cells were created by surrounding a gold-plated tungsten sense wire with six aluminum field wires in an irregular hexagonal shape, as shown in Figure 3.9. The field wires were 109 μm in diameter and held at a potential of -2300 V while the sense wires had a diameter of 20 μm and were held at ground potential. Aluminum guard wires, held at ground, were positioned around the outside of the planes to help shape each cell's electrostatic field. A mixture of 49% Argon, 49% Ethane, and 2% Ethanol and water was used as the low-threshold ionizing medium. This gas

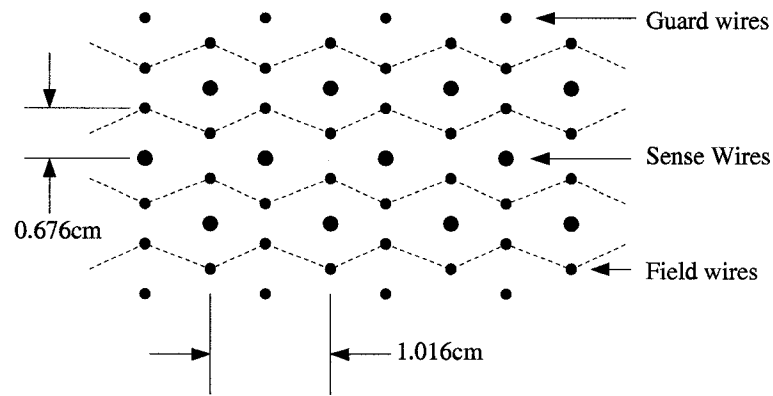


Figure 3.9: The cross section of the x -viewing layers of a traditional drift chamber.

exhibited an average drift velocity of $50 \mu\text{m}/\text{ns}$ leading to a single wire resolution of $120 \mu\text{m}$ and an efficiency of 98%.

3.3.4 Beam Stop

In E791, the forerunner to this experiment, a limit on the intensity of the neutral beam was reached because of beam-induced background effects. E791 used a two-armed spectrometer with sufficient angle between the arms to leave a path for the remnant of the neutral beam to pass through. Even with this precaution, the event quality was severely degraded by neutrons and kaons decaying downstream of the decay tank and creating hits in the tracking chambers when the beam intensity was greater than 5.5 Tp. In an effort to improve the sensitivity, E871 introduced a neutral beam stop, or beam plug, inside the first spectrometer magnet to block any particles left within the profile of the beam as they left the decay tank. The elimination of the neutral beam allowed E871 to increase the intensity of the neutral beam by a factor of three over E791, and to measure tracks downstream of the beam plug that were close to the beam axis. These factors significantly increased the sensitivity and acceptance of the E871 detector.

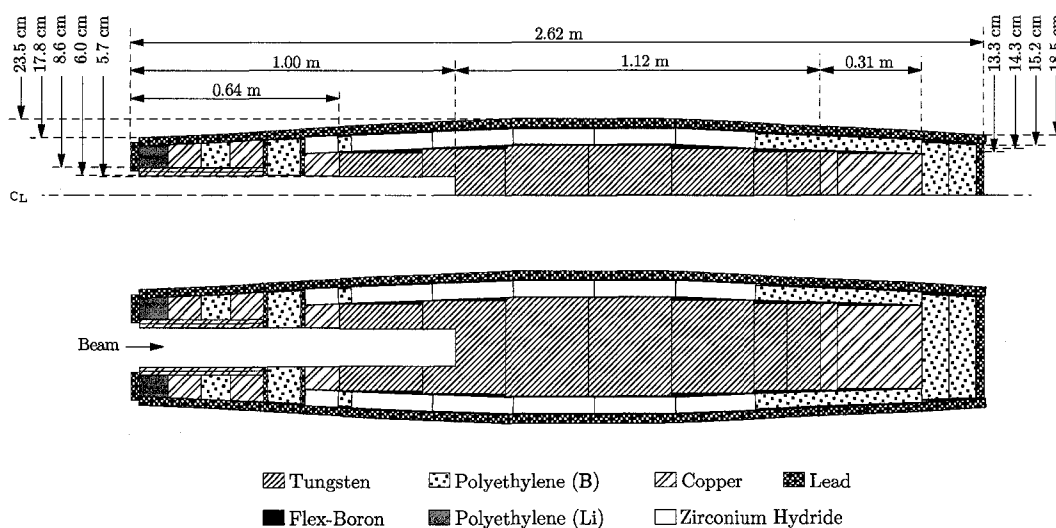


Figure 3.10: An x-z cross section of the neutral beam stop.

The beam plug's goal was to stop all particles that entered, and contain any secondaries generated in the process. Mass is the key to stopping neutral particles, but the size of the stop was limited by the interior dimensions of the first spectrometer magnet. Figure 3.10 shows a cross-section of the beam stop, which had a long profile with a narrow opening to shield against back-scattered particles. The core of the plug was made from 5000 kg of "Heavimet", a tungsten-nickel alloy (97%-3%), which provided twelve hadronic interaction lengths of material. This was backed by 1880 kg of copper to add mass at a reduced cost. Surrounding the dense core was a layer of zirconium hydride and either borated or lithium-doped polyethylene used to capture neutrons moderated or produced in the Heavimet or copper. Finally, a layer of lead was wrapped around the entire plug to absorb any photons emitted during neutron capture. As seen in Figure 3.11, the effectiveness of the beam plug is reflected in the drop in hit rates of the SDC1 and SDC2 (upstream of the stop), compared to those of SDC3, SDC4, DC5, and DC6 (downstream of the stop). The first two pairs of straw drift chambers show elevated hit rates in cells close to the beam axis where the beam affecting background was more likely, while the remaining

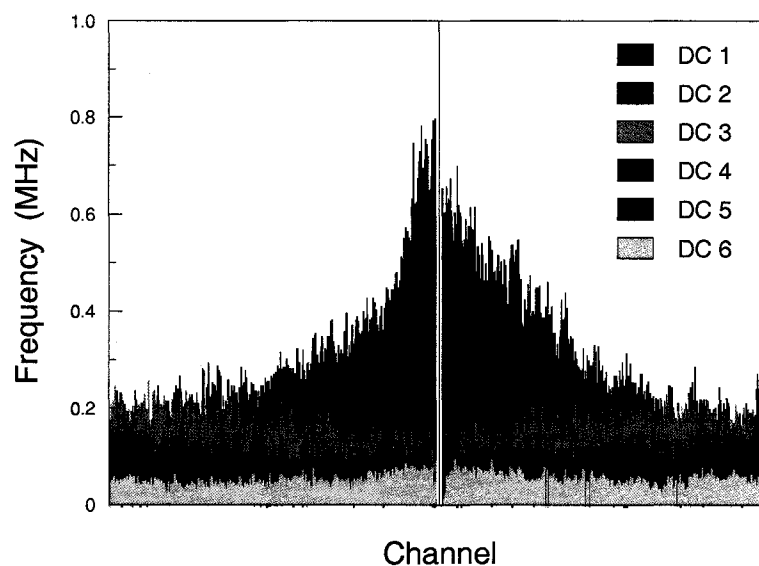


Figure 3.11: Single channel hit rates for the drift chambers. The drop in singles rates after the first magnet is significant in the channels close to the beam axis.

four drift chamber's hit rates are relatively flat across the cells.

3.4 Trigger Counters and Particle Identification

The second half of the E871 detector includes the triggering mechanism for signaling a good event and the means by which particles were identified. A set of fast scintillator counters was used to reduce background by triggering on events with low transverse momentum. This helped to eliminate the 3-body decays that dominate the K_L^0 branching ratio. Efficient particle identification was necessary to ensure precise event reconstruction. Just as redundant measurements were made to find the momenta of daughters, multiple routines were used to tag particles as electrons, pions or muons.

3.4.1 Trigger Scintillator Counters

In high rate experiments such as E871, trigger detectors are necessary to indicate the presence of an event to the data acquisition system (DAQ). The detectors had to be fast, to reduce the amount of dead time, and efficient so that no candidate events were lost. By careful arrangement of the magnetic fields in D02 and D03, the trigger system can also screen events to eliminate background before they are recorded, saving computing time and storage space. E871's primary goal was to search for rare two-body decay modes of the K_L^0 . As seen in Table 3.1, the maximum decay momenta for these modes are all above 200 MeV/c. The main backgrounds arise from 3-body semileptonic decays which have maximum decay momenta for the lepton and pion of over 200 MeV/c as well, but this is in the limit where the neutrino carries no momentum. The majority of these events will have a transverse momentum well below 200 MeV/c. To separate these events, the Spectrometer magnets were carefully tuned to provide a net 200 MeV/c transverse momentum kick to the decay products. In this system, the 2-body decays will emerge from the spectrometer either parallel or slightly out-bent. The majority of 3-body backgrounds will leave the spectrometer in-bent (Figure 3.12) or not make it out of the spectrometer at all.

Two stations of segmented trigger scintillator counters were arranged perpendicular to the beamline (Figure 3.13) and used to record the presence of an event with a degree of parallelism (see Chapter 4) to the data acquisition system. The first station (TSC1) was located at $z = 29.94$ m, just downstream of the last drift chamber, and contained two planes situated to the right and left of the beamline. Each plane in TSC1 contained 32 vertical scintillator slats 165.3 cm long by 3.2 cm wide by 0.5 cm thick. The slats were arranged into 2 layers and staggered so that adjacent scintillators overlapped by 0.29 cm as in Figure 3.14.

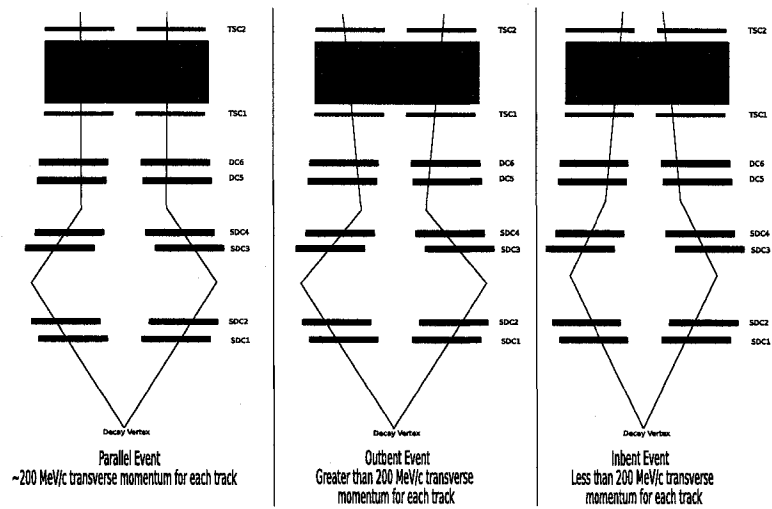


Figure 3.12: Examples of two-body events with ideally focused tracks (a), overfocused tracks (b), and underfocused tracks (c).

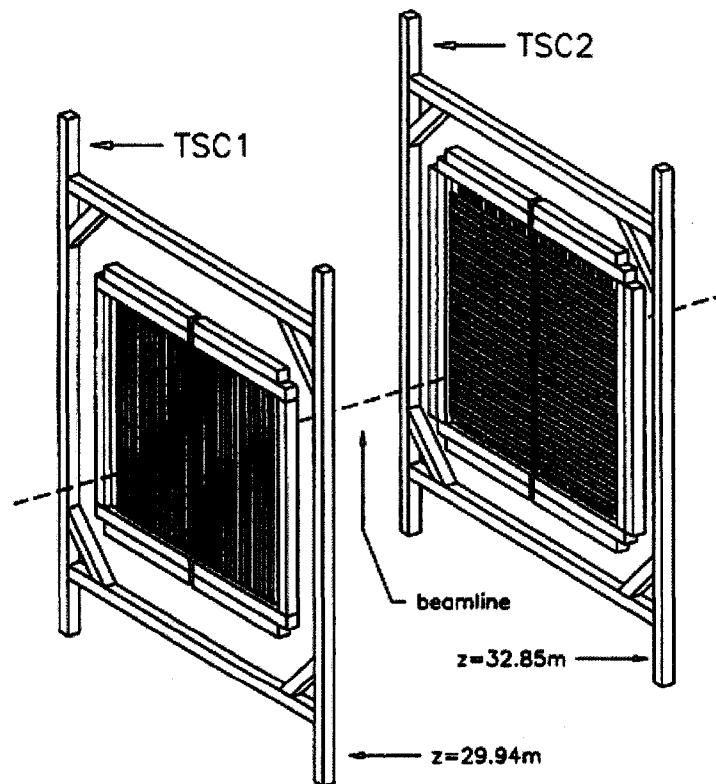


Figure 3.13: The scintillating hodoscope used to trigger properly focused events. TSC1 contains 32 x -measuring slats while TSC2 contains 32 x -viewing slats and 64 y -viewing slats.

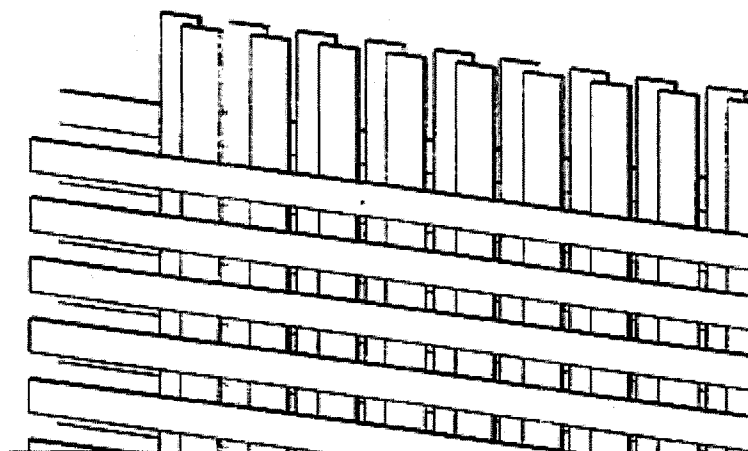


Figure 3.14: A drawing of the layout of TSC2. The x and y -viewing slats were staggered to eliminate gaps in the hodoscope.

The second station (TSC2) was located at $z = 32.85$ m, directly after the Cerenkov counter, and was broken into two planes for the beam left and beam right components as in TSC1. But, whereas TSC1 could only measure the x -position, TSC2 could measure both the x and y position. Only the second station contained y -viewing scintillators to reduce the chance of multiple scattering or of kicking an energetic electron into the track path which could affect the efficiency of the Cerenkov counter. The x -viewing slats in TSC2 had the same arrangement and dimensions as those in TSC1 except they were 189.7 cm long to present the same angular coverage. The 64 y -viewing slats were separated into two layers and arranged on either side of the vertical slats as in Figure 3.14 and staggered such that they overlapped by 0.28 cm. These scintillators were 100.9 cm long by 3.0 cm wide by 0.5 cm thick.

Each slat was made from Bicron BC-408, a polyvinyl toluene scintillator which provided a fast signal response with a rise-time of 0.9 ns, a decay time of 2.1 ns, and a FWHM pulse width of 2.5 ns. The attenuation length of the 425 nm light emitted was measured at 120 cm. Because this length is less than the length of the x -viewing slats, a photomultiplier tube was used to read out each end of the scintillators to

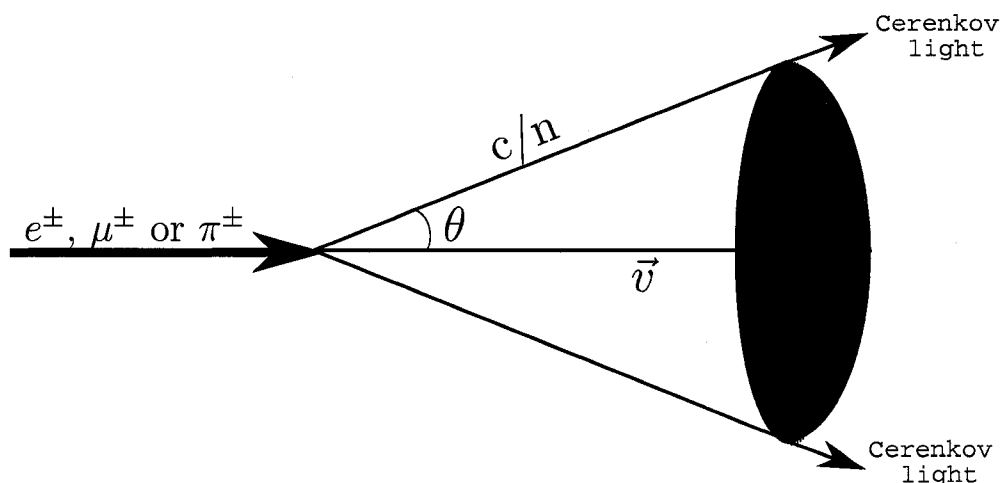


Figure 3.15: The light cone produced through the Cerenkov effect in a dielectric medium.

reduce the amount of light lost to attenuation.

3.4.2 Cerenkov Counter

Directly following the first plane of trigger scintillator counters was the first of four particle identification detectors. The threshold Cerenkov counter was designed to select out electrons over pions and muons. This counter relied on the Cerenkov effect, which states: if a charged particle travels faster than the speed of light in that medium, it will radiate a coherent plane of light as it travels, *i.e.* radiation occurs when

$$\beta n > 1, \quad (3.1)$$

where

$$\beta = \frac{v}{c} = \frac{p}{\sqrt{p^2 + m^2 c^2}}. \quad (3.2)$$

Particles with greater mass will need a larger momentum in order to reach the Cerenkov threshold and produce light. The radiation emitted will form a cone, as

| Particle | Mass (MeV/c^2) | Threshold (GeV/c) |
|-----------|--------------------|-------------------|
| e^\pm | 0.511 | 0.031 |
| μ^\pm | 105.6 | 6.357 |
| π^\pm | 139.6 | 8.396 |
| p | 938.3 | 56.233 |

Table 3.2: Threshold momenta for Čerenkov radiation in Hydrogen (H_2)

seen in Figure 3.15, with an opening angle which is dependent upon the particle's velocity and the medium's index of refraction:

$$\cos(\theta) = \frac{1}{\beta n} \quad \text{with} \quad \beta n > 1. \quad (3.3)$$

The detector built for E871, shown in Figure 3.16, was approximately 2 m square by 2.8 m deep and was constructed from aluminum. The front window was made of 127 μm of Mylar covered with 38.1 μm of Tedlar to ensure no light leakage. A thin front window also reduced the chance for multiple scattering and reduced the chance of scattering electrons above the Čerenkov threshold which could create a false signal. The interior was filled with hydrogen gas held at 7.6 cm H_2O of overpressure with respect to atmosphere to prevent air from contaminating the chamber. The index of refraction for this medium was 1.0001392. The momentum thresholds for electrons, pions, and muons in diatomic hydrogen gas can be found in Table 3.2. The large momentum difference between electrons and muons leads to high efficiency in tagging electrons except in the highest energy events. In order to minimize any loss in efficiency in the electron identification, the track momentum of an event was limited to be below 6.5 GeV/c to avoid misidentifying a muon as an electron.

The Čerenkov radiation was collected by reflecting the light off of 32 spherical mirrors covering the interior of the downstream wall into 32 photomultiplier tubes. The beam right and beam left sections for the counter were separated by a black

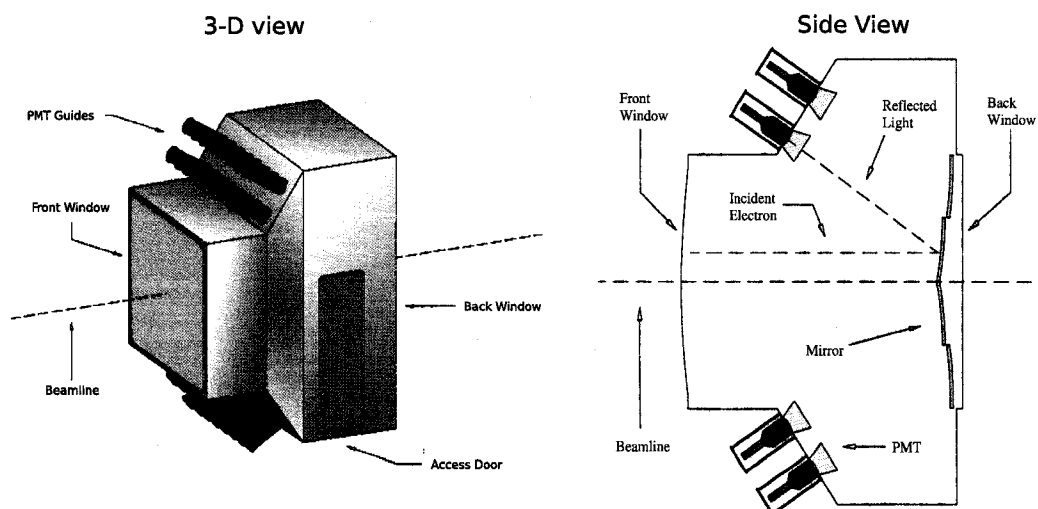


Figure 3.16: The E871 threshold Cerenkov counter external and internal geometry.

Tedlar curtain hanging vertically along the beam axis to create two active halves. Each half's rear wall contained 16 mirrors hung in a 4×4 grid with each reflecting to an individual photomultiplier tube. The outer two columns of each half contained larger mirrors measuring 25.8 cm x 45.7 cm, while the inner two columns had mirrors with dimensions 23.1 cm x 45.7 cm. This allowed for a slight overlap to reduce the amount of light lost to gaps. Conical funnels of aluminized mylar preceded the 5 inch Burle 8854 PMTs to facilitate better light collection as seen in Figure 3.16.

3.4.3 Lead Glass Calorimeter

The lead glass calorimeter (PbG), shown in Figure 3.17, was located at $z=33.2$ m and provided the second method for discriminating electrons from pions and muons. To do this, the energy deposited in the calorimeter was compared with the momentum measured in the magnetic spectrometer. The ratio $\frac{E}{p}$ should be 1 for any particles stopping in the lead glass, as all of its energy will be absorbed.

Two planes of lead glass crystals make up the calorimeter. The first plane, or

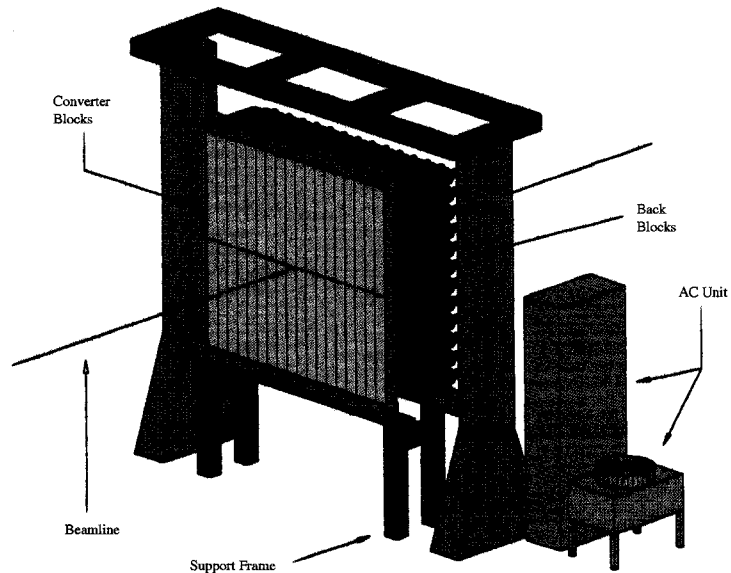


Figure 3.17: The E871 lead-glass calorimeter with an external cooling system.

”converter” plane consisted of 36 blocks arranged in an 18×2 array with each block measuring $10.9 \text{ cm} \times 90 \text{ cm} \times 10.0 \text{ cm}$ ($x - y - z$). The signal from each crystal was read out by a 7.62 cm photomultiplier tube aligned vertically along the $\pm y$ axis. Each block was wrapped in aluminized Mylar and black plastic, except for the readout and downstream ends.

The back plane, or “absorber” plane, contained 164 crystals stacked in a 14×12 array with each block having dimensions $15.3 \text{ cm} \times 15.3 \text{ cm} \times 32.2 \text{ cm}$ ($x - y - z$). These blocks were similarly wrapped in aluminized Mylar and black plastic as in the converter plane except for the downstream end where a 12.7 cm diameter photomultiplier tube was used to collect light and the upstream end where an ultraviolet light source could be used to cure the blocks as they are damaged by radiation over the course of the experiment. The downstream ends of the converter blocks were similarly left open to allow for curing.

As electrons enter the converter plane, they will most likely initiate an electro-

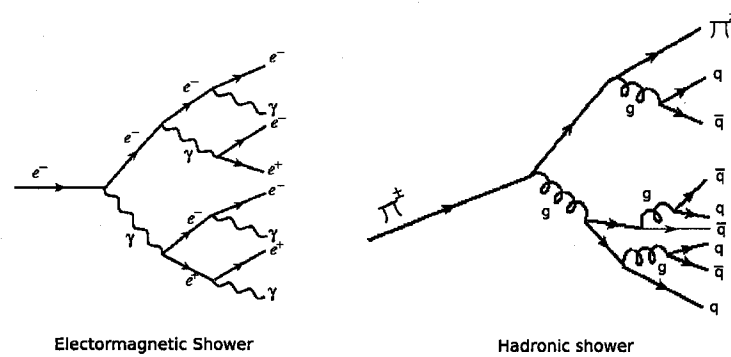


Figure 3.18: Examples of electromagnetic and hadronic showers.

magnetic shower. This shower is caused by bremsstrahlung radiation released as the electron slows as it traverses the lead glass. The light released in this process can produce an electron-positron pair which will be slowed in the lead glass, releasing more bremsstrahlung radiation. This process repeats until the photons released are no longer energetic enough to pair produce (Figure 3.18). These showers begin in the converter plane and continue on into the absorber plane where the entire shower can be stopped and the energy of the initial electron measured. Muons and pions can also produce electromagnetic showers but this process is greatly suppressed by their much greater mass. The electromagnetic fields of the atoms in the lead glass are not sufficiently strong to produce a shower. For the typical track momenta found in E871, muons are minimum ionizing and do not leave a large amount of their energy in the crystals. Hadronic showers can occur for the pion, which creates a jet of hadrons as shown in Figure 3.18. But with hadronic showers, the jet will not be contained inside the calorimeter. The energy measured for this type of process will be less than the momentum measured in the spectrometer, giving an $\frac{E}{p}$ ratio of less than one. The converter and absorber planes contain ~ 14 radiation interaction lengths for the electron, compared to only 1.2 hadronic interaction lengths for the pion. Due to the low energy deposition of both pions and muons, no discrimination

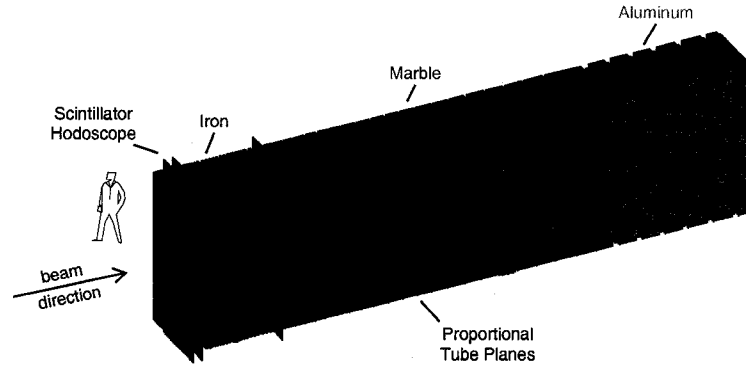


Figure 3.19: The muon hodoscope and muon rangefinder.

can be made between the two.

3.4.4 Muon Identification

The final component of the E871 detector is used to identify muons by measuring their range in a horizontal stack of absorber materials. As discussed earlier, electrons and pions will both lose energy by showering, electromagnetically for electrons, and hadronically for pions. The muon is 200 times heavier than the electron which suppresses its ability to induce electromagnetic showers and, as it is a lepton, it cannot shower hadronically. In the momentum region accepted in the E871 detector, between 1 – 10 GeV/c, muons are minimum ionizing particles; i.e., the rate of energy lost due to ionization of atoms as the charged lepton passes through the material is at or near its minimum value as described by the modified Bethe-Bloch formula:

$$-\frac{dE}{dx} = \frac{4\pi N_a r_e^2 m_e c^2 z^2 Z \rho}{A \beta^2} \left[\frac{1}{2} \ln \frac{2m_e c^2 \beta^2 \gamma^2 T_{max}}{I^2} - \beta^2 - \frac{\delta}{2} - \frac{C}{Z} \right]. \quad (3.4)$$

In Eq. (3.4), Z , A , and ρ are the atomic number, atomic mass, and density of the ionized matter, I is the mean excitation potential, and T_{max} is the maximum

energy exchanged in a collision. The final two terms, δ and $\frac{C}{Z}$ are used to correct for density effects at high particle energy and to correct for the assumption of stationary electrons at low particle energy, respectively. With the proper choice of absorber materials, electrons and pions can be made to give up their energy very quickly, while muons continue on for many meters, giving minimal energy to the absorber as they travel.

The muon identification system was designed so that the muon would travel through a series of absorbers and active detector elements such that it would reach each active element after losing 5% of its momentum in the absorber which precedes it; see Figure 3.19. In this fashion, the momentum of the particle can be determined by noting the last detector element that fired in the stack. The identity of the particle can be found by comparing the momentum determined by the muon identification system with the momentum determined by the magnetic spectrometer. If these two measurements agree, then the track is a muon. If the momentum found in the spectrometer is much higher than that found in the range stack, then the track was either a pion or an electron which did not shower in the lead glass.

Table 3.3 shows a list of the absorbers used, their thickness and the z -position of each. Also shown are the active detector elements inter-spaced in the absorbers (which will be described in the following sections) along with the momentum that a particle must have to reach that deep into the stack. Note that by the time a track reaches the active detector element MHO X0, it had to travel through the lead glass calorimeter and 45.72 cm of iron. A pion reaching this point had to travel almost 4 hadronic interaction lengths, at which point 95% would have created a hadronic shower and been absorbed, whereas a muon would need a momentum of 1 GeV/c to reach the same detector element.

| Z(cm) | Material | Gap- $\vec{p}_{stop}(\text{GeV}/c)$ | Z(cm) | Material | Gap- $\vec{p}_{stop}(\text{GeV}/c)$ | Z(cm) | Material | Gap - $\vec{p}_{stop}(\text{GeV}/c)$ |
|-------|----------|--|-------|------------|--|-------|---------------|---|
| 0 | 12" Fe | - | 256 | 3" Fe | - | 954 | 21" Marble | - |
| 32 | MHO X1 | 1-0.80 | 267 | MRG 19 X | 20-2.35 | 1010 | MRG 39 X | 40-6.25 |
| 41 | 2" Fe | - | 270 | 4" Fe | - | 1013 | 21" Marble | - |
| 47 | MRG 01 Y | 2-0.85 | 282 | MRG 20 Y | 21-2.45 | 1069 | MRG 40 Y | 41-6.75 |
| 49 | 2" Fe | - | 285 | 4" Fe | - | 1072 | 21" Marble | - |
| 55 | MRG 02 X | 3-0.90 | 297 | MRG 21 X | 22-2.60 | 1129 | MHO Y2 | 42-7.00 |
| 59 | 2" Fe | - | 300 | 4" Fe | - | 1138 | 24" Marble | - |
| 64 | MHO X0 | 4-1.00 | 312 | MRG 22 Y | 23-2.75 | 1201 | MRG 41 X | 43-7.25 |
| 73 | MHO Y0 | 4-1.00 | 315 | 4" Fe | - | 1205 | 24" Marble | - |
| 82 | 2" Fe | - | 327 | MRG 23 X | 24-2.90 | 1271 | MRG 42 Y | 44-7.75 |
| 87 | MRG 03 X | 5-1.05 | 330 | 4" Fe | - | 1274 | 24" Marble | - |
| 90 | MRG 04 Y | 5-1.05 | 343 | MRG 24 Y | 25-3.10 | 1338 | MRG 43 X | 45-8.00 |
| 92 | 2" Fe | - | 346 | 4" Fe | - | 1341 | 27" Marble | - |
| 100 | MRG 05 Y | 6-1.10 | 357 | MX2 | 26-3.25 | 1413 | MRG 44 Y | 46-8.30 |
| 103 | 2" Fe | - | 366 | 12" Marble | - | 1417 | 27" Marble | - |
| 108 | MRG 06 X | 7-1.15 | 398 | MRG 25 X | 27-3.35 | 1490 | MRG 45 X | 47-8.70 |
| 110 | MRG 07 Y | 7-1.15 | 401 | MRG 26 Y | 27-3.35 | 1493 | 27" Marble/Al | - |
| 113 | 2" Fe | - | 403 | 12" Marble | - | 1565 | MRG 46 Y | 48-9.10 |
| 120 | MRG 08 X | 8-1.20 | 435 | MRG 27 X | 28-3.55 | 1569 | 30" Marble/Al | - |
| 123 | 2" Fe | - | 438 | 12" Marble | - | 1647 | MRG 47 X | 49-9.50 |
| 129 | MRG 09 Y | 9-1.30 | 471 | MRG 28 Y | 29-3.70 | 1651 | 30" Marble/Al | - |
| 134 | 2" Fe | - | 474 | 12" Marble | - | 1729 | MRG 48 Y | 50-9.80 |
| 141 | MRG 10 X | 10-1.35 | 507 | MRG 29 X | 30-3.90 | 1733 | 30" Marble/Al | - |
| 144 | 2" Fe | - | 510 | 15" Marble | - | 1811 | MRG 49 X | 51-10.25 |
| 151 | MRG 11 Y | 11-1.40 | 551 | MRG 30 Y | 31-4.15 | 1815 | 33" Marble/Al | - |
| 155 | 2" Fe | - | 554 | 15" Marble | - | 1902 | MRG 50 Y | 52-10.80 |
| 162 | MRG 12 X | 12-1.55 | 596 | MRG 31 X | 32-4.30 | 1906 | 33" Marble/Al | - |
| 164 | 2" Fe | - | 599 | 15" Marble | - | 1992 | MRG 51 X | 53-11.05 |
| 172 | MHO Y1 | 13-1.60 | 639 | MRG 32 Y | 33-4.40 | 1995 | 21" Marble/Al | - |
| 180 | 3" Fe | - | 642 | 15" Marble | - | 2052 | MRG 52 Y | 54-11.95 |
| 189 | MRG 13 X | 14-1.65 | 682 | MRG 33 X | 34-4.75 | 2055 | 3" Marble | - |
| 194 | 3" Fe | - | 686 | 18" Marble | - | | | |
| 203 | MRG 14 Y | 15-1.80 | 735 | MRG 34 Y | 35-5.00 | | | |
| 206 | 3" Fe | - | 738 | 18" Marble | - | | | |
| 216 | MRG 15 X | 16-1.85 | 787 | MRG 35 X | 36-5.25 | | | |
| 219 | 3" Fe | - | 791 | 18" Marble | - | | | |
| 228 | MRG 16 Y | 17-1.95 | 840 | MRG 36 Y | 37-5.50 | | | |
| 231 | 3" Fe | - | 843 | 18" Marble | - | | | |
| 240 | MRG 17 X | 18-2.10 | 891 | MRG 37 X | 38-5.75 | | | |
| 244 | 3" Fe | - | 895 | 21" Marble | - | | | |
| 253 | MRG 18 Y | 19-2.25 | 950 | MRG 38 Y | 39-6.00 | | | |

Table 3.3: Muon range stack material placement and stopping momentum by detector plane

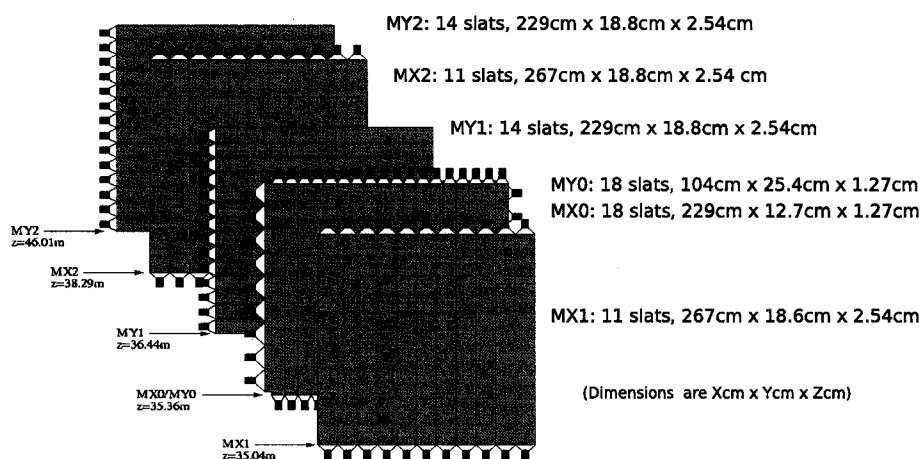


Figure 3.20: The layout of the six planes of scintillators used in the muon hodoscope.

Muon Hodoscope

The stack of absorbers and detector elements was built as one large unit but actually contains two separate systems: the muon hodoscope and the muon rangefinder. The hodoscope is made up of 6 segmented planes of Bicron BC408 scintillator. The dimensions and locations of each plane can be found in Figure 3.20. Each scintillator was read out by a Phillips XP2262 photomultiplier tube which was attached through a light guide and optical cookie to maximize the light collected. The x -viewing planes were read out on both ends, while the y -viewing elements were only read out on one end. The plane Y0 was the exception as it consisted of two distinct halves, one for beam left and one for beam right so that each half was read out with a photomultiplier tube. X0 and Y0 were part of the level 1 trigger, and the separation of the Y0 plane into two halves allowed for the association of the tracks made in the hodoscope with the tracks made in the left and right side of the magnetic spectrometer.

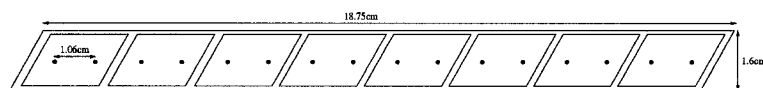


Figure 3.21: A cross section of an 8-channel extruded aluminum segments used in the 52 proportional counters planes of the muon rangefinder.

3.4.5 Muon Rangefinder

The muon rangefinder consisted of 52 proportional counters oriented in both the x and y direction interspersed in the absorber material such that the muon loses 5% of its momentum between successive counters. Each plane was made up of 8-channel extruded aluminum segments bonded in an edge to edge fashion. Each segment was 18.75 cm by 1.55 cm and oriented at a 60° angle from the horizontal as seen in Figure 3.21. The angular nature of the extruded planes allows for overlap of the active regions without needing multiple layers of counters at each station.

The x -oriented counters were 12 extrusions wide and 301 cm long, and the y -oriented ones were 16 extrusions wide with a length of 225 cm. Each cell contains two evenly-spaced, gold-plated tungsten wires $76.2 \mu\text{m}$ in diameter held under tension. The wires were kept at a potential of +2600V. The cells were filled with an argon-ethane gas mixture (49.2%-49.2%) with a small amount of ethanol (1.6%) added. Just as in the drift chambers described earlier, the passage of a charge particle in the gas-filled cells causes ionization of electrons. The ionized electrons accelerate toward the sense wire which further ionizes the gas. The resulting avalanche of charge is collected along the sense wires and recorded. The rangefinder will stop minimum-ionizing muons with momenta up to 11.95 GeV/ c .

CHAPTER 4

Trigger System

4.1 Overview

Over the two-year run of E871, the products of K_L^0 decay events were recorded by the detector at a rate on the order of 10^6 Hz. The data acquisition system (DAQ) was designed to eliminate much of the unwanted background decays in hardware in order to reduce the burden on the data tape system. The tape system used to store the data could handle a signal rate of $\approx 10^2$ Hz. Several layers of triggers were used to quickly sift through information from the trigger scintillator counters and particle identification systems and pick out possible two-body events or four-body events with two tracks carrying a large fraction of the invariant mass. The process begins with the triggering of a valid Level 0 (L0) event which only checks the path of the primary tracks. It is then passed to the Level 1 (L1) trigger, which adds a particle identification requirement. A signal for a valid L1 event is then sent to the Readout Supervisor (RS) which is the brains of the triggering system. The RS sends the information stored in the data crates to the Dual Port Memory (DPM) system to await further processing. The RS then prepares the system for the next event by

resetting the L0 and L1 triggers. The DPM system stores the event data in eight crates until retrieved by one of eight high speed Silicon Graphic (SGI) processors to begin the crude event reconstruction required in the Level 3 (L3) trigger. Events that pass all three triggers are sent to an IBM RS/600 computer and stored on high-capacity hard drives. Once a 200 megabyte block of data was collected, it was written to a 4mm Digital Audio Tape (DAT). An overview of the triggering process can be found in Figure 4.1.

4.2 Level 0

The triggering process begins when a charged particle traverses the trigger scintillating counters on each side of the beam-line. If the signals from the six counters (the left and right sides of TSC1 and TSC2, with TSC2 having both x and y -measuring planes) form a coincidence in time, the L0 trigger will examine the event more closely. The coincidence requirement ensures that the measured tracks are from the same K_L^0 decay event. The L0 trigger allows two types of events to pass, non-parallel decays and parallel decays, and can handle raw event rates $\approx 10^6$ Hz.

Non-parallel decays are events which pass the coincidence requirement but no cuts are placed on the position of hits in the TSCs. The events are wholly uninteresting except for calibration of the detector and for measuring raw filtering rates. The signal events for E871 are encompassed in the second type of L0 trigger, the parallel events. As described in Chapter 3, the E871 spectrometer magnets are tuned to have two-body K_L^0 decay tracks leave the downstream end of the spectrometer parallel to the beam-line. The Level 0 trigger measures the degree to which two tracks are parallel by comparing the x -slat hit in the upstream TSC with the slat hit in the downstream TSC (Figure 4.2). The limit set by the L0 trigger is $\delta_{slat} = \pm 2$

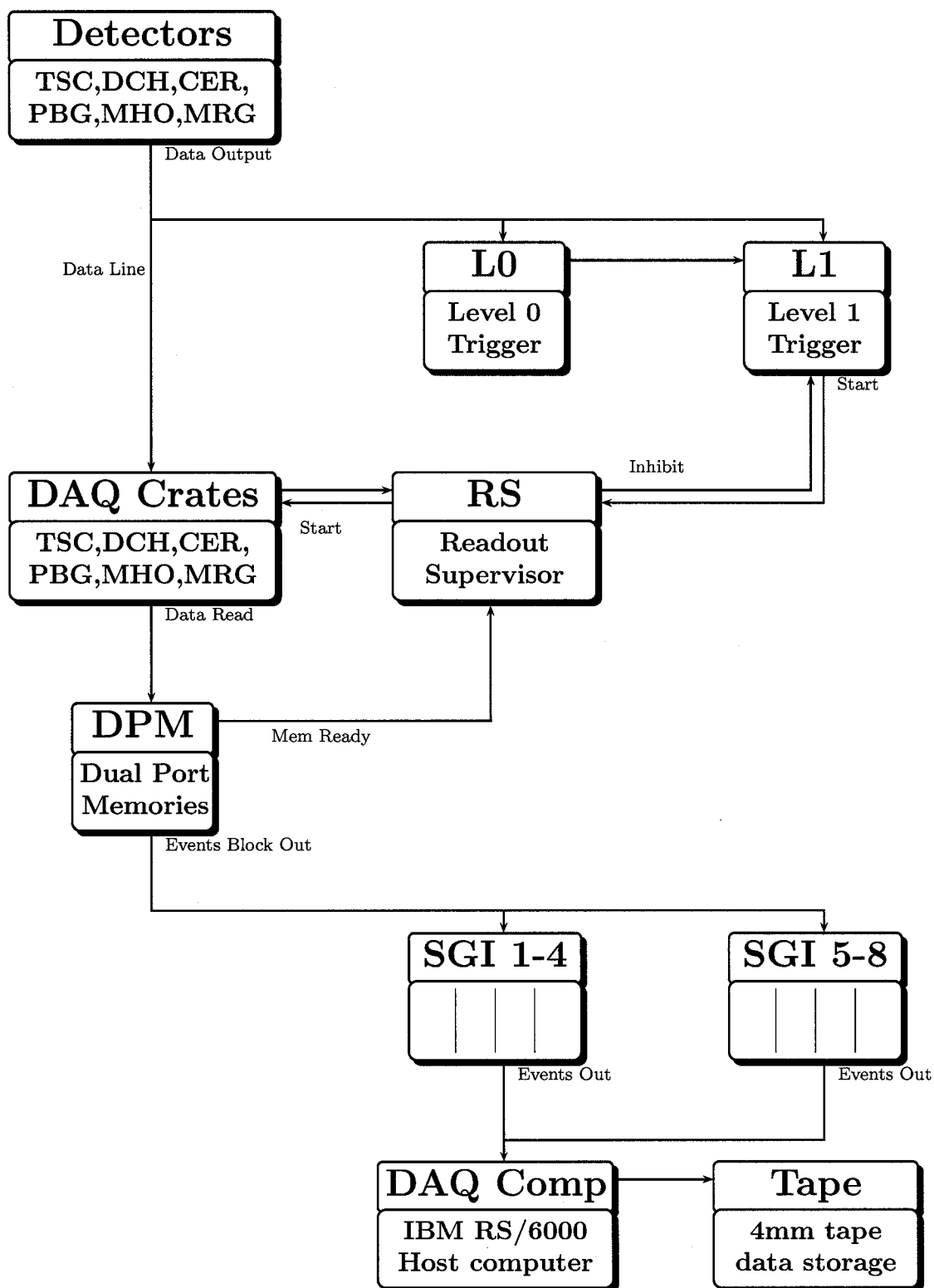


Figure 4.1: E871 DAQ system overview.

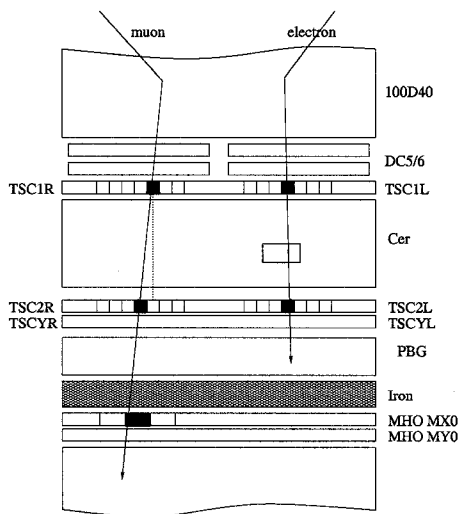


Figure 4.2: An example of a L0/L1 trigger.

which is a 31 mrad angular deviation from the parallel. Events which satisfy either the parallel or nonparallel requirements are sent on to the L1 trigger for further analysis.

4.3 Level 1

The Level 1 trigger takes the L0 parallel trigger information and adds particle identification. By using data from the Čerenkov counter and the muon hodoscope, the L1 system classifies each event into one of five categories: μe , $e\mu$, $\mu\mu$, ee , and $\pi\pi$ (minimum bias, MB) with the first listed particle corresponding to the left track. The tracks are also required to have a coincidence between the TSC signals and signals from the drift chambers DC5 and DC6. Each track is assigned a particle type by comparing it to the signature for a muon, electron, and pion:

- μ^\pm – Timing coincidence in DC5, DC6, and the TSCs, with a signal in the muon hodoscope. Loose spatial correlation is required.

- e^\pm – Timing coincidence in DC5, DC6, and the TSCs, with a signal in the Čerenkov counter. Loose spatial correlation is required in each.
- π^\pm – Timing coincidence in DC5, DC6, and the TSCs, with no signal in either the Čerenkov counter or the muon hodoscope. Loose spatial correlations are required here as well.

All μe , $e\mu$, $\mu\mu$, ee events which passed the L0 parallel trigger are sent on to the Level 3 trigger system, while only a fraction of the MB events is allowed to pass. The parallel MB events are prescaled by a factor of 1000, and the non-parallel MB events have a prescale of 10^4 . The L1 trigger reduces the ~ 250 kHz incoming event rate to *sim*10 kHz that is then sent to the Level 3 trigger.

4.4 Level 3

The Level 3 (L3) triggering system was accomplished in "software" by using eight SGI V35 processors to analyze the hit patterns in the forward spectrometer and do a crude event reconstruction. The event data are stored in eight Dual Port Memory (DPM) crates connected via a VME backplane. Each can each hold information on 3000 events. With half of the DPM's in use every spill, 12000 events/spill can be reconstructed with the L3 trigger. Upon processing, each event is checked for quality by examining the number of hits left by decay tracks in the drift chambers. Each plane in the straw drift chambers and hexagonal drift chambers, SDC1, SDC2, SDC3, DC5 and DC5, must contain at least two hits for x -viewing planes but no more than 250, and one hit for y -viewing planes but no more than 150. SDC4 had a minimum hit requirement of one for both x -viewing and y -viewing planes and a maximum of 250 for x -viewing and 150 for y -viewing. The ability to reconstruct a decay track with precision is directly related to the number of hits in

each plane. An event with too few hits will not allow for a track's path to be found, and too many will not allow a unique path to be determined.

The simple event reconstruction uses the hit clusters found in the drift chambers along with the overall p_T kick of the spectrometer magnets to find a track in each arm of the spectrometer. The two tracks are then projected back into the decay tank to find the vertex by determining their distance of closest approach (DOCA). The reconstructed vertex must fall between $z = 8$ m and $z = 21.5$ m and have a DOCA value of less than 70 cm, or the event is discarded. The transverse momentum of the decay and the invariant mass are also used as a determining factor on event quality. The total transverse momentum of the event must be less than 60 MeV/c and the invariant mass must exceed 460 MeV/c². These kinematic cuts depended on the event's classification as determined in the L1 trigger since the particle's mass figures greatly into the calculations. Events tagged as MB were reconstructed under a $K_L^0 \rightarrow \pi^+\pi^-$ hypothesis but were not subjected to an invariant mass cut. All events passing these cuts were sent to the IBM RS/6000 host computer for storage to await being written to 4mm DATs. The L3 trigger had a pass rate of $\sim 3\%$ leading to a data rate of 110 Hz being written to tape.

CHAPTER 5

Offline Analysis

5.1 Overview

The goal of the E871 offline software is to fully reconstruct an event's kinematic quantities such as track path, energy, momentum, and vertex position from the electronic information provided by the detectors during the run. A Monte Carlo event generator is incorporated in the software which allows artificial events to be analyzed in the same way as real events. Nine stages are used in the reconstruction (Figure 5.1) with each stage building a better description of the event based on the information gained in the previous one.

Stages one through four are used to create the Monte Carlo events. A K_L^0 is generated with a random momentum, decay vertex and decay time based on the energy spectrum and profile of the neutral beam used in E871. A specific decay channel or set of decay channels is supplied by the user. The decay products are then "swum" through each detector to generate appropriate ADC and TDC information that takes into account real detector responses and efficiencies, as well as multiple scattering. The hits are then packed for writing in an identical fashion

as a real event. Stages five and six unpack the hit information and sort it into arrays corresponding to the electronics for each detector element. The physical quantities such as deposited energy, distance of closest approach of a track to a wire in a drift chamber, and event time associated with the electronic information are calculated from calibration arrays specific to each detector element. Stages seven, eight, and nine reconstruct tracks in the spectrometer based on pattern recognition software, associate those tracks with hits in the particle identification counters, and refit the tracks using two independent fitting routines. The methods used in the last three stages will be discussed further.

5.2 Pattern Recognition

By the end of stage six, the drift times and distances for each wire are calculated and stored in an array but up to this point the spatial relationship of the chambers that have registered activity has not been taken into account. Stage seven looks at the hit information of each wire and attempts to find a physical path through the spectrometer that would account for the signals found in each chamber. This process is called Pattern Recognition (Patrec) and is a series of routines which must be satisfied if an event is to be considered for further refinement. If an event fails any of the Patrec routines, a flag is set and the event is killed. There are 22 planes of active drift chambers in the spectrometer, six x -viewing and five y -viewing on each spectrometer half (left/right). In the first step, a check is made to see if there was at least one good hit in each active plane, or if the plane was too noisy to retrieve any reliable results. A good hit is defined as one whose measured distance of closest approach (DOCA) falls in the allowed region. An event that has four planes with more than 100 hits each is considered too noisy. Next, each plane is searched for groups of at least two geometrically contiguous hit wires in different layers of an

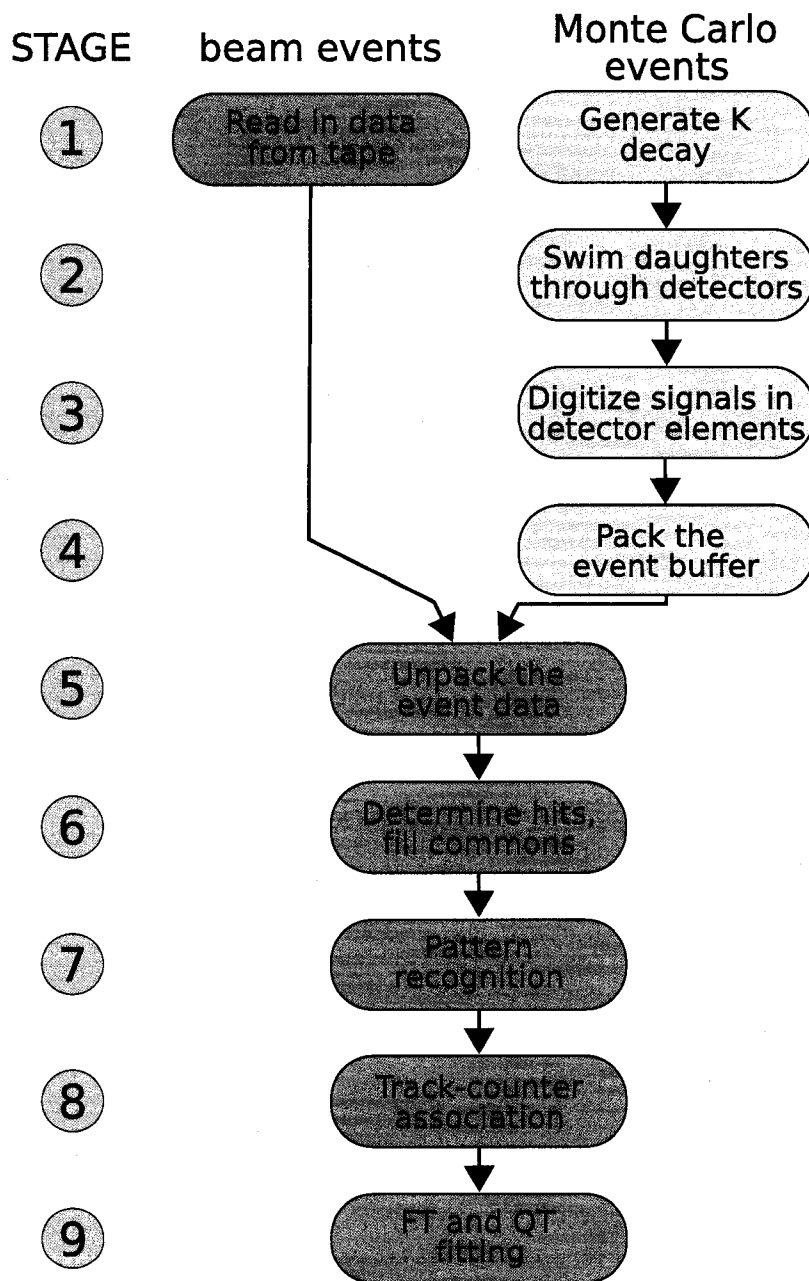


Figure 5.1: A Flow chart for the stages in the E871 offline analysis software.

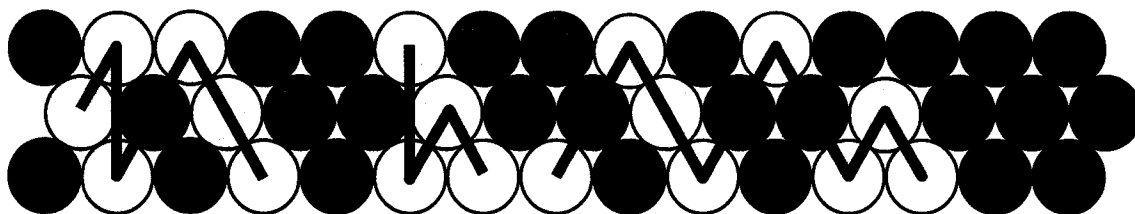


Figure 5.2: An Illustration of three clusters in a drift chamber which demonstrate the meaning of “geometrically contiguous”. The yellow cells indicate “good hits”.

active plane, called clusters (Figure 5.2). Each cluster is considered a possible point at which a decay product could have passed. Starting at the most downstream x (y) plane in the spectrometer, the search for two-dimensional prototracks is begun by considering all possible combinations of six (five) clusters, one from each x (y) viewing plane. If the slope between consecutive clusters fall within certain tolerances, the path is kept and stored for further refinement. If no allowed paths are found or if too many possible paths are found, Patrec exits and the event is killed.

A cluster can contain up to 20 hit wires for an x -viewing plane and 10 hit wires for a y -viewing plane. In order to reach the tracking resolution necessary for adequate event reconstruction, the wires hit inside each cluster by a decay product must be determined. To this end, a segment is defined as a set of one, two or three geometrically contiguous wires that register hits and that is not contained inside a larger segment. An example of a set of five segments can be seen in Figure 5.3. A search is made for all sets of segments, one segment for each cluster in a path, that would best represent the two-dimensional path found from the clusters. To find the best segment for each cluster-set, the candidates are scored by performing a likelihood calculation using slope matching of clusters to determine whether the candidate is noise or a true hit. Once all segment sets are found and scored, they are “deghosted”. Many of the segment sets found differ by only one or two out of the five or six possible segments and are most likely trying to represent the same

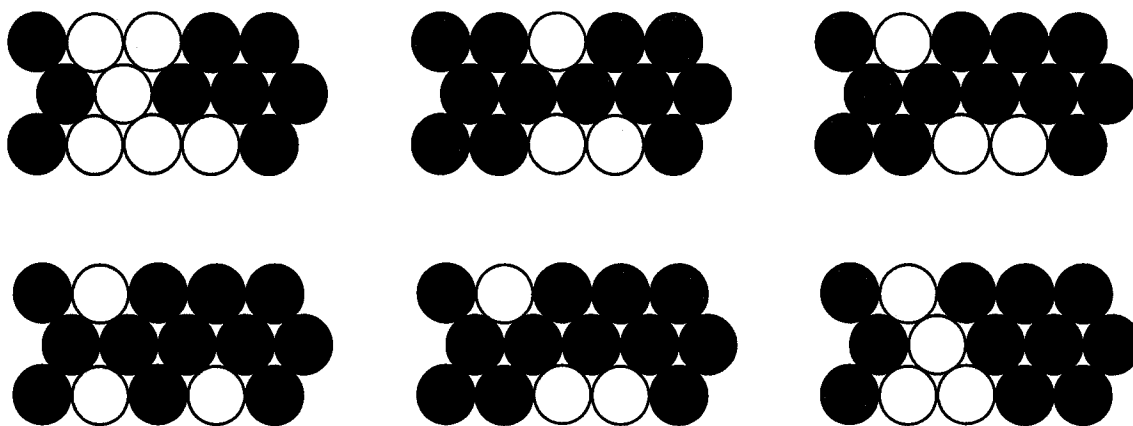


Figure 5.3: An illustration of 5 segments (red cells) inside 1 cluster (yellow cells). Each segment is mutually exclusive in that no segment can be fully contained in another.

track but that Patrec picked one of the clusters incorrectly. The differing segments are usually in the forward most planes of the spectrometer as these are the most noisy. To eliminate the “ghost” set, the one with the best score is kept, unless both sets have comparable scores in which case neither can be eliminated and both are passed on for further refinement.

At this point, Patrec contains a list of possible two-dimensional x paths and two-dimensional y paths for both the left and right halves of the spectrometer. The next step is to consider all possible combinations of x and y paths to find the best three-dimensional tracks (Terminology: “path” or “proto-track” is used for two-dimensional fits, while three-dimensional fits will be called “tracks”). Each track is separated into three sections, front, middle and rear. Each section contains two points in three-dimensions that form a line segment. To test the validity of the track, the line segments are projected to a point at the midpoint of the two magnets to examine how well they correlate. The line segments in the front and middle sections are projected to the midpoint of the first spectrometer magnet where the DOCA measurement takes place. Similarly, the line segments in the rear and middle sections are projected to the midpoint of the second magnet for another

DOCA measurement. If the DOCAs are less than 4 cm, then the track is kept. If no good tracks are found, Patrec exits. For all remaining tracks, the momentum of each track is calculated with a point-line method that uses the curvature of the particles path in each spectrometer magnet:

$$p = \frac{p_{kick}}{\Delta\theta}. \quad (5.1)$$

In Eq. (5.1), $\Delta\theta$ is the angular difference in the line segments in the x -direction before and after the magnet and p_{kick} is either the constant momentum kick (416 MeV/c or 216 MeV/c) or position-dependent momentum kick found in a lookup table. The momentum measured in the front and rear magnet must match to within 10% or the track is discarded. The actual momentum recorded for each track is a weighted average of that measured in the front and rear magnets.

The final step in pattern recognition is to calculate the vertex points for all possible left/right combinations of tracks and to rank the results. The vertex point is defined as the distance of closest approach between the left and right tracks when they are projected upstream from the line segments found between SDC1 and SDC2. The vertex result as well as the track pair information is kept if the vertex calculation satisfies the following conditions:

- The track-to-track DOCA is less than 10 cm.
- The z -position, z_0 , of the vertex is between 0.0 m and 30.0 m.
- $|\frac{x_0}{z_0}| \leq 0.050$ and $|\frac{y_0}{z_0}| \leq 0.025$, where (x_0, y_0, z_0) are the coordinates of the vertex.

The surviving tracks are sorted according to the track-to-track DOCA value with the tracks having the smallest DOCA listed first.

5.3 Track-Counter Association

The pattern recognition software used in stage seven finds the path that best fits the hits in the spectrometer, but the type of particle that traversed the path is unknown and irrelevant until this point in the analysis. Stage eight compares the path of a decay particle in the spectrometer with the hits registered in the particle identification counters at the rear of the detector to determine if a particle traveling on that path could have caused the hits seen in the counters, and if so, the type of particle that would give those types of hits. For each track that passes pattern recognition, the track-counter association routine is executed. The path of each track is projected forward into the Cerenkov counter, through the lead glass calorimeter and into the muon hodoscope and rangefinder. The projected hits are digitized and compared to the “real” hits in the event to associate specific hits in each particle identification counter with a track in the spectrometer. Counter specific routines are called which examine the hits associated with a track and attempt to determine whether the particle was an electron, a muon or a pion. The Cerenkov counter and the lead-glass calorimeter are used to identify electrons and decide whether to tag a track as a “good”, “possible” or “non” electron. The muon hodoscope and rangefinder are used to discriminate muons from pions. These routines will tag a track as either a “good”, “possible” or “non” muon. The requirements to classify a track as an electron or muon are described in Sec. 6.3. A particle is determined to be a pion if it is neither a muon nor an electron.

5.4 Event Fitting

While pattern recognition provides a good initial guess at the kinematics of a K_L^0 decay and removes obviously bad events, the precision of its calculations is

limited by the approximations made for the sake of speed. Stage nine employs two fitting routines which build upon the track properties found in stage seven and uses more comprehensive methods for kinematic calculations. The full magnetic field map containing the three dimensional components of the field is used for momentum calculations whereas pattern recognition uses a transverse momentum kick approximated by either a constant field or by a field found from a look-up table based on position. The non-linear effects of multiple scattering are incorporated to account for the deflection of the particle path from a straight line. The two fitters, which are described in the following sections, use independent methods to provide a check on the consistency of event reconstruction. The FT fitter uses χ^2 minimization techniques to find the best track and vertex parameters for each event. The QT fitter employs track and momentum matching to find the track parameter for the front (SDC1, SDC2, SDC3) and rear (SDC4, SDC5, SDC6) sections of the spectrometer and averages them in an appropriate way to calculate the decay kinematics. The object of the following sections is to outline the algorithm used by each fitter. For more a detailed description of the FT and QT routines, the reader is directed to [36], [37], and [38].

5.4.1 FT Fitter

The FT fitter uses a χ^2 minimization technique to find a set of parameters $\vec{\alpha}$ that best describes the “true” path of the particle, where

$$\vec{\alpha} = \left(x, y, \frac{dx}{dz}, \frac{dy}{dz}, \frac{q}{p} \right), \quad (5.2)$$

x and y are the coordinates of a point on the downstream end of the vacuum window on the decay tank, $\frac{dx}{dz}$ and $\frac{dy}{dz}$ measure the direction of the track and $\frac{q}{p}$ gives the charge and momentum of the particle. The fitter uses the parameters found by the pattern recognition routine in stage seven for the initial guess of $\vec{\alpha}$. From this initial point

and momentum, the location that the theoretical track hits each layer of each drift chamber is recorded as a theoretical data point, x_i^{th} . In order to describe the degree of disagreement between the theoretical track and the data, a formula for a χ^2 value is introduced:

$$\chi_{track}^2(\vec{\alpha}) = \sum_i^{N_{par}} \sum_j^{N_{par}} (x_i^{data} - x_i^{th}(\vec{\alpha})) W_{ij}^x (x_j^{data} - x_j^{th}(\vec{\alpha})), \quad (5.3)$$

where the sums are over the number of layers hit by each track, which can be up to 28 points (18 x -layers, 10 y -layers).

The matrix W_{ij}^x is called the “weight matrix” and its inverse, the covariance matrix, is a measure of the errors that are introduced when the position of the particle is recorded experimentally. The diagonal components comprise the uncorrelated errors, such as the resolution of each drift chamber. The off-diagonal elements are the correlated errors which are mainly due to multiple scattering. For example, the difference in the position recorded in the downstream drift chambers will depend greatly on the amount of deflection caused by the upstream straw drift chambers. Since multiple scattering is dependent on the momentum of each track, the weight matrix must be recalculated from Monte Carlo each time the routine is called. The FT fitter then calls a routine that finds the set of parameters $\vec{\alpha}$ which minimizes the χ^2 formula above. This is done for all tracks that passed pattern recognition.

The second step taken by the FT fitters is to use the track fits to obtain the decay vertex kinematics for all possible left/right pairs. A χ^2 minimization technique similar to the track fitting is used. Instead of having actual data points with which to fit, now the track fit parameters $\vec{\alpha}_{L,R}$ are used as the “data”. The χ^2 equation to be minimized is now:

$$\chi_{vertex}^2(\vec{\beta}) = \sum_i^{N_{par}} \sum_j^{N_{par}} \left(\alpha_i^{data} - \alpha_i^{th} \right) W_{ij}^\alpha \left(\alpha_j^{data} - \alpha_j^{th} \right), \quad (5.4)$$

where $\vec{\alpha}$ is now a 10-vector made up of $\vec{\alpha}_L$ and $\vec{\alpha}_R$, and

$$\vec{\beta} = (x_L, y_L, \frac{dx_L}{dz}, \frac{dy_L}{dz}, \frac{q_L}{p_L}, x_R, y_R, \frac{dx_R}{dz}, \frac{dy_R}{dz}, \frac{q_R}{p_R}). \quad (5.5)$$

W_{ij}^α is a block diagonal 10×10 matrix consisting of the two 5×5 matrices found in the track fits. Since the vertex fit takes place inside the decay tank and the fit to the tracks is done to the downstream end of the vacuum decay window, W_{ij}^α must be slightly modified to account for the multiple scattering that would take place in the window. Once the minimization is complete, the fitted vertices are sorted according to the minimized χ^2 and the vertex with the lowest χ^2 is used in the analysis.

5.4.2 QT Fitter

The method used by the QT fitter is fundamentally different from that in the FT fitter in that it does not do any χ^2 minimization. QT fitting follows a process similar to pattern recognition but treats the front and rear sections of the spectrometer as independent. A hypothesis is made that all the information about the trajectories of the particles is found in the analysis of the front, and the back half is only used for a second momentum measurement and as a way to check the effectiveness of the fit. It is assumed that the data in drift chambers four, five and six are so distorted by multiple scattering that no information about the path of the particles in the decay tank can be extracted.

To start, the coordinates of the hits in each layer of a plane (either x or y) are averaged. In this manner, three x -points and two y -points are found in the front section while three x -points and three y -points are found in the rear (SDC3 does not contain a y -viewing plane). The extra y -point from SDC4 is not used in order to keep the analysis in both section identical. It will be used later as a measure of how well the y -components of the fit match the data. These five data points can be used to find the five parameters needed to specify a track from a specific longitudinal

point: x , y , $\frac{dx}{dz}$, $\frac{dy}{dz}$, $\frac{q}{p}$. Beginning with the outer most drift chamber, SDC1 in the front and SDC6 in the back, the path of the particle is projected inward to the next two drift chambers with the initial track parameter found in stage seven's pattern recognition. Based on the difference between the projected path and the data points, the track parameters are adjusted for a better match. This is done iteratively until the differences are below a threshold ($\approx 10 \mu\text{m}$). The two momentum measurements for the front and back section of the spectrometer are combined using a weighted average with the weights of each half's momentum being determined from Monte Carlo.

The quality of fit is determined by how well the two independent fits for each track compare. A χ^2 value for both the x and y views (Eq. (5.6) and Eq. (5.7)) is constructed from the position and direction cosine differences as well as from the momentum difference from the average. The x -view χ^2 is defined as

$$\chi_x^2 = \chi_{\delta p}^2 + \chi_{\delta x}^2 + \chi_{\delta\theta_x}^2 \quad (5.6)$$

with

$$\chi_{\delta p}^2 = \left(\frac{p_f - \bar{p}}{\sigma_{p_f}} \right)^2 + \left(\frac{p_b - \bar{p}}{\sigma_{p_b}} \right)^2, \quad \chi_{\delta x}^2 = \left(\frac{x_f - x_b}{\sigma_x} \right)^2 \quad \text{and} \quad \chi_{\delta\theta_x}^2 = \left(\frac{\theta_{x_f} - \theta_{x_b}}{\sigma_{\theta_x}} \right)^2,$$

and the y -view χ^2 is

$$\chi_y^2 = \chi_{\delta y}^2 + \chi_{\delta\theta_y}^2 + \chi_{\delta y_4}^2 \quad (5.7)$$

where the position and angular χ^2 have the same form as their x -counterparts and $\chi_{\delta y_4}^2$ measures the error in the y -position at the y -plane in SDC4.

Once all tracks have been fit, vertices are found for all possible left/right pairs. The direction cosines from the front half of the spectrometer are used along with the averaged momentum to project the path of the tracks into the decay tank. The track to track distance of closest approach defines the vertex of the pair. If the

DOCA is less than 10 cm, the vertex is kept and a χ^2 for the quality of the vertex fit is calculated. This is defined as

$$\chi_{vertex}^2 = \frac{\delta d^2}{(z_{SDC1} - z_{vertex})(\alpha + \frac{\beta}{p_L^2 + p_R^2})} \quad (5.8)$$

where δd is the track-to-track DOCA, z_{SDC1} and z_{vertex} are respectively the z -positions of the first straw drift chamber and the vertex, p_L and p_R are the respective track momenta, and α and β are parameters determined from Monte Carlo. All vertices that pass QT for the event are sorted according to the parameter

$$\xi = \chi_{vertex}^2 + \eta(\chi_L^2 + \chi_R^2), \quad (5.9)$$

where η is an empirical parameter and $\chi_{L,R}^2$ is the sum of the $\chi_{x,y}^2$ for that track added in quadrature.

Part III

Branching Fraction Measurement

CHAPTER 6

Monte Carlo Studies

6.1 Overview

Monte Carlo analysis is a simulation technique which can be used to explore the characteristics of an experiment under controlled situations. In E871, the Monte Carlo methods are coded into the data analysis routine which allows us to examine the response of each detector element and to develop event signatures for signal and background decays. For each event, a K_L^0 is generated, decayed through a user-defined branch, and the daughters transported through the detector. Hits are generated in the each element of the spectrometer, TSCs, and particle identification subsystems which include detector efficiencies, dead spots and multiple scattering to make the results of the simulation match the results of data runs as closely as possible. This chapter examines the results of Monte Carlo generated data to determine the properties and acceptance of the pion and e^+/e^- tracks that will enable us to classify an event as signal, normalization or background.

6.2 $K_L^0 \rightarrow \pi^+\pi^-e^+e^-$ Event Signature

The design of a detector must provide ways to differentiate between decay modes of interest such that it is unlikely that two modes would give the same response. In an ideal situation, the electronic signature would be unique in that no other mode or combination of modes could duplicate it. But in reality, detector resolution and efficiencies, accidental hits, and closely-related decay branches lead to background contamination.

As the original purpose of the E871 experiment was to search for rare two-body leptonic decays of the kaon, its detector was designed to maximize the acceptance for these branches while minimizing three-body backgrounds to the two body signal events. As described in Chapter 4, the trigger system was designed to limit the amount of data written to tape by selecting events that had two tracks with the correct charge whose reconstructed invariant mass was greater than 460 MeV under a decay hypothesis of $K_L^0 \rightarrow \pi^+\pi^-$, $K_L^0 \rightarrow e^+e^-$, $K_L^0 \rightarrow \mu^+\mu^-$, or $K_L^0 \rightarrow \mu^\pm e^\mp$. With this requirement, the search for $K_L^0 \rightarrow \pi^+\pi^-e^+e^-$ is limited to one in which two of the four decay products carry the majority of the invariant mass. At first glance, this could occur in one of four possible ways:

1. The $\pi^+\pi^-$ pair passes through the spectrometer, TSC and particle identification counters and is accepted by the trigger with the soft e^+e^- pair partially reconstructed or missing the spectrometer.
2. The e^+e^- pair passes through the spectrometer, TSC and particle identification counters and is accepted by the trigger with the soft $\pi^+\pi^-$ pair partially reconstructed or missing the spectrometer.
3. The π^+e^- pair passes through the spectrometer, TSC and particle identification counters and is accepted by the trigger with the soft π^-e^+ pair partially reconstructed or missing the spectrometer.

4. The π^-e^+ pair passes through the spectrometer, TSC and particle identification counters and is accepted by the trigger with the soft π^+e^- pair partially reconstructed or missing the spectrometer.

Two of the four products that are fully reconstructed in the spectrometer must have at least 460 MeV of the K_L^0 's invariant mass. Due to this requirement, $K_L^0 \rightarrow \pi^+\pi^-e^+e^-$ events will only be found in the E871 data set from option one. Option two is kinematically forbidden while options three and four are allowed, but suppressed due to very limited phase space. This work will be limited to searching for two full pion tracks and partial e^+/e^- tracks. The two pions will be referred to as the *primary* tracks as theirs are the tracks that must be fully reconstructed by pattern recognition, the FT and QT fitters, and the particle identification routines in order that the event be written to tape. The soft e^+e^- pair carries little of the K_L^0 's invariant mass and is unlikely to create hits in the entire spectrometer. For events where the e^+e^- pair does hit the front two straw drift chambers, their tracks will most likely be bent out of the spectrometer or into the beam plug due to the strength of the first spectrometer magnet as illustrated in Figure 6.1. These tracks will not be fully reconstructed, nor is there any way to positively identify them as electron-type. As such, they will be referred to as *partial tracking stubs*, or *stubs* for simplicity. In the following sections, the characteristic quantities of the primary tracks and the partial tracking stubs will be examined under various K_L^0 form factor hypotheses (see Chapter 2) to determine cuts that will allow identification of a set of tracks with the signal, the normalization or background events. A summary of the these cuts along with the efficiency of each can be found at the end of this section in Table 6.2 and Table 6.3 for the FT and QT fitters, respectively.

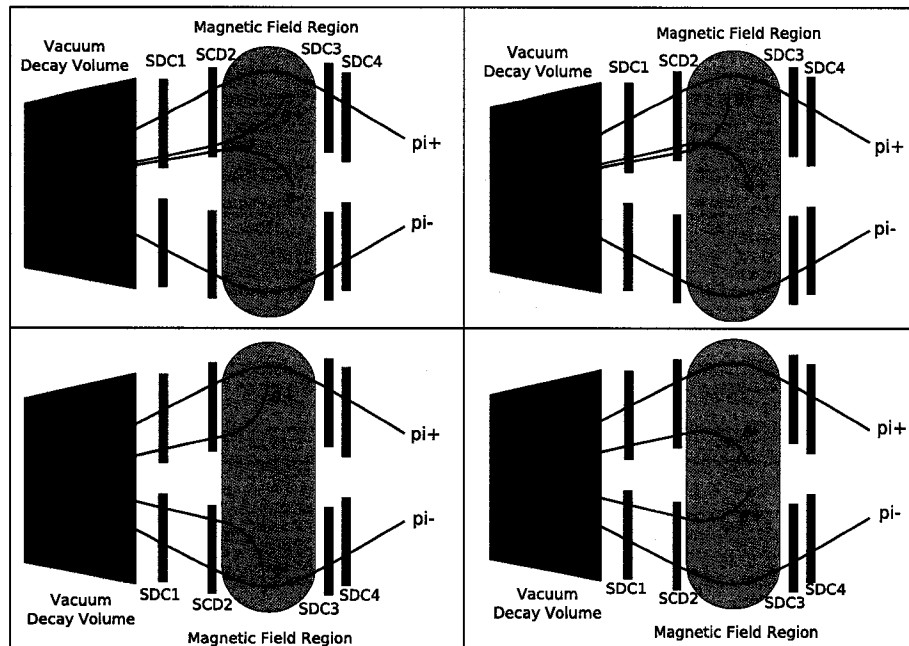


Figure 6.1: Possible $K_L^0 \rightarrow \pi^+\pi^-e^+e^-$ events accepted into the front half of the spectrometer. Due to their soft nature, the e^+e^- tracks rarely leave hits in more than SDC1 and SDC2.

6.3 Primary Pion Tracks

In order to verify that a set of tracks originated from a two-body or a four-body K_L^0 decay, we require that the tracks can be projected upstream into the vacuum decay region to form a vertex point. The quality of the vertex will depend on how well each track's kinematics are reconstructed in pattern recognition, and how they are subsequently fit using the independent FT and QT routines. In order to fully describe each track, the fitting routines will provide the track's momentum and direction cosine at the upstream end of the spectrometer, as well as a χ^2 value describing how well each fit matched the hits in the drift chambers. The tracks are then projected upstream into the decay tank where the vertex is formed by calculating the distance of closest approach (DOCA) between the tracks.

The track and vertex information of the primary pions is reconstructed inde-

pendently of how the track was created. The set of track properties that describes a good pion track in the detector must, therefore, be independent of whether the pion originated as part of the signal $K_L^0 \rightarrow \pi^+\pi^-e^+e^-$ or of the normalization $K_L^0 \rightarrow \pi^+\pi^-$. Thus, the cut values derived from the Monte Carlo must include data from both to ascertain if the cuts are not rejecting large portions of properly reconstructed two-body or four-body events. By applying these cuts to the signal and normalization samples equally, any errors introduced by these cuts will cancel in the final branching ratio calculation.

Track Quality

As described in Chapter 5, a track χ_T^2 is calculated as a measure of how well the projected track matches the hits recorded from each drift chamber. For the FT fitter, the χ_T^2 value depends on the number of degrees of freedom in the fit which is the number of drift chamber planes hit in the event. This can be anywhere from 28, where every plane (18 x -planes and 10 y -planes) has a recorded hit, to 17, where two x -planes are hit per chamber and one y -plane per chamber. The QT fitter uses the values for χ_x^2 and χ_y^2 found in Eq. (5.6) and Eq. (5.7), respectively, added in quadrature to find its χ_T^2 . The χ^2 for the left and right tracks are added in quadrature to find a total track χ_T^2 for the QT fitter.

The results for the FT and QT fitters be found in Figure 6.2 and Figure 6.3 respectively. The larger values of χ_T^2 in the plots indicate difficulty in reconstructing the track. Pions that decay in flight can cause kinks in the track as well as extra hits in the drift chambers caused by the decay electron. Accidental tracks or tracks from stub candidates, along with poor hit quality in the drift chamber can cause poor reconstruction due to using incorrect hits. A cut value of 25 for the FT χ_T^2 will exclude less than 1.5% of all events. For the combined χ_T^2 of the QT fitter, a nominal cut of 35 will also exclude less than 1.5% of events.

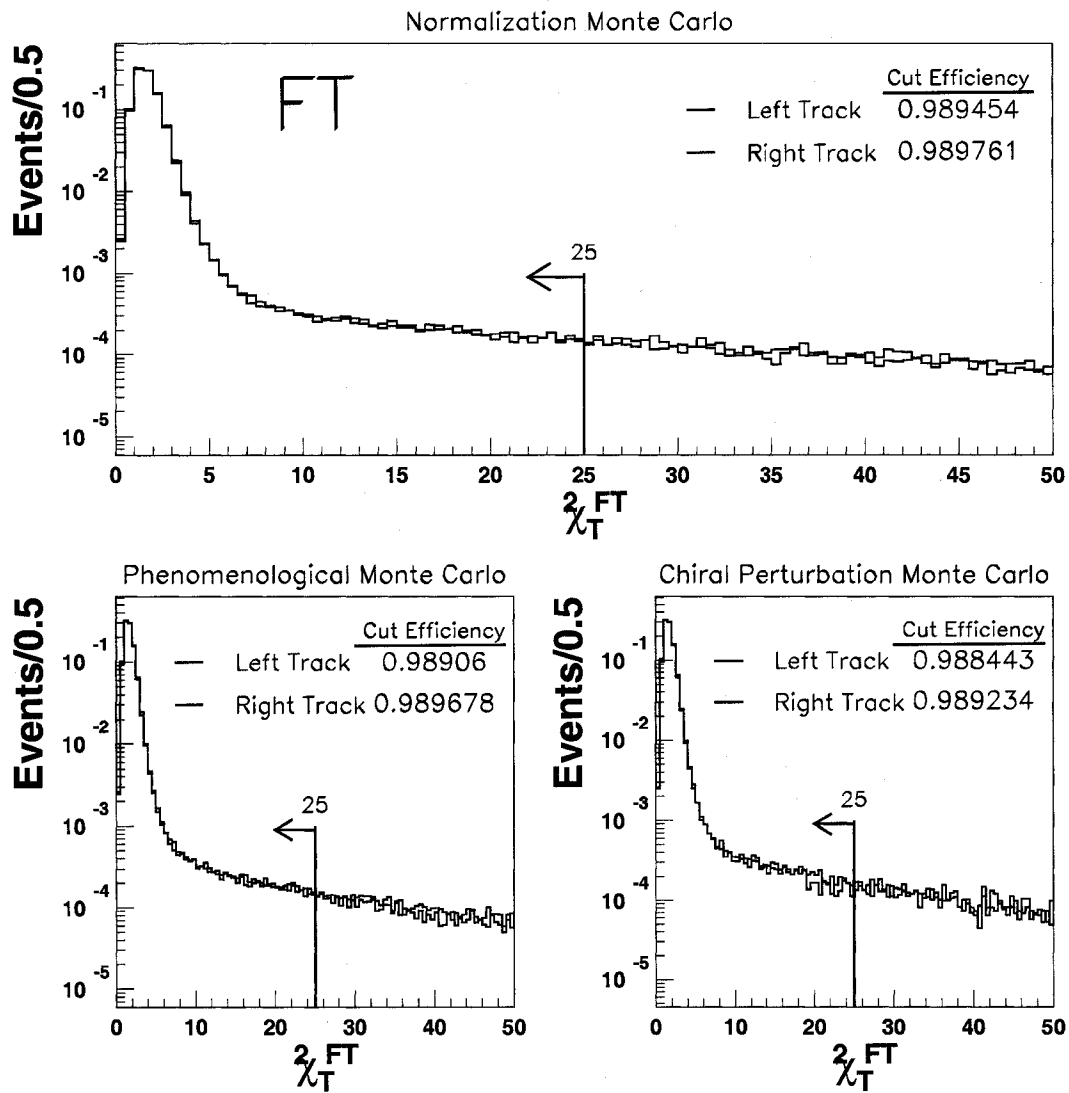


Figure 6.2: FT fitter χ_T^2 distributions for $K_L^0 \rightarrow \pi^+\pi^-$ and $K_L^0 \rightarrow \pi^+\pi^-e^+e^-$ with K_L^0 form factors are presented. A nominal cut value of 25 is shown.

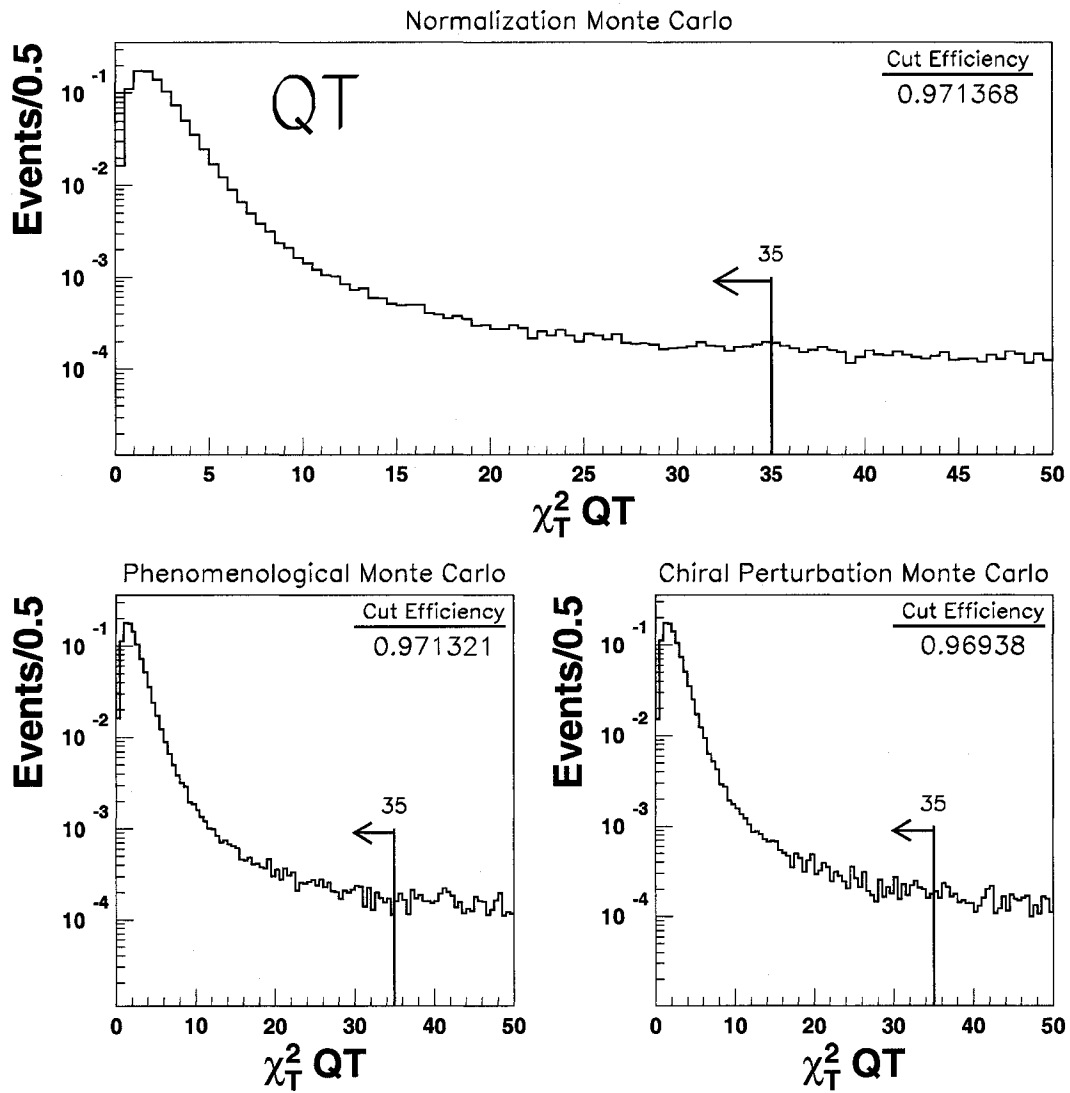


Figure 6.3: QT fitter χ_T^2 distributions for $K_L^0 \rightarrow \pi^+\pi^-$ and $K_L^0 \rightarrow \pi^+\pi^-e^+e^-$ with K_L^0 form factors are presented. A nominal cut value of 35 is shown.

Track Momentum

The design of the E871 detector places requirements on the momentum of each pion. The fiducial acceptance in the spectrometer is biased such that few tracks will have a momentum below 1 GeV/c. The muon hodoscope and the muon rangefinder were built with this acceptance in mind. A muon track must have at least 1 GeV/c to travel far enough into the layers of scintillator and iron to be correctly identified. Below this threshold, a pion and a muon will appear too similar to be distinguished. A low momentum cut of 1.05 GeV/c is placed on the momentum of each pion to ensure proper identification. Due to the small acceptance for low momentum events, this cut is $\sim 98\%$ efficient.

On the opposite end of the momentum spectrum, highly boosted kaons will produce daughter pions with large momenta. The acceptance of these events is small as many of the pions will enter the beam plug due to the decrease in opening angle between the pions. This decrease in acceptance, as well as the smaller probability of high momentum K_L^0 production, results in the steep drop-off of the high momentum tail in the momentum spectra of Figure 6.4 and Figure 6.5. Much of this tail must be eliminated due to the decrease in efficiency of the particle identification routines as the track momentum gets larger. The lack of statistics in this region did not allow for a detailed study of the detector response. High momentum pions and muons from pion decay are also more likely to escape from the muon rangefinder before depositing their entire energy. To limit the number of misidentified tracks, the momentum of each track will be required to be below 6.5 GeV/c. The requirement removes less than 2% of the events in the Monte Carlo samples.

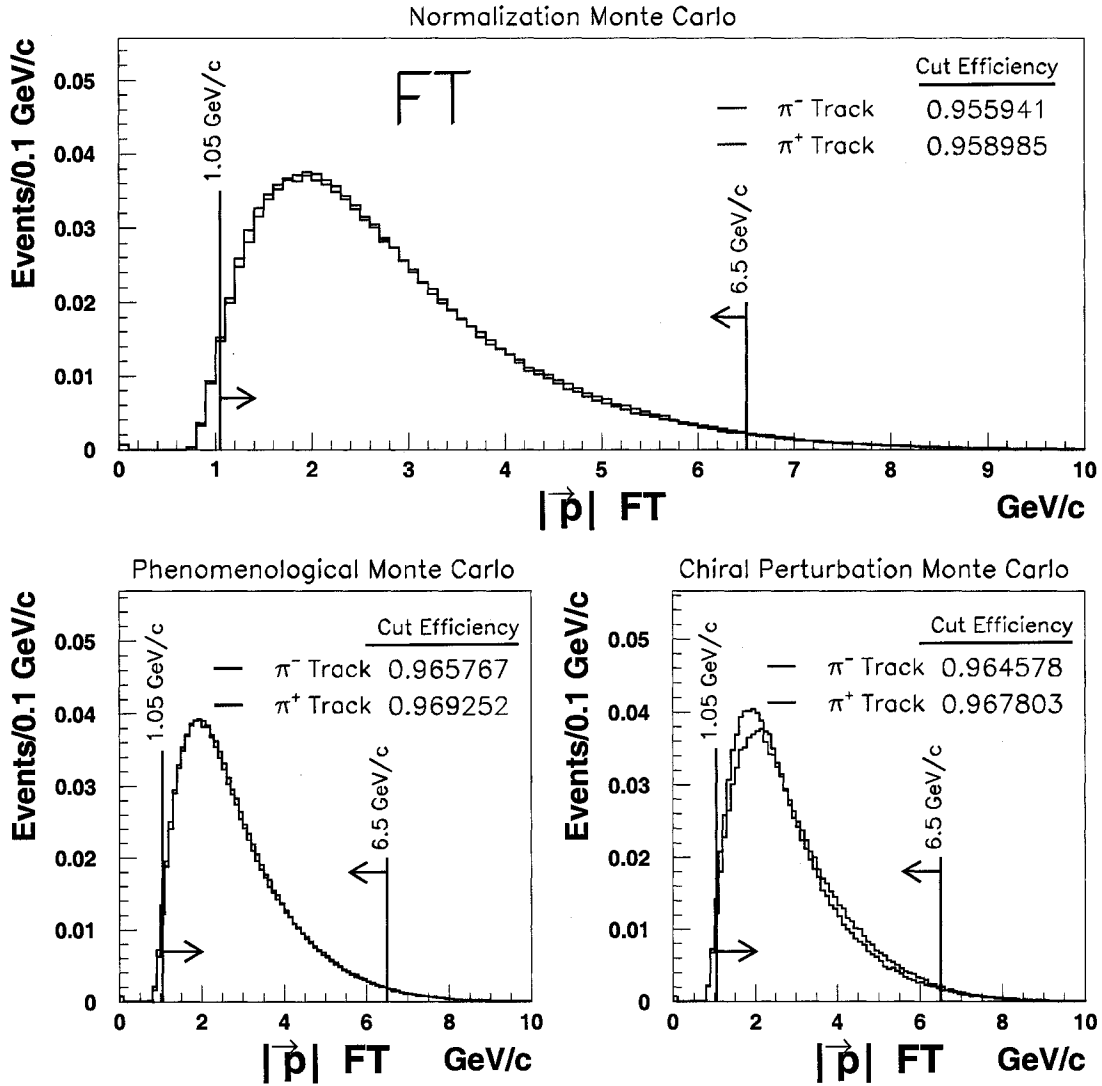


Figure 6.4: Pion momentum distributions for $K_L^0 \rightarrow \pi^+\pi^-$ and $K_L^0 \rightarrow \pi^+\pi^-e^+e^-$ with K_L^0 form factors calculated using the FT fitter are presented. The efficiency of the $1.05 \text{ GeV}/c < |\vec{p}| < 6.5 \text{ GeV}/c$ cut is listed.

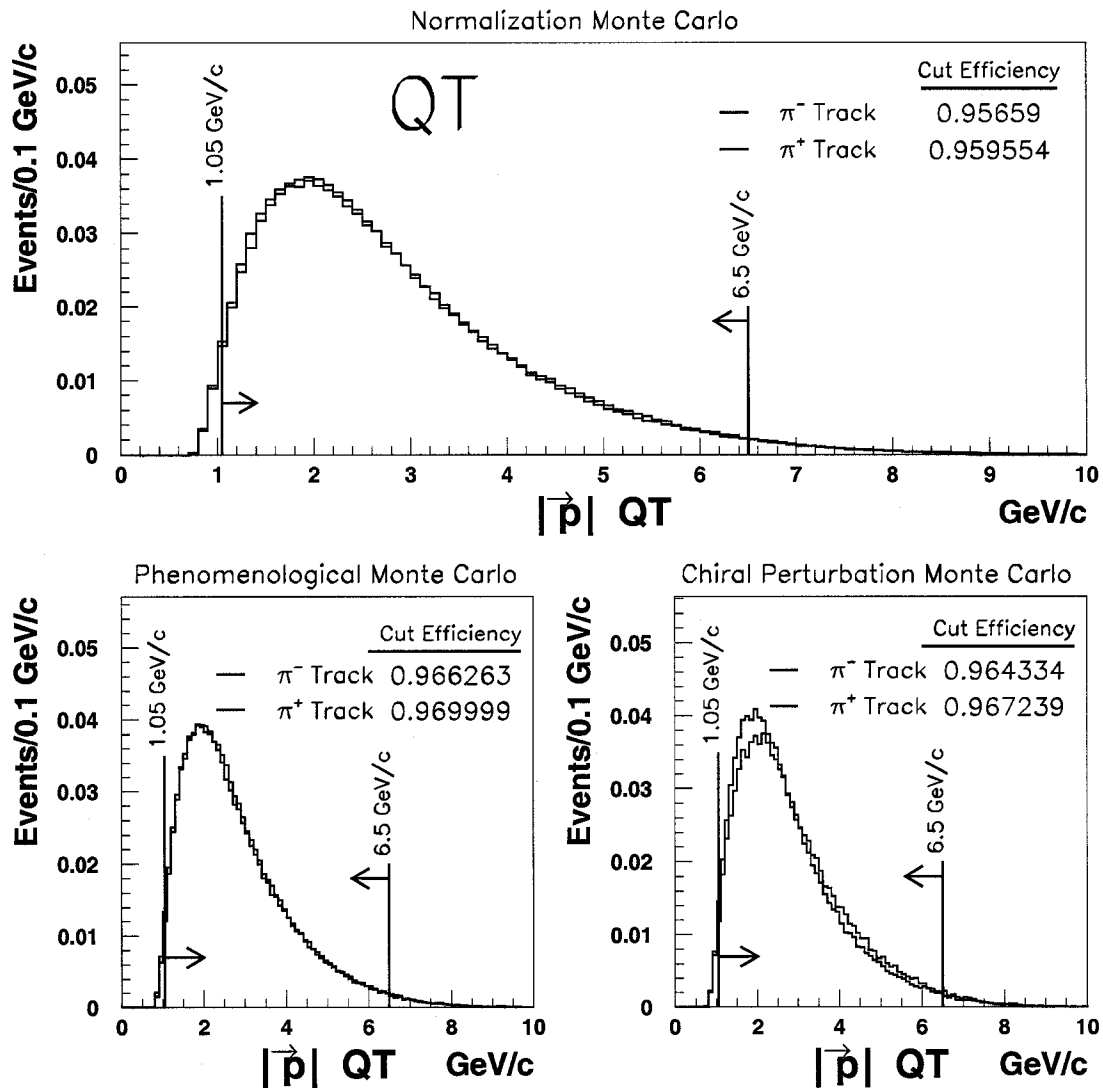


Figure 6.5: Pion momentum distributions for $K_L^0 \rightarrow \pi^+\pi^-$ and $K_L^0 \rightarrow \pi^+\pi^-e^+e^-$ with K_L^0 form factors calculated using the QT fit are presented. The efficiency of the $1.05 \text{ GeV}/c < |\vec{p}| < 6.5 \text{ GeV}/c$ cut is listed.

Vertex Position

Once the momentum and direction cosines of each track have been assigned by the fitting routines, the pion tracks are projected upstream into the vacuum decay region. The vertex position is defined as the midpoint of the line connecting the points at which the two tracks are at their distance of closest approach. The reconstructed vertex position must fall inside the decay tank as well as inside the neutral beam's x - y profile, which is defined by the collimators described in Sec. 3.2, for it to be accepted. In order to describe the position of vertex inside the decay tank with relation to the neutral beam profile, the vector that describes the vertex position, (x, y, z) will be replaced with angular positions (v_x, v_y, v_z) (see Figure 6.6 for a view of this change), where

$$v_x = \frac{x - T_x}{z - T_z}, \quad v_y = \frac{y - T_y}{z - T_z}, \quad \text{and} \quad v_z = z - T_z. \quad (6.1)$$

The vector \vec{T} in Eq. (6.1) is the point at which the K_L^0 was produced in the platinum target. As the beam diverges from the target into the decay tank, the angular limits on v_x and v_y stay constant while the limits on x and y depend on the z -position of the vertex.

The E871 fitting routines provide a method for extrapolating \vec{T} from the sum of the pion momentum vectors at the vertex point but this routine was specifically written for two-body decay. The momentum sum in the two-body case will equal the momentum of the decay K_L^0 due to conservation of momentum. The routine projects the K_L^0 track backward to the midpoint of the target, $z = 0$. This point is used for \vec{T} . For a four-body decay, the momentum sum of two of the pions will not necessarily equal that of the K_L^0 , even for events in which the primary tracks carry the bulk of the momentum. Even a small deviation in momentum will translate to a large difference in position at the target as the vector is projected 15 m upstream. For consistency between the two and four body decay channels, we will assume that

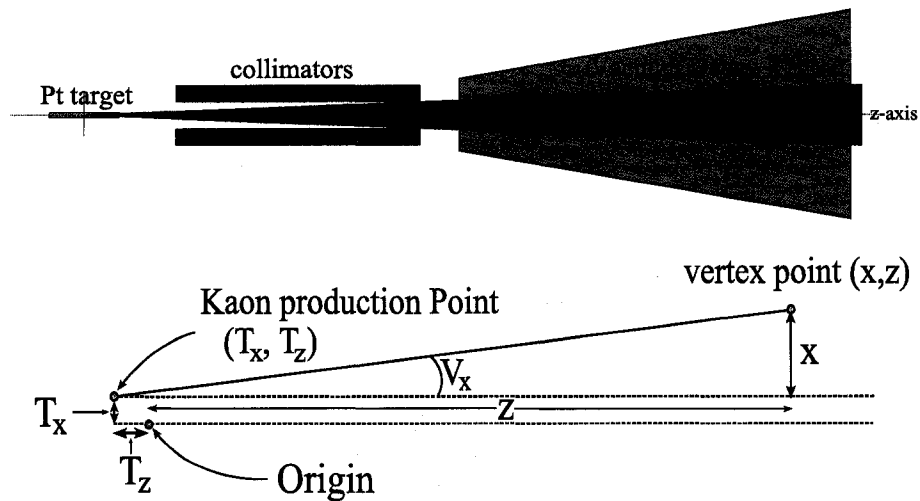


Figure 6.6: Top: The neutral beam profile from the platinum target is shown as defined by the brass collimators. Bottom: A pictorial description of how the vertex angles in Eq. (6.1) are calculated.

the neutral beam always originates from the center of the target, $\vec{T} = (0, 0, 0)$. The limits on the reconstructed K_L^0 vertex are defined by the upstream collimators as ± 0.0027 mrad for v_x and ± 0.01 mrad for v_y . These cuts remove background from poorly fit tracks due to pion decay, accidentals, and events with large scatters. Figure 6.7 and Figure 6.9 show the distributions for the vertex positions in x , y , and z and the distribution of the vertices in the v_x - v_y plane, respectively. In order to limit the acceptance of late-decaying K_S^0 into two pions, an upstream cut of 9.55 m is placed on the reconstructed z -position of the vertex. The likelihood of a K_S^0 surviving into the decay tank is small, but it will decay into a $\pi^+\pi^-$ pair 68.60% of the time [19]. At the downstream end of the decay tank, the z -position of the vertex is cut at 20.6 m since there is little fiducial acceptance for events decaying any further downstream.

As a compliment to the cuts made on vertex position, a limit can be placed on χ_{vtx}^2 values calculated to measure of how well the vertex point is fit from the reconstructed tracks. The methods used to calculate the χ_{vtx}^2 values can be found

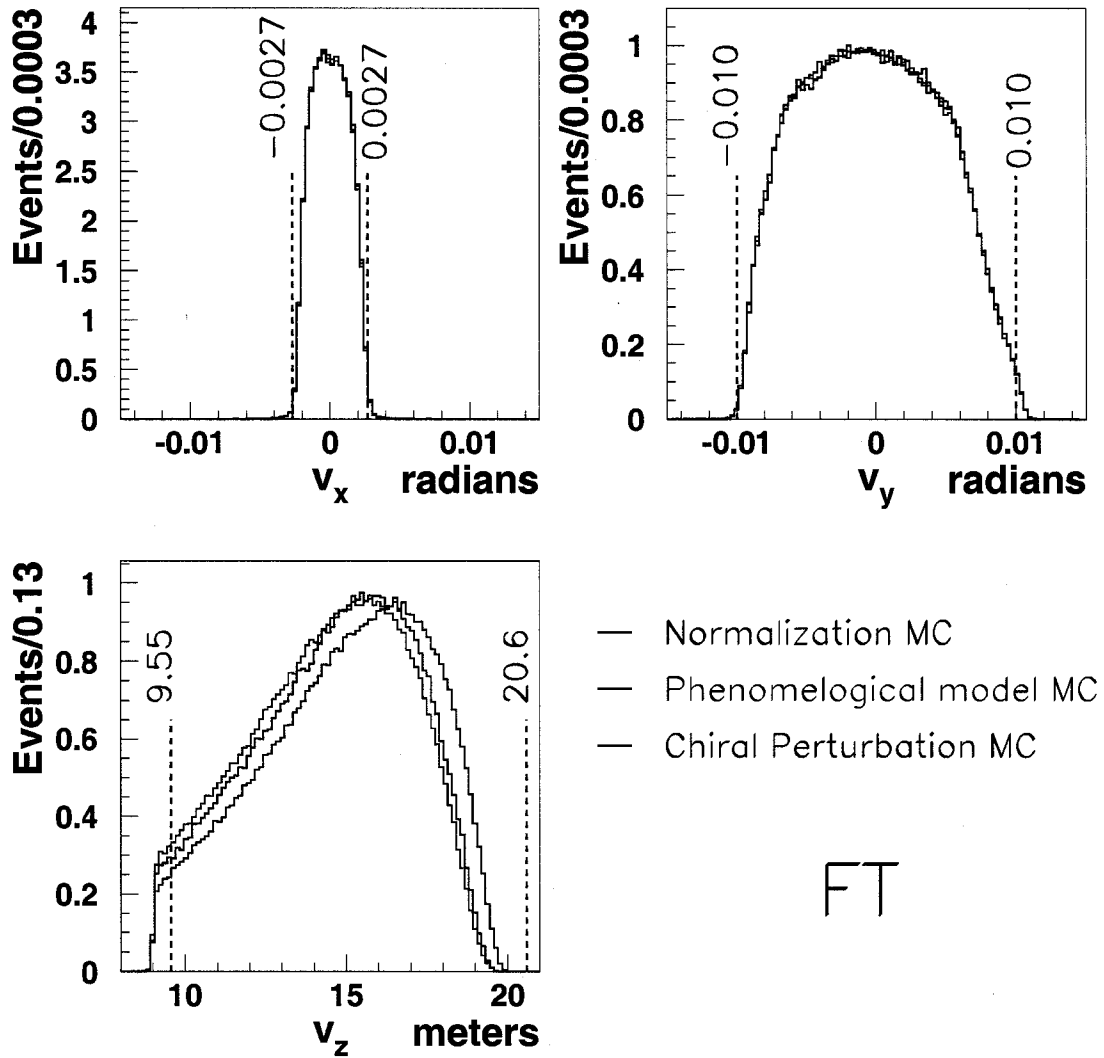


Figure 6.7: Angular vertex position distributions for v_x , v_y and v_z calculated using the FT fitter are shown for $K_L^0 \rightarrow \pi^+\pi^-$ and $K_L^0 \rightarrow \pi^+\pi^-e^+e^-$ with the cut values represented by the dashed lines.

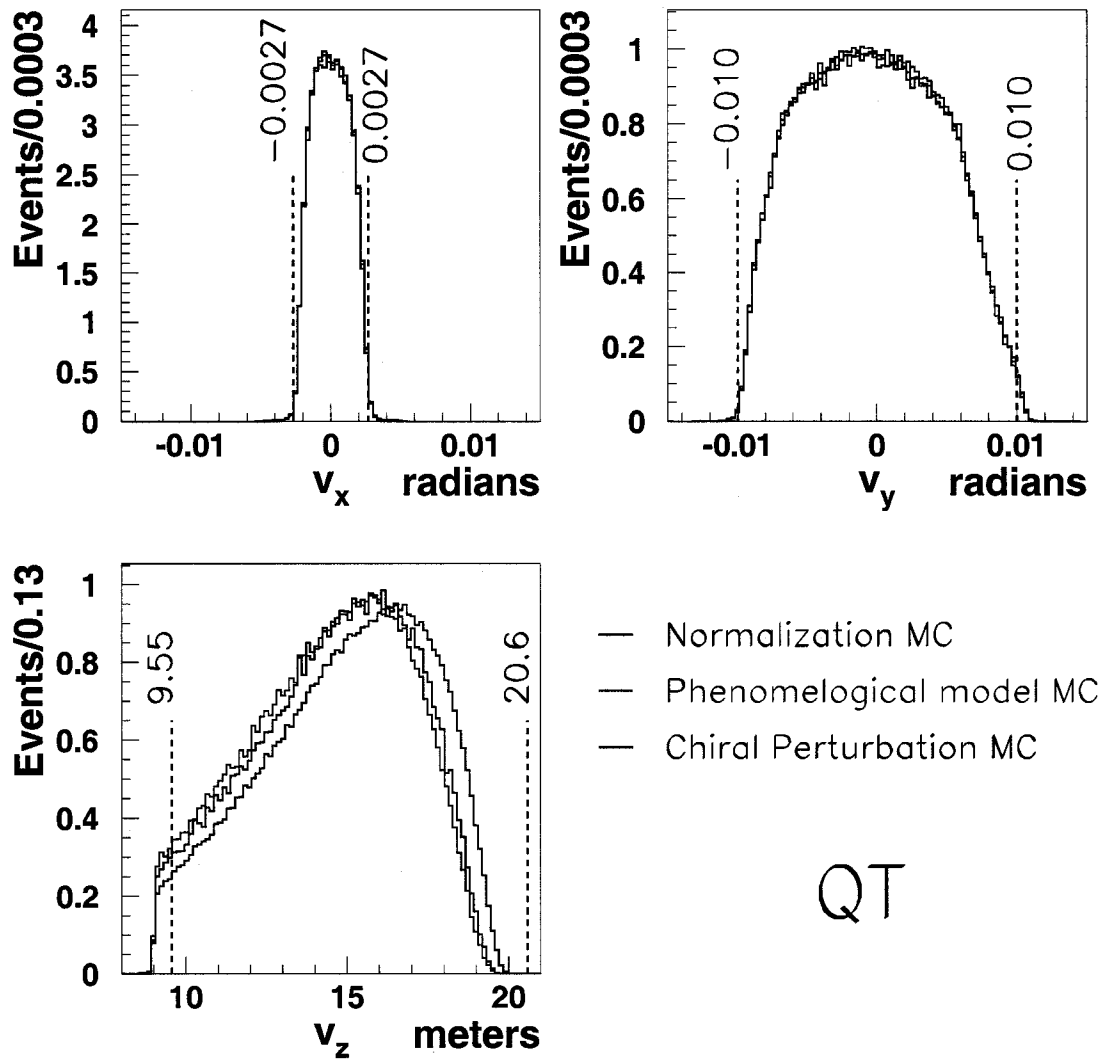


Figure 6.8: Angular vertex position distributions for v_x , v_y and v_z calculated using the QT fitter are shown for $K_L^0 \rightarrow \pi^+\pi^-$ and $K_L^0 \rightarrow \pi^+\pi^-e^+e^-$ with the cut values represented by the dashed lines.

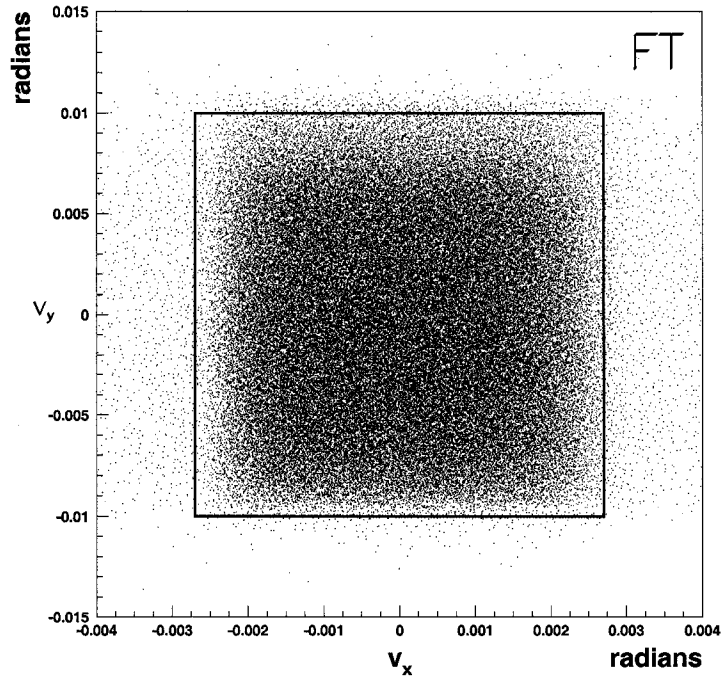


Figure 6.9: The distribution of the FT-reconstructed vertices in the v_x - v_y plane for the normalization Monte Carlo. This plot is typical of results for the QT-fitted events as well as for the two models of signal Monte Carlo. The blue box represents the $-0.0027 < v_x < 0.0027$ rad and $-0.01 < v_y < 0.01$ rad cuts on the angular vertex position.

from Eq. (5.4) and Eq. (5.8) for the FT and QT fitters, respectively. A cut of 30 for the FT fitter and 15 for the QT fitter eliminate poorly reconstructed events and have an efficiency of greater than 96% as shown in Figure 6.10 and Figure 6.11. Due to pion decay, the efficiency of these cuts is lower than those for purely leptonic events studied in E871, where the loss from this cut is less than 2%.

Particle Identification

Once two tracks in the spectrometer have been properly identified and reconstructed, their species must be determined to be able to classify the event. The particle identification detectors described in Chapter 3, Sec. 6.3 were built to positively identify electrons and muons over pions using the Cerenkov detector, lead-

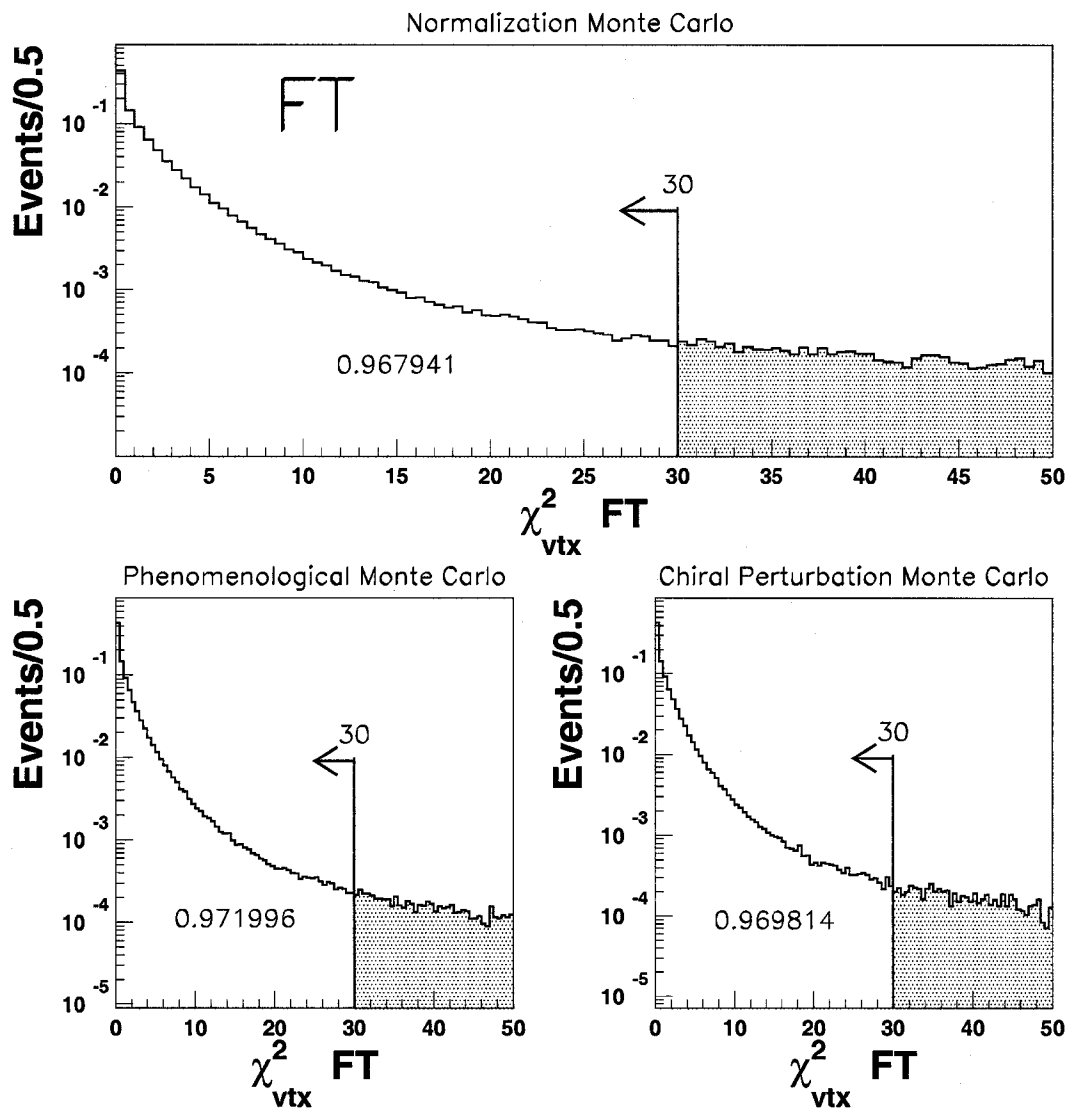


Figure 6.10: The χ^2_{vtx} distribution of the FT-reconstructed vertices for the pion tracks from Monte Carlo data is shown. The excluded region from the cut at 30 is shown in red and represents less than 4% of the sample.

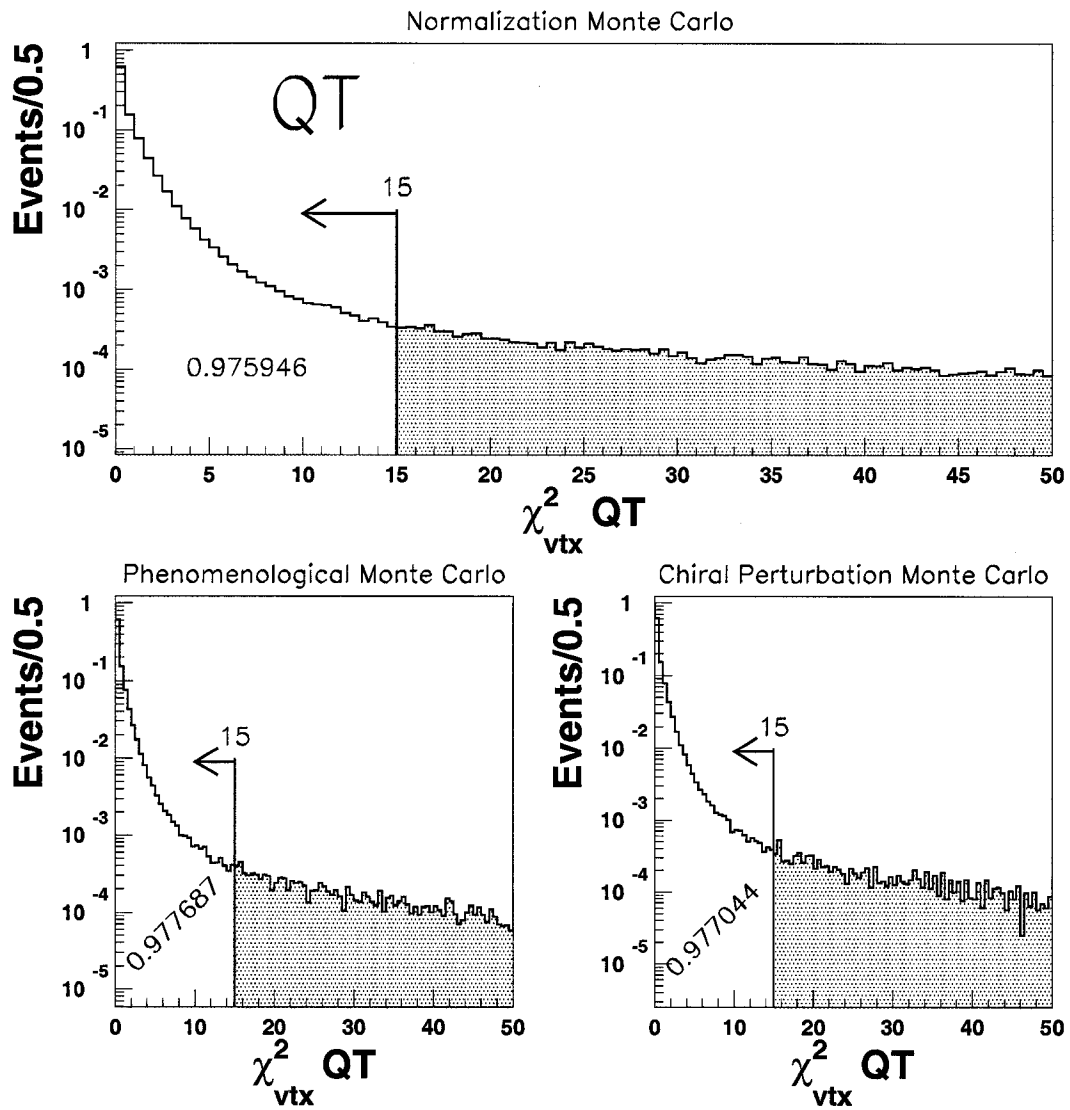


Figure 6.11: The χ^2_{vtx} distribution of the QT-reconstructed vertices for the pion tracks from Monte Carlo data is shown. The excluded region from the cut at 15 is shown in red and represents less than 4% of the sample.

| | possible | good |
|----------------------|--|--|
| Cerenkov (TKXIDK) | Simulated positions match actual corrected time is within ± 4 ns | Passes requirements for possible pass pulse height cut |
| Pb Glass (TKXIDG) | Passes $\frac{E}{p}$ cut passes $\frac{E_c}{E} / \frac{E}{p}$ contour cut | Passes requirements for possible passes energy centroid to hit position cut |
| Muon ID (TKXIDM) | Pass momentum matching (gap cut) hits in X0,Y0 or X1 MHO planes | Passes requirements for possible passes space and time cuts |

Table 6.1: Particle identification routine requirements for full tracks in the E871 detector.

glass calorimeter, muon hodoscope and muon rangefinder. Routines specific to each detector compare their hits to those expected if the given track were an electron for the Cerenkov and lead-glass portions, or a muon for the hodoscope and rangefinder. The routines will evaluate the hit information and compare it to what would be expected given the track properties found in the spectrometer. A hypothesis will be made based on the comparison and a value of “good” or “possible” will be assigned for each detector element (Table 6.1). In order to identify a track as a pion, the track must fail the “possible” cuts associated with being a muon or an electron. The efficiencies of the particle identification routines have been extensively studied in [39, 35, 40] and include the efficiency’s dependence on momentum and x -position and y -position for both beam left and beam right tracks. Due to the similarities in the momentum distributions shown in Figure 6.4 and Figure 6.5, the difference in these efficiencies between $K_L^0 \rightarrow \pi^+\pi^-e^+e^-$ signal decays and $K_L^0 \rightarrow \pi^+\pi^-$ normalization decays is very small, on the order of 10^{-4} .

FT Fitter

| Parameter | Cut Value | Normalization | Phenomen. | Chiral Pert. |
|--|------------------------------|---------------|-----------|--------------|
| | | Model | Model | Model |
| χ_T^2 , left track | 25 | 0.989 | 0.989 | 0.988 |
| χ_T^2 , right track | 25 | 0.988 | 0.989 | 0.989 |
| π^- track momentum | $1.05 \leq p \leq 6.5$ GeV/c | 0.951 | 0.965 | 0.966 |
| π^+ track momentum | $1.05 \leq p \leq 6.5$ GeV/c | 0.950 | 0.970 | 0.968 |
| vertex position, v_x | $ v_x < 2.7$ mrad | 0.991 | 0.990 | 0.990 |
| vertex position, v_y | $ v_y < 10$ mrad | 0.996 | 0.996 | 0.996 |
| vertex position, v_z | $9.55 < v_x < 20.6$ m | 0.980 | 0.974 | 0.977 |
| χ_{vtx}^2 | 30 | 0.968 | 0.972 | 0.970 |
| Efficiencies for events passing all cuts above | | 0.859 | 0.872 | 0.872 |

Table 6.2: Cut values and efficiencies associated with a good pion track in the spectrometer (FT fitter).

QT Fitter

| Parameter | Cut Value | Normalization | Phenomen. | Chiral Pert. |
|--|----------------------------|---------------|-----------|--------------|
| | | Model | Model | Model |
| χ_T^2 , tracks | 35 | 0.988 | 0.989 | 0.988 |
| π^- track momentum | $1.05 \leq p \leq 6.5$ GeV | 0.951 | 0.965 | 0.966 |
| π^+ track momentum | $1.05 \leq p \leq 6.5$ GeV | 0.950 | 0.970 | 0.968 |
| vertex position, v_x | $ v_x < 2.7$ mrad | 0.991 | 0.990 | 0.990 |
| vertex position, v_y | $ v_y < 10$ mrad | 0.996 | 0.996 | 0.996 |
| vertex position, v_z | $9.55 < v_x < 20.6$ m | 0.980 | 0.974 | 0.977 |
| χ_{vtx}^2 | 15 | 0.976 | 0.978 | 0.977 |
| Efficiencies for events passing all cuts above | | 0.856 | 0.868 | 0.866 |

Table 6.3: Cut values and efficiencies associated with a good pion track in the spectrometer (QT fitter).

6.4 Partial Tracking Stub Search

As described earlier, there is very little acceptance for four-body events in which either the positron or electron is able to traverse the entire spectrometer and pass all of the triggers. The low energy nature of the e^+e^- pair makes it unlikely that they will leave significant tracks in SDC3 or in elements further downstream. This fact limits the search for the e^+e^- tracks to the front of the spectrometer, or more specifically to SDC1 and SDC2. As such, the momentum of these tracks is not directly measurable and will have to be inferred from the transverse momentum of the primary track pair. A stub finding routine was written which employed both pattern recognition and the FT and QT fitters to perform an exhaustive search of all extra hits in the first two straw drift chambers. To limit the processing time, the stub finder was run only on events in which two pion tracks had been properly reconstructed (as described in the earlier section), thus limiting the search for $K_L^0 \rightarrow \pi^+\pi^-e^+e^-$ to the $K_L^0 \rightarrow \pi^+\pi^-$ data tapes.

The stub search begins in stage nine of the analysis code by re-running pattern recognition and the FT and QT fitters to find all cluster associated with extra hits in the first two left and right straw drift chambers. The hits associated with the primary pion tracks are masked out so they are not reused. For each extra cluster, segments are created using the same method as Sec. 5.2. SDC2. Stub candidates are formed by taking each x -segment in SDC1 and combining it with all possible combinations of segments from the y -plane of SDC1 and the x -plane and y -plane from SDC2. A simple example of the search for stub candidates is shown in Figure 6.12 for a situation involving only two planes of x -viewing straws. Events with excess noise can have well over 1000 possibilities, but events with less than 1024 are passed on for further analysis.

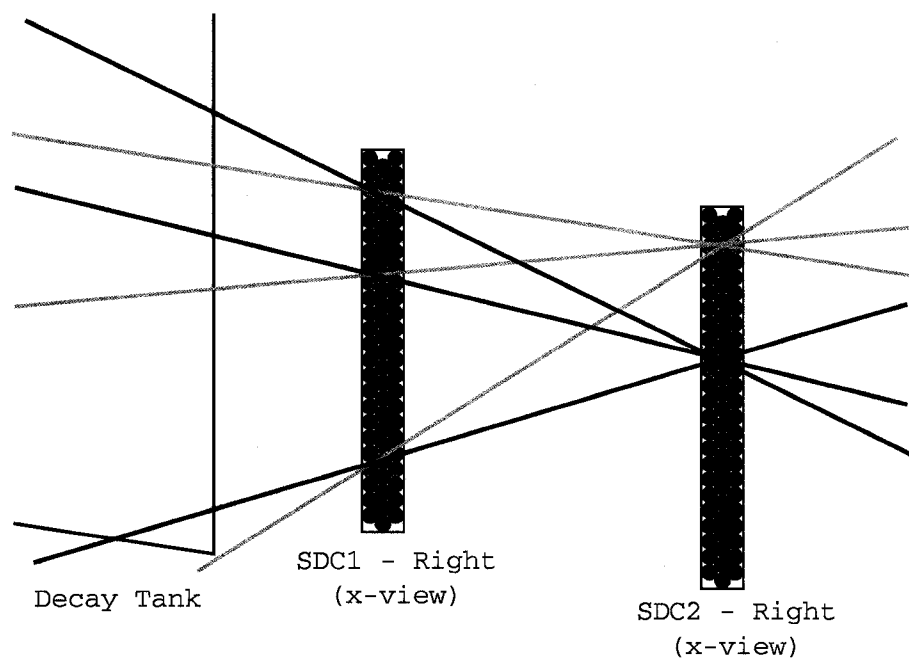


Figure 6.12: A simplified example of the search for stub candidates with three extra segments found in SDC1 and two extra segments in SDC2. A segment can only be used for one stub candidate. The selection is made based on a log-likelihood scoring system.

Partial Tracking Stub Momentum

The only information obtained by pattern recognition and the fitting routines in the stub search is the trajectory of each partial track from the hits left in the first two straw drift chambers. Since the momentum of the K_L^0 is unknown, conservation of momentum can not be used to calculate the momentum carried by the e^+e^- pair. However, by using the vertex position of pion pair and assuming the K_L^0 was produced in the center of the target, the sum of the momentum of the decay products that is transverse to the line connecting these points is invariant in the laboratory frame and should sum to zero. Figure 6.13 shows this graphically.

The transverse momentum of the pion and electron-positron pair can be calcu-

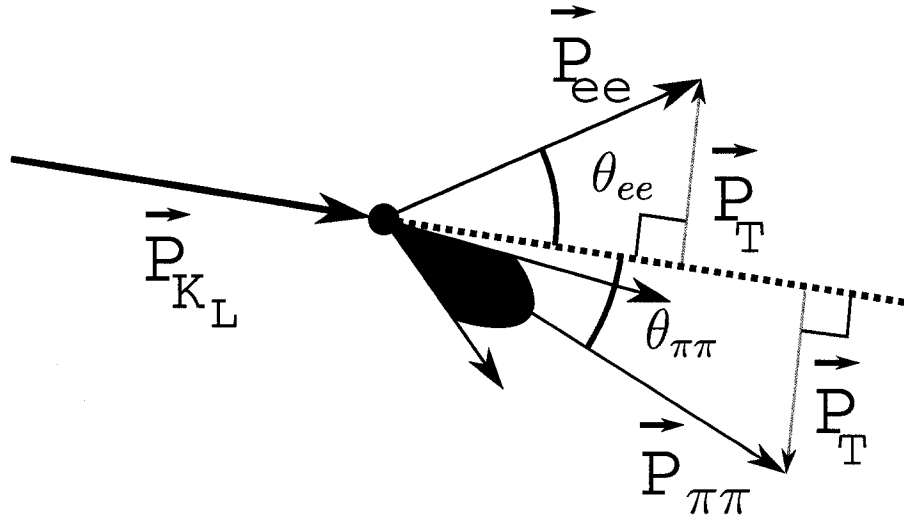


Figure 6.13: An illustration of the collinearity angles and vectors used to calculate the momentum of the e^+e^- momentum sum.

lated from

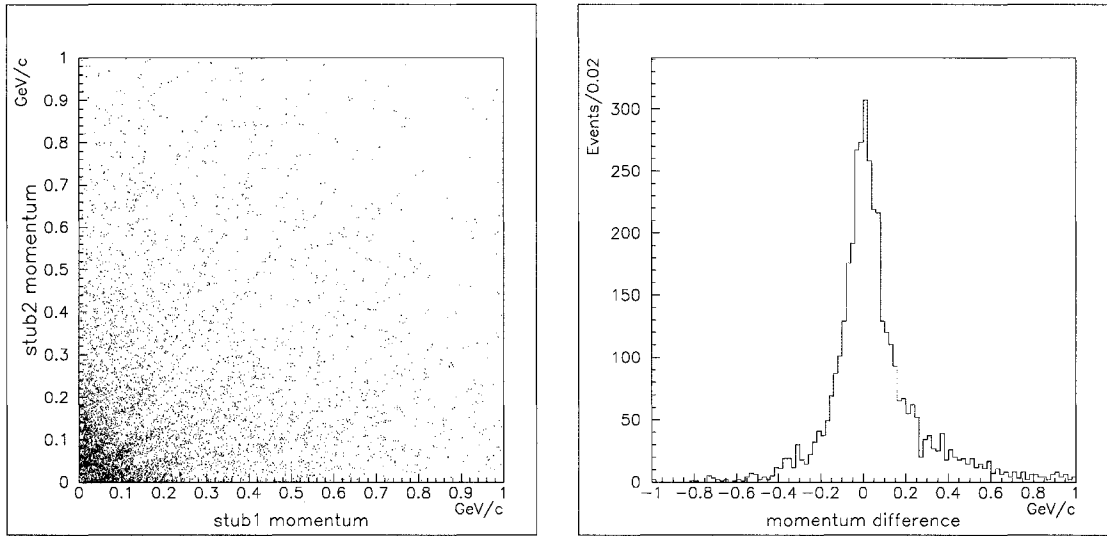
$$p_T^{\pi\pi} = |p_{\pi^+}^{\vec{}} + p_{\pi^-}^{\vec{}}| \sin(\theta_{\pi\pi}) \quad (6.2)$$

$$p_T^{ee} = |p_{e^+}^{\vec{}} + p_{e^-}^{\vec{}}| \sin(\theta_{ee}), \quad (6.3)$$

where collinearity angles $\theta_{\pi\pi}$ and θ_{ee} are the angle between the K_L^0 direction and the pion and electron-positron momentum sums, respectively. Since the momentum transverse to the K_L^0 direction must sum to zero, the magnitude of the e^+e^- pair's momentum can be inferred to be

$$|p_{e^+}^{\vec{}} + p_{e^-}^{\vec{}}| = |p_{\pi^+}^{\vec{}} + p_{\pi^-}^{\vec{}}| \frac{\sin(\theta_{\pi\pi})}{\sin(\theta_{ee})}. \quad (6.4)$$

To find the momentum of the individual stubs, we must assume that they have equal momentum in the laboratory frame. In the virtual photon's center of mass, the e^+ and e^- of each e^+e^- pair are emitted isotropically and with equal momentum. When the pair is Lorentz boosted into the laboratory frame, the maximum difference between the momentum of the e^+ and e^- can be approximately $2p_e^{cm}$ which is small compared to the boost. Figure 6.14 examines the difference between the e^+ and e^-



(a) Stub Momentum Asymmetry.

(b) MC-Reconstructed Momentum Difference.

Figure 6.14: The Monte Carlo distribution for the momentum carried by the electron and positron in the lab frame is shown in (a). The momentum difference, $|p_{e^+}^{\vec{}}| - |p_{e^-}^{\vec{}}|$, for all events in (a) is shown in (b).

momentum from Monte Carlo. Due to the soft nature of the virtual photon in both models, the phase space is dominated by events in which the momentum difference is small. The momentum of each stub from Eq. (6.4) is then

$$|p_{e^\pm}^{\vec{}}| = \frac{1}{2} |p_{\pi^+}^{\vec{}} + p_{\pi^-}^{\vec{}}| \frac{\sin(\theta_{\pi\pi})}{\sin(\theta_{ee})}. \quad (6.5)$$

Stub to Vertex DOCA

The reconstruction phase of the analysis begins with only the location of each stub candidate in the first two straw drift chambers known, along with the trajectory formed from these points. The most potent indicator of a correlation between the stub candidate and the pion tracks is the impact parameter of the partial track to pion vertex. A track to point minimization technique is used to calculate the distance of closest approach (DOCA). Given the point \vec{r} as a point on the stub's

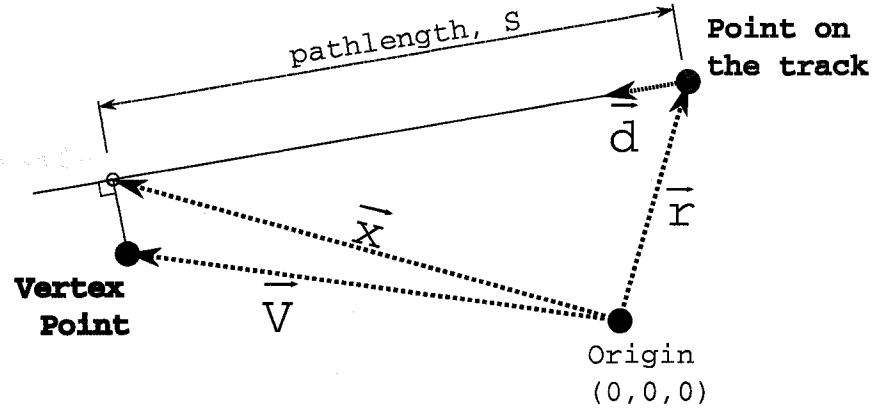


Figure 6.15: An illustration of the vectors used to calculate the DOCA value of a track to a point using the minimization technique.

track at SDC2, \hat{d} as the direction cosine of this track (assume \hat{d} points upstream into the decay tank), the point along the stub's path which is closest to the vertex point \vec{V} is

$$\vec{x} = \vec{r} - S\vec{d}, \quad (6.6)$$

where S is the pathlength from \vec{r} to the DOCA point \vec{x} . The DOCA is the distance between \vec{V} and \vec{x} , $|\vec{x} - \vec{V}|$. Figure 6.15 is an illustration. The minimization condition is then

$$\frac{\partial |\vec{x} - \vec{V}|}{\partial S} = 0 = \frac{\partial}{\partial S} \sqrt{[(\vec{x} - S\vec{d}) - \vec{V}]^2}. \quad (6.7)$$

We can find the solution to Eq. (6.7) by solving for S in

$$\frac{\partial}{\partial S} [(\vec{x} - S\vec{d}) - \vec{V}]^2 = 0 \quad (6.8)$$

which gives a pathlength at the DOCA of

$$S = \frac{\vec{d} \cdot (\vec{V} - \vec{x})}{d^2}. \quad (6.9)$$

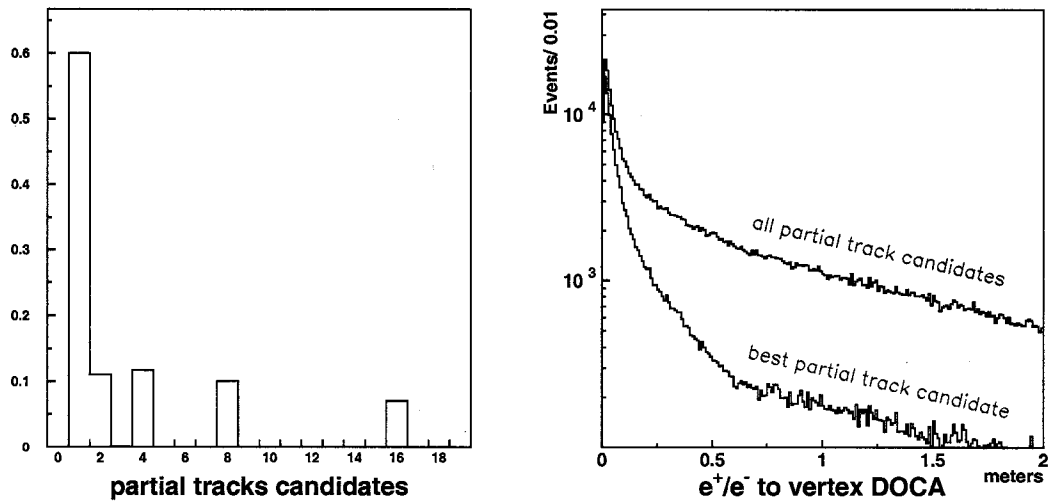
Once the pathlength is known, it can be combined with Eq. (6.6) to find the DOCA value, $|\vec{x} - \vec{V}|$ as

$$DOCA = \sqrt{\left| \left(\vec{r} - \left(\frac{\vec{d} \cdot (\vec{V} - \vec{x})}{d^2} \right) \vec{d} \right) - \vec{V} \right|^2}. \quad (6.10)$$

Monte Carlo generated samples were analyzed to study the number of stub candidates along with the DOCA values found for each. Figure 6.16 shows the number of stub candidates found per event for each model and the DOCA calculated for each. These samples include multiple scattering but do not include accidental hits in the straw drift chambers from background sources. Although the most numerous events are those with only one stub candidate, these must be removed as there is not enough information to reconstruct where the missing track should be without a momentum measurement on the stub. Reconstructing events with one stub is possible if the opening angle between the tracks is so small that they appear overlapped. In this case, it is assumed that one stub represents the trajectory of both, but the probability for this is small regardless of which model is used. The search will be limited to events where at least two candidate tracks are found.

The stub candidates are sorted according to the minimized DOCA. The two candidates with the smallest DOCAs are assumed to be the tracks for the electron and positron. Distinguishing the electron from the positron is impossible since the tracks do not make it into the magnetic field region of the spectrometer, but particle-track particle identification is also irrelevant to this analysis. Figure 6.17 and Figure 6.18 show the distribution of the DOCA values in each model for the best stub and the second best stub, respectively. Each distribution is fit to a log-normal function of the form

$$N \left(\frac{\text{events}}{\text{channel}} \right) = \frac{P_1}{P_3 \sqrt{2\pi}} \cdot e^{-\frac{1}{2} \left(\frac{\log(x) - \log(P_2)}{P_3} \right)^2}, \quad (6.11)$$

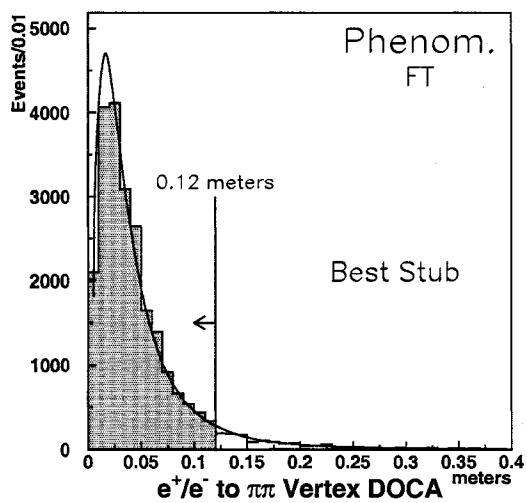


(a) partial track candidates per event.

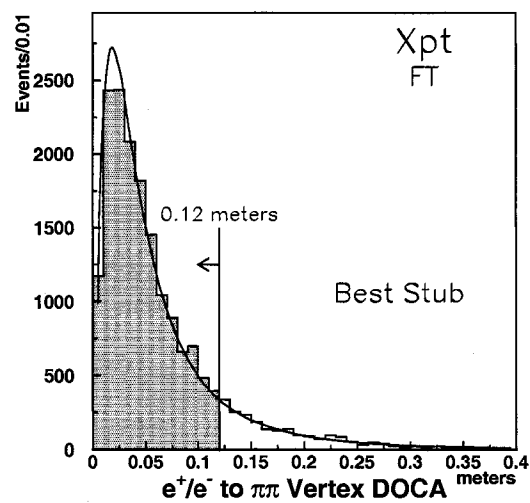
(b) e^+/e^- to vertex DOCA for all candidates (black) and for the best candidates (red).

Figure 6.16: Distributions for the number of partial track candidates per event and the e^+/e^- to vertex DOCA for each are shown for the phenomenological model using the FT fitter. Plots using the chiral perturbation model and the QT fitter show similar results.

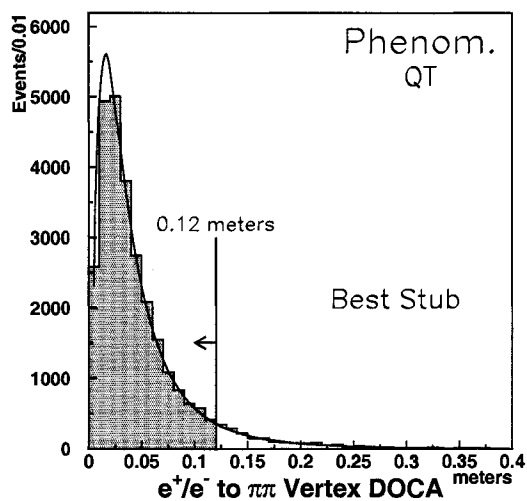
where x is the channel number, and P_1 through P_3 are the fit parameters. The stub to vertex DOCA is used as the primary figure of merit when deciding which events should be studied further and those events which will be discarded. A cut of 12 cm was chosen for the best stub candidate DOCA value so that the average efficiency of both models and fitters was approximately 90%. The cut associated with the second stub candidate was set at 18 cm and used to reduce the acceptance of events in which the track had a large scatter. Due to their low energy, multiple scattering in the downstream vacuum window and the straw drift chambers will increase one or both of the impact parameters of the partial tracks into a region where background events are more likely to occur. The efficiencies of these and all the following cuts are summarized in Table 6.4 at the end of this section.



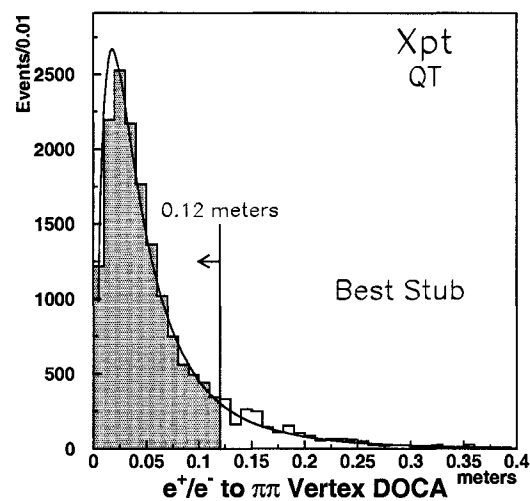
(a) Phenomenological Model, FT fitter.



(b) Chiral Perturbation Model, FT fitter.

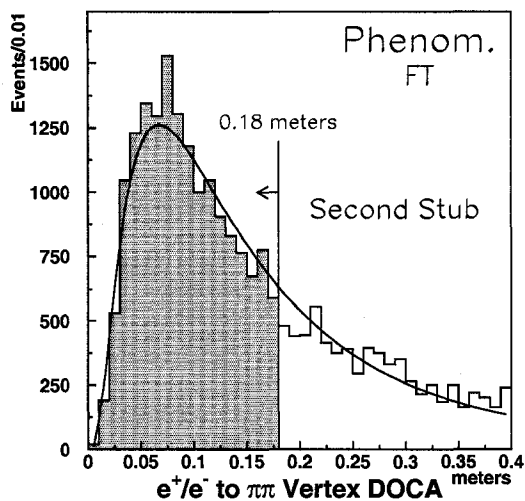


(c) Phenomenological Model, QT fitter.

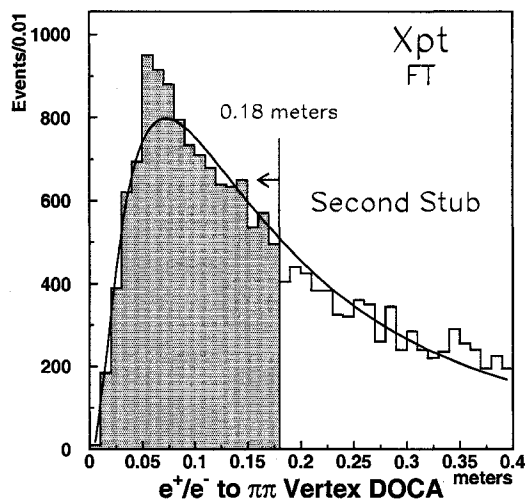


(d) Chiral Perturbation Model, QT fitter.

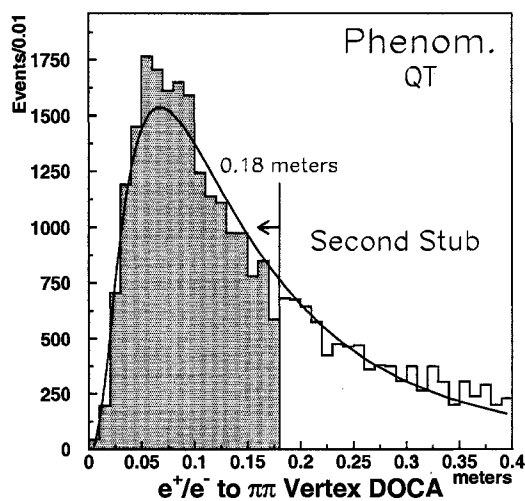
Figure 6.17: Stub to vertex DOCA of the stub candidate with the smallest stub to vertex DOCA for each event.



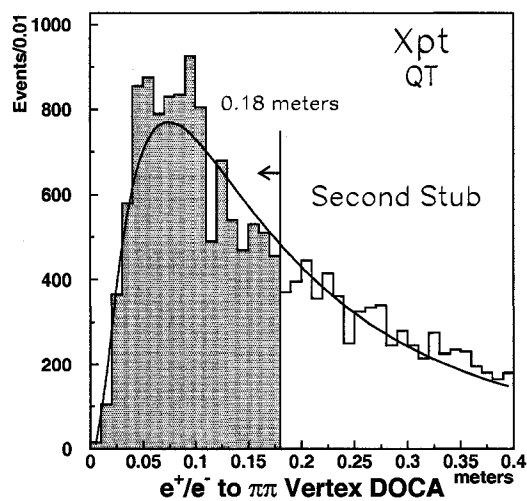
(a) Phenomenological Model, FT fitter.



(b) Chiral Perturbation Model, FT fitter.



(c) Phenomenological Model, QT fitter.



(d) Chiral Perturbation Model, QT fitter.

Figure 6.18: Stub to vertex DOCA of the stub candidate with the second smallest stub to vertex DOCA for each event.

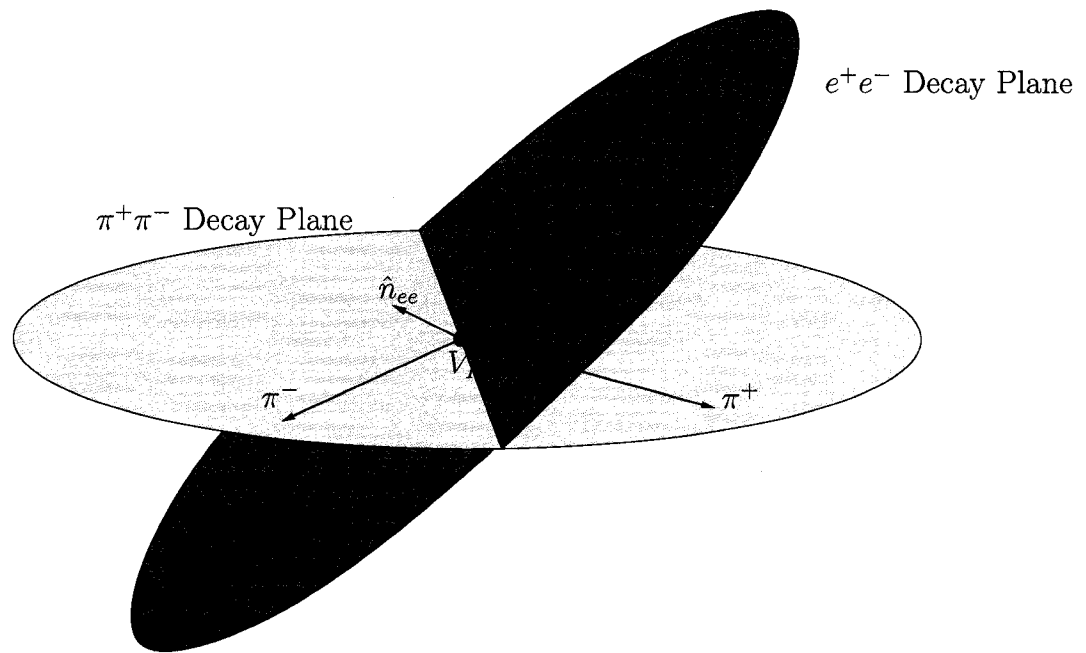


Figure 6.19: An illustration of the $\pi^+\pi^-$ and e^+e^- decay planes formed by the momentum vectors of the $\pi^+\pi^-$ and e^+e^- pairs, respectively.

Stub Correlation Angles

Due to the large momentum of the kaon in the laboratory frame, the daughters in the four body decay process will have their momentum highly boosted in the z -direction. This, along with the high invariant mass requirement for the $\pi^+\pi^-$ pair leads to a correlation between the stub momentum sum and pion decay plane as well as a correlation between the individual stub directions and the pion decay plane. As shown in Figure 6.19, the pion decay plane is described by the vector normal to the plane defined by the two pion momenta,

$$\hat{n}_{\pi\pi} = \frac{\vec{p}_{\pi^+} \times \vec{p}_{\pi^-}}{|\vec{p}_{\pi^+} \times \vec{p}_{\pi^-}|}. \quad (6.12)$$

If \vec{d} is the direction cosine of a single stub, the correlation angle between \vec{d} and

the primary decay plane ($\hat{n}_{\pi\pi}$) can be described as

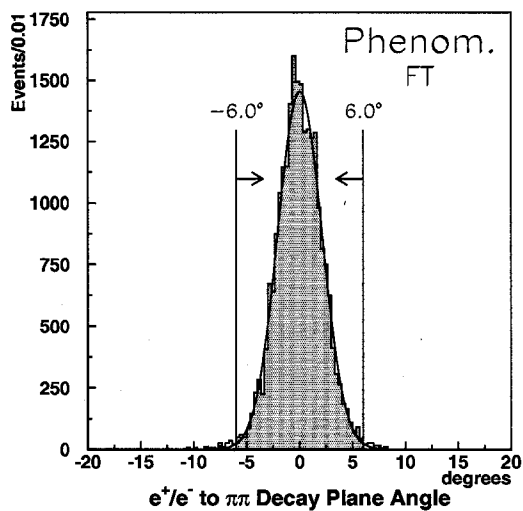
$$\alpha_{corr} = \vec{d} \cdot \hat{n}_{\pi\pi}. \quad (6.13)$$

The distribution of correlation angles for the individual stubs can be found in Figure 6.20 and Figure 6.21. The histograms were fit to Gaussian functions and values of $\pm 6^\circ$ and $\pm 6.7^\circ$ were found to agree with $\sim 3\sigma$ cut for both models and both fitters with only the two-body cuts applied.

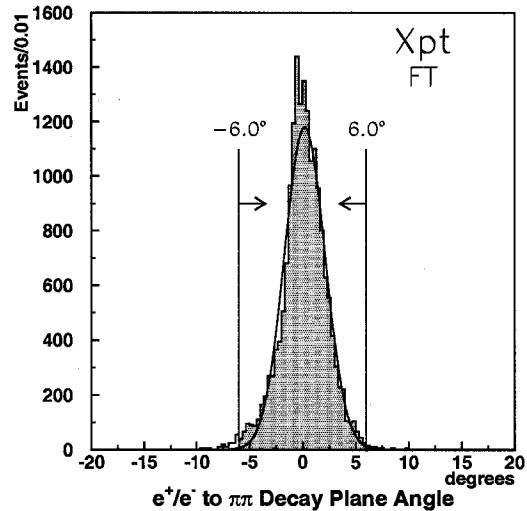
Stub to Stub Opening Angle

For much the same reasons that a correlation exists between the stub and pion momentum sums, the angle between the stub pairs also displays an interconnection. The three body nature of the intermediate $K_L^0 \rightarrow \pi^+\pi^-\gamma^*$ state and the need for the pions to carry at least 460 MeV of the invariant mass leads to the virtual gamma having only a small fraction of the available energy in the kaon center of mass for events accepted into the detector. The virtual photon undergoes a Dalitz decay and the products are Lorentz boosted into the laboratory frame. Since the virtual photon's energy is small compared to the energy associated with the boost, the Dalitz pair formed in its decay will be thrown forward with a very small angle between them. The distribution of stub opening angles for both models can be found in Figure 6.22.

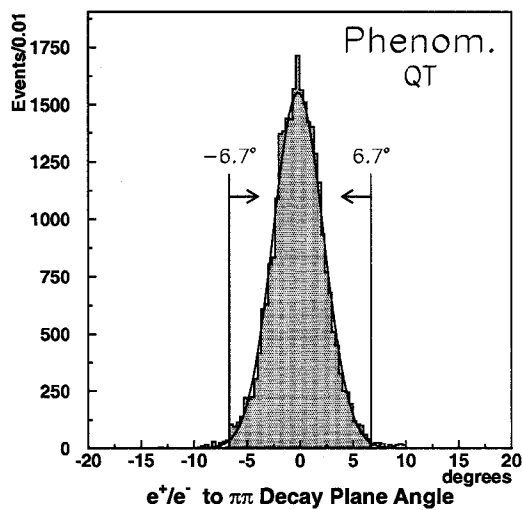
By limiting the maximum opening angle to 8° , we can take advantage of the correlation between the stubs to remove background. The opening angle between partial tracking stubs from K_{e3} and $K_{\mu 3}$ pileup events will not have any such correlation as the lepton tracks are wholly uncorrelated. Partial tracks from K_S^0 , neutron, and Λ decay products at the end of the neutral beamline or in the decay tank which are in time with a $K_L^0 \rightarrow \pi^+\pi^-$ events will be limited by such a cut as well (Chapter 7). The opening angle distributions for the e^+e^- pairs in the four-body



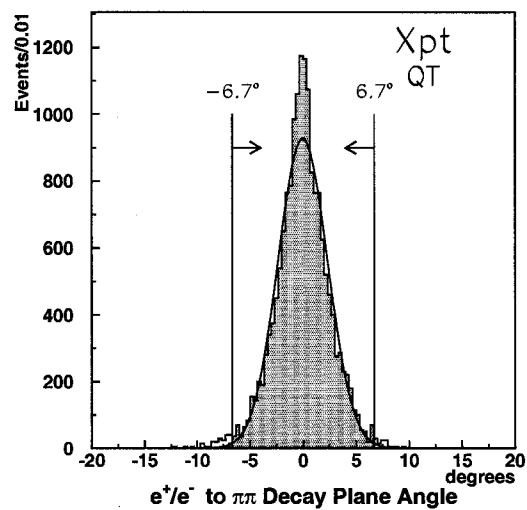
(a) Phenomenological Model, best stub, FT fitter.



(b) Chiral Perturbation Model, best stub, FT fitter.

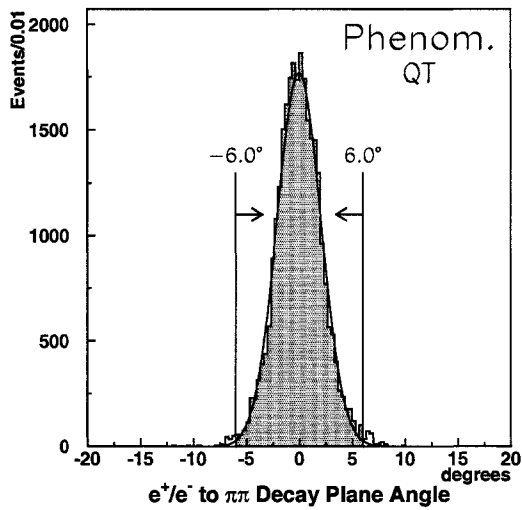


(c) Phenomenological Model, 2nd best stub, FT fitter.

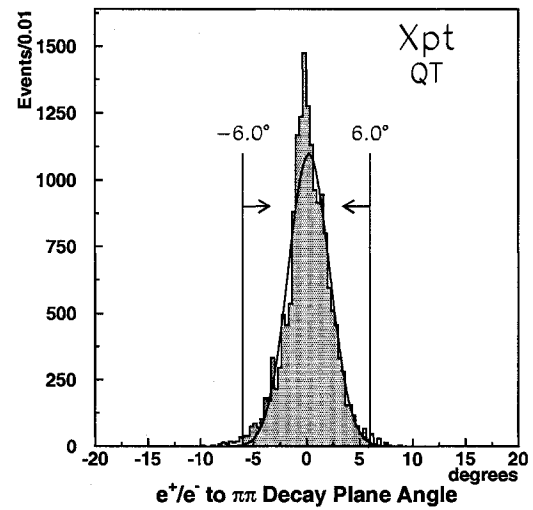


(d) Chiral Perturbation Model, 2nd best stub, FT fitter.

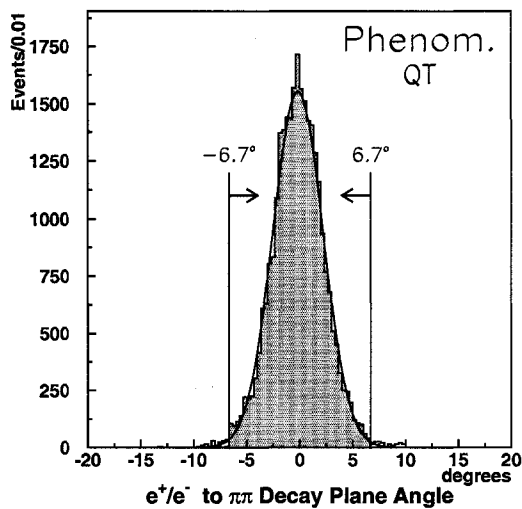
Figure 6.20: The stub to primary decay plane angle for the best two stub candidates using the FT fitter.



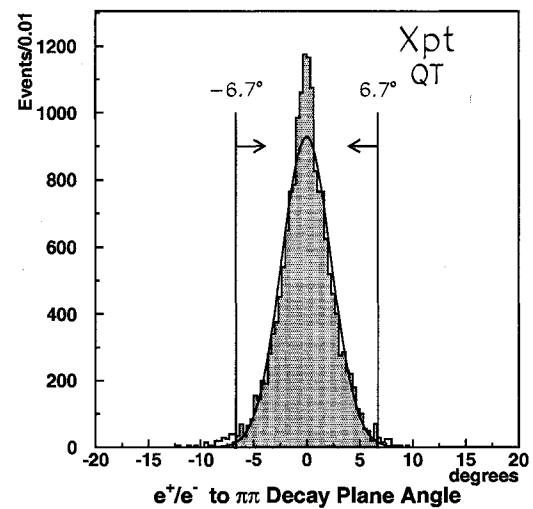
(a) Phenomenological Model, best stub, QT fitter.



(b) Chiral Perturbation Model, best stub, QT fitter.

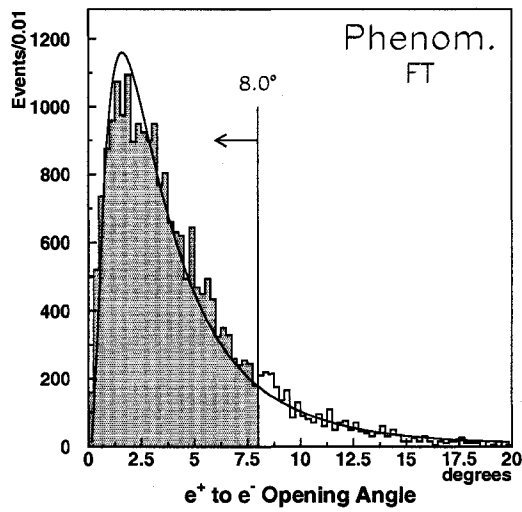


(c) Phenomenological Model, 2nd best stub, QT fitter.

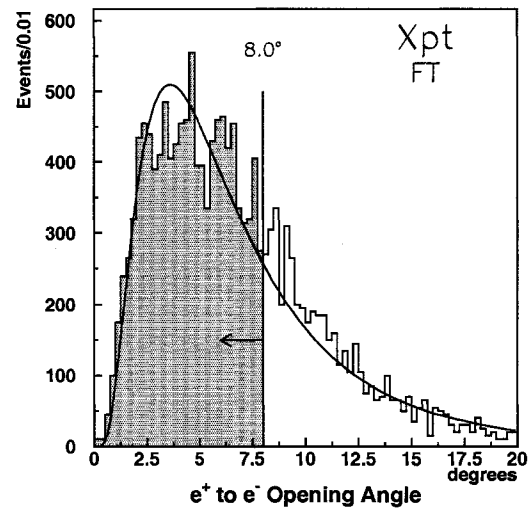


(d) Chiral Perturbation Model, 2nd best stub, QT fitter.

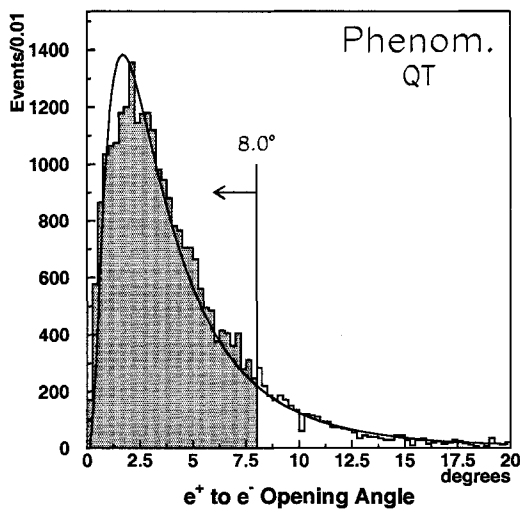
Figure 6.21: The stub to primary decay plane angle for the best two stub candidates using the QT fitter.



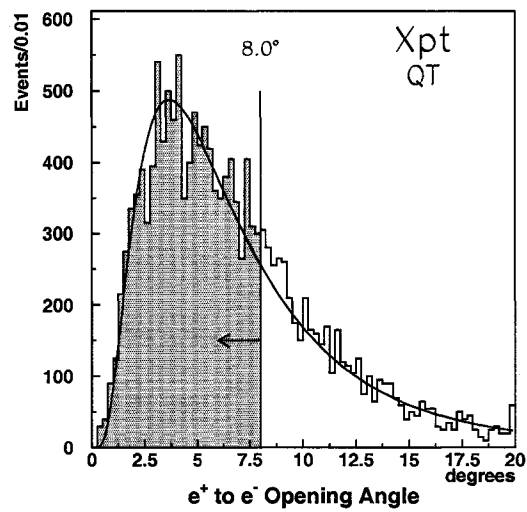
(a) Phenomenological Model, FT fitter.



(b) Chiral Perturbation Model, FT fitter.



(c) Phenomenological Model, QT fitter.



(d) Chiral Perturbation Model, QT fitter.

Figure 6.22: Stub to stub opening angle between the best two stub candidate for each event.

decays were fit to a log-normal distribution (Eq. (6.11)). The efficiencies of this cut varies widely across the two models (Table 6.4) but is necessary due to background considerations.

Stub to Stub DOCA

To determine further correlation between the best and second best partial tracks, their DOCA value is calculated using a track to track method similar to the track to point method described in Sec. 6.4. From the stub candidate search, the direction cosine (\vec{d}_i) and a reference point along the path (\vec{r}_i) are known for each track. If the point along each track where the DOCA occurs is \vec{x}_i where $i = 1, 2$, then

$$\vec{x}_i = \vec{r}_i - \vec{d}_i \cdot S_i. \quad (6.14)$$

S_i is the pathlength from the reference point to the DOCA point, and is found by minimizing the distance between \vec{x}_1 and \vec{x}_2 to be

$$S_1 = \frac{(\vec{d}_1 \cdot \vec{d}_2)(\vec{d}_2 \cdot (\vec{r}_1 - \vec{r}_2)) - (\vec{d}_1 \cdot (\vec{r}_1 - \vec{r}_2))}{1 - (\vec{d}_1 \cdot \vec{d}_2)^2} \quad (6.15)$$

$$S_2 = \frac{(\vec{d}_2 \cdot (\vec{r}_1 - \vec{r}_2)) - (\vec{d}_1 \cdot \vec{d}_2)(\vec{d}_1 \cdot (\vec{r}_1 - \vec{r}_2))}{1 - (\vec{d}_1 \cdot \vec{d}_2)^2}. \quad (6.16)$$

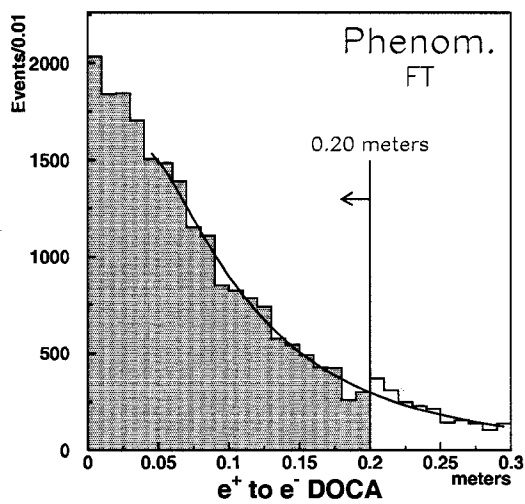
Substituting this into Eq. (6.14), the DOCA point for each track is found to be

$$\vec{x}_1 = \vec{r}_1 - \vec{d}_1 \left[\frac{(\vec{d}_1 \cdot \vec{d}_2)(\vec{d}_2 \cdot (\vec{r}_1 - \vec{r}_2)) - (\vec{d}_1 \cdot (\vec{r}_1 - \vec{r}_2))}{1 - (\vec{d}_1 \cdot \vec{d}_2)^2} \right] \quad (6.17)$$

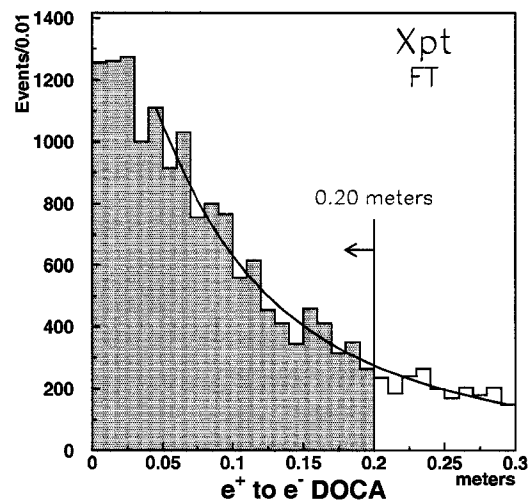
$$\vec{x}_2 = \vec{r}_2 - \vec{d}_2 \left[\frac{(\vec{d}_2 \cdot (\vec{r}_1 - \vec{r}_2)) - (\vec{d}_1 \cdot \vec{d}_2)(\vec{d}_1 \cdot (\vec{r}_1 - \vec{r}_2))}{1 - (\vec{d}_1 \cdot \vec{d}_2)^2} \right], \quad (6.18)$$

and the DOCA between the stub pair is then $\vec{x}_1 - \vec{x}_2$.

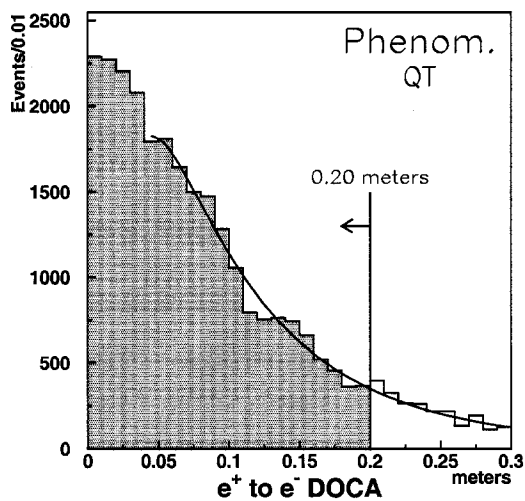
In an ideal situation, one would expect that all tracks originating from a $K_L^0 \rightarrow \pi^+\pi^-\pi^+\pi^-$ event to have a DOCA value of zero, but resolution effects and multiple



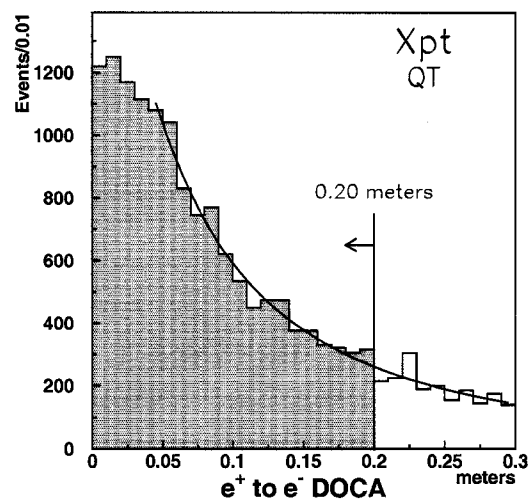
(a) Phenomenological Model, FT fitter.



(b) Chiral Perturbation Model, FT fitter.



(c) Phenomenological Model, QT fitter.



(d) Chiral Perturbation Model, QT fitter.

Figure 6.23: Stub to stub DOCA between the best two stub candidate for each event.

| FT fitter: | | | |
|--|------------|--------------------------|----------------------------|
| Quantity of Interest | Cut Values | Phenom. Model efficiency | χ pt Model efficiency |
| stub-vertex DOCA, best stub | 0.12 m | 0.944 | 0.879 |
| stub-vertex DOCA, 2 nd stub | 0.18 m | 0.699 | 0.626 |
| stub- $\pi^+\pi^-$ decay plane \angle (best) | 6° | 0.989 | 0.988 |
| stub- $\pi^+\pi^-$ decay plane \angle (2 nd) | 6.7° | 0.986 | 0.986 |
| stub opening angle | 8° | 0.846 | 0.626 |
| stub to stub DOCA | 0.20 m | 0.873 | 0.810 |
| QT fitter: | | | |
| Quantity of Interest | Cut Values | Phenom. Model efficiency | χ pt Model efficiency |
| stub-vertex DOCA, best stub | 0.12 m | 0.932 | 0.878 |
| stub-vertex DOCA, 2 nd stub | 0.18 m | 0.694 | 0.630 |
| stub- $\pi^+\pi^-$ decay plane \angle (best) | 6° | 0.986 | 0.986 |
| stub- $\pi^+\pi^-$ decay plane \angle (2 nd) | 6.7° | 0.988 | 0.981 |
| stub opening angle | 8° | 0.848 | 0.631 |
| stub to stub DOCA | 0.20 m | 0.881 | 0.816 |

Table 6.4: Cut values and efficiencies for the four-body reconstruction in each fitter and model.

scattering smear the distribution to values as large as 70 cm. The stub to stub DOCA distributions are shown in Figure 6.23. A cut value of 20 cm keeps the efficiency above 80% for all models.

6.5 Acceptances

The acceptance for a given decay channel is defined as the number of events which are geometrically admitted to the spectrometer, trigger scintillating counters, and the particle identification systems consecutively and pass all imposed reconstruction requirements. Geometrically for both the $K_L^0 \rightarrow \pi^+\pi^-$ normalization and $K_L^0 \rightarrow \pi^+\pi^-e^+e^-$ signal, the two pions must have an opening angle which allows

them to enter the spectrometer and create hits in all detector elements. This requires that they have the correct charge and meet the transverse momentum criteria. An extra geometric provision is imposed for the four-body signal in that the e^+ and e^- tracks must hit the first two straw drift chambers.

The detector and reconstruction efficiencies are folded in with the geometric acceptance in the E871 Monte Carlo. The effect of dead or missing wires and the finite resolution of the drift chambers is included, as well as effects from the inefficiency of the trigger system, kinematic cuts from data reduction and pion decay. The branching ratio calculation for $K_L^0 \rightarrow \pi^+\pi^-e^+e^-$ depends on the acceptance ratio between the normalization and signal in order to compensate for the increase in the number of $K_L^0 \rightarrow \pi^+\pi^-e^+e^-$ events lost compared to $K_L^0 \rightarrow \pi^+\pi^-$. For the $K_L^0 \rightarrow \pi^+\pi^-e^+e^-$ signal, the acceptance

$$A_{\pi\pi ee} = A_{\pi\pi ee}^{Geometric} \cdot \epsilon_{\pi\pi} \cdot \epsilon_{stubs} \quad (6.19)$$

can be measured from the ratio of simulated events that pass all requirements in Table 6.2, Table 6.3, and Table 6.4 to the total number of events generated. The stub-detection efficiency is included in this ratio by inclusion of the four-body cuts. Figure 6.24 shows the distribution of the selected events in invariant mass and transverse momentum. The signal region for $K_L^0 \rightarrow \pi^+\pi^-e^+e^-$ events is centered on the mass of the K_L^0 and is defined as $0.4905 < M_{\pi\pi ee} < 0.505$ GeV for the FT fitter and $0.490 < M_{\pi\pi ee} < 0.5055$ GeV for the QT fitter. All events accepted events must also have $p_T^{4body} < 0.01$ GeV/c to ensure momentum conservation. In order to keep the signal and normalization samples mutually exclusive, an additional requirement is placed on the four-body reconstruction. If the event satisfies the two-body selection criteria and falls in the normalization's signal region, it is cut from the $K_L^0 \rightarrow \pi^+\pi^-e^+e^-$ candidate sample. Figure 6.25 shows the projection of plots in Figure 6.24 onto the mass axis.

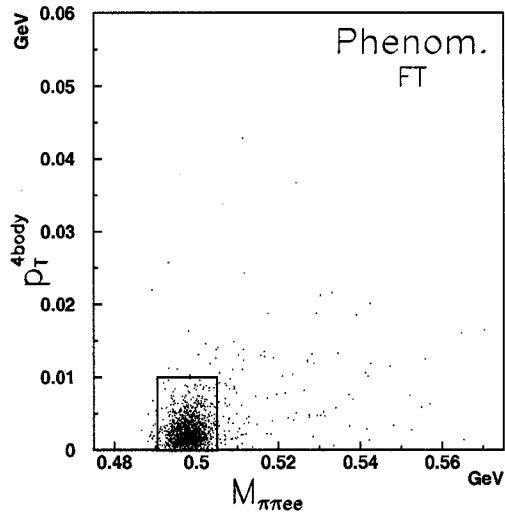
For the $K_L^0 \rightarrow \pi^+\pi^-$ normalization, the acceptance

$$A_{\pi\pi} = A_{\pi\pi}^{geometric} \cdot \epsilon_{\pi\pi} \quad (6.20)$$

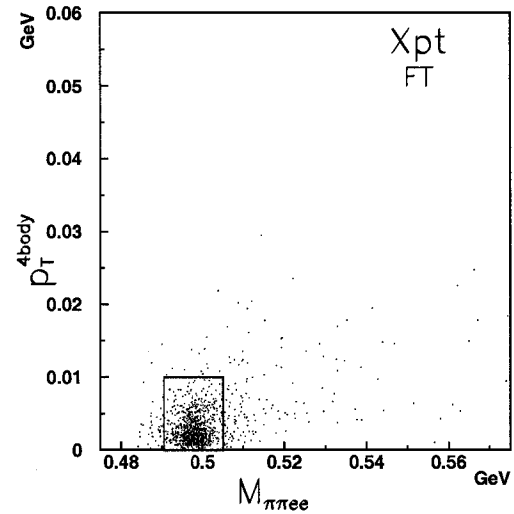
is calculated in the same manner as the signal acceptance. Figure 6.26 and Figure 6.27 show the distribution of all events passing the two-body selection criteria in invariant mass and transverse momentum squared. The signal region for normalization events is defined as events having two-body p_T^2 less than 0.0001 (GeV/c)^2 and $0.4935 < M_{\pi\pi} < 0.502 \text{ GeV}$ for the FT fitter and $0.493 < M_{\pi\pi} < 0.5025 \text{ GeV}$ for the QT fitter. The acceptance ratio between the normalization and signal is found from

$$\frac{A_{\pi\pi}}{A_{\pi\pi ee}} = \frac{N_{\pi\pi}^{passed}}{N_{\pi\pi ee}^{passed}} \cdot \frac{N_{\pi\pi}^{generated}}{N_{\pi\pi ee}^{generated}}, \quad (6.21)$$

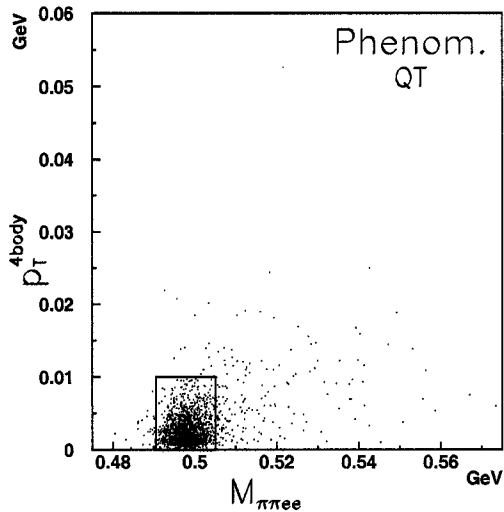
where N_i^{passed} is the number of Monte Carlo events passing all selection requirements and falling in the signal region for a decay mode and $N_i^{generated}$ is the total number of Monte Carlo events simulated. The results for the acceptance ratio using each fitter and model is shown in Table 6.5.



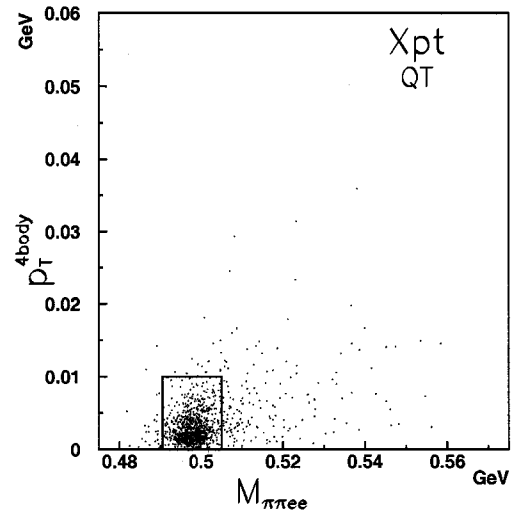
(a) Phenomenological Model, FT fitter.



(b) Chiral Perturbation Model, FT fitter.

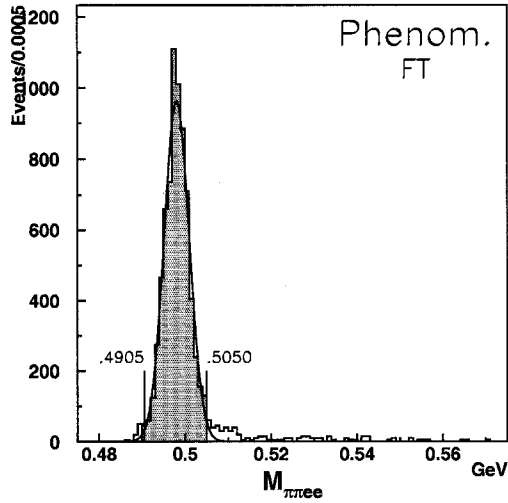


(c) Phenomenological Model, QT fitter.

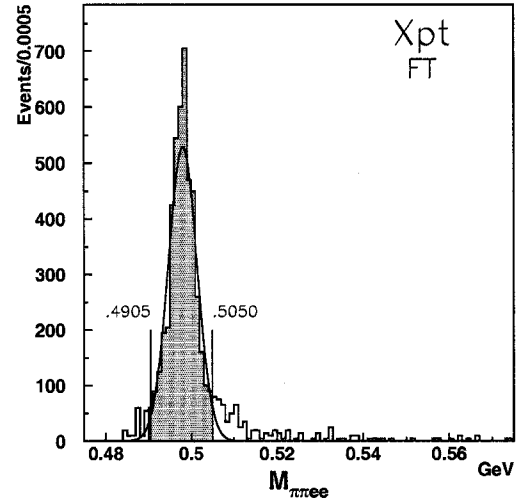


(d) Chiral Perturbation Model, QT fitter.

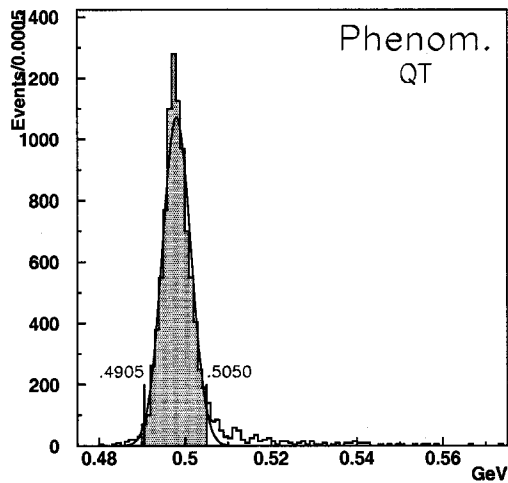
Figure 6.24: Invariant mass versus transverse momentum distributions for Monte Carlo events which pass all two and four body cuts are shown. The box represents the signal region of $0.4905 < M_{\pi\pi ee} < 0.505$ GeV and $p_T^{4body} < 0.01$ GeV/c for the FT fitter and $0.490 < M_{\pi\pi ee} < 0.5055$ GeV and $p_T^{4body} < 0.01$ GeV/c for the QT fitter.



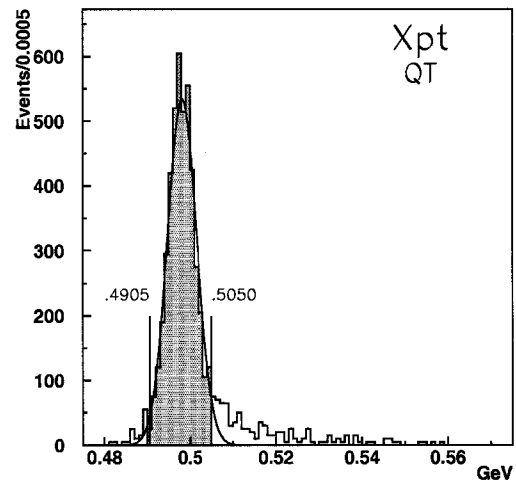
(a) Phenomenological Model, FT fitter.



(b) Chiral Perturbation Model, FT fitter.



(c) Phenomenological Model, QT fitter.



(d) Chiral Perturbation Model, QT fitter.

Figure 6.25: Invariant mass distributions for Monte Carlo events which pass all two and four body cuts are shown. The red lines represents the signal region of $0.4905 < M_{\pi\pi ee} < 0.505$ GeV for the FT fitter and $0.490 < M_{\pi\pi ee} < 0.5055$ GeV for the QT fitter.

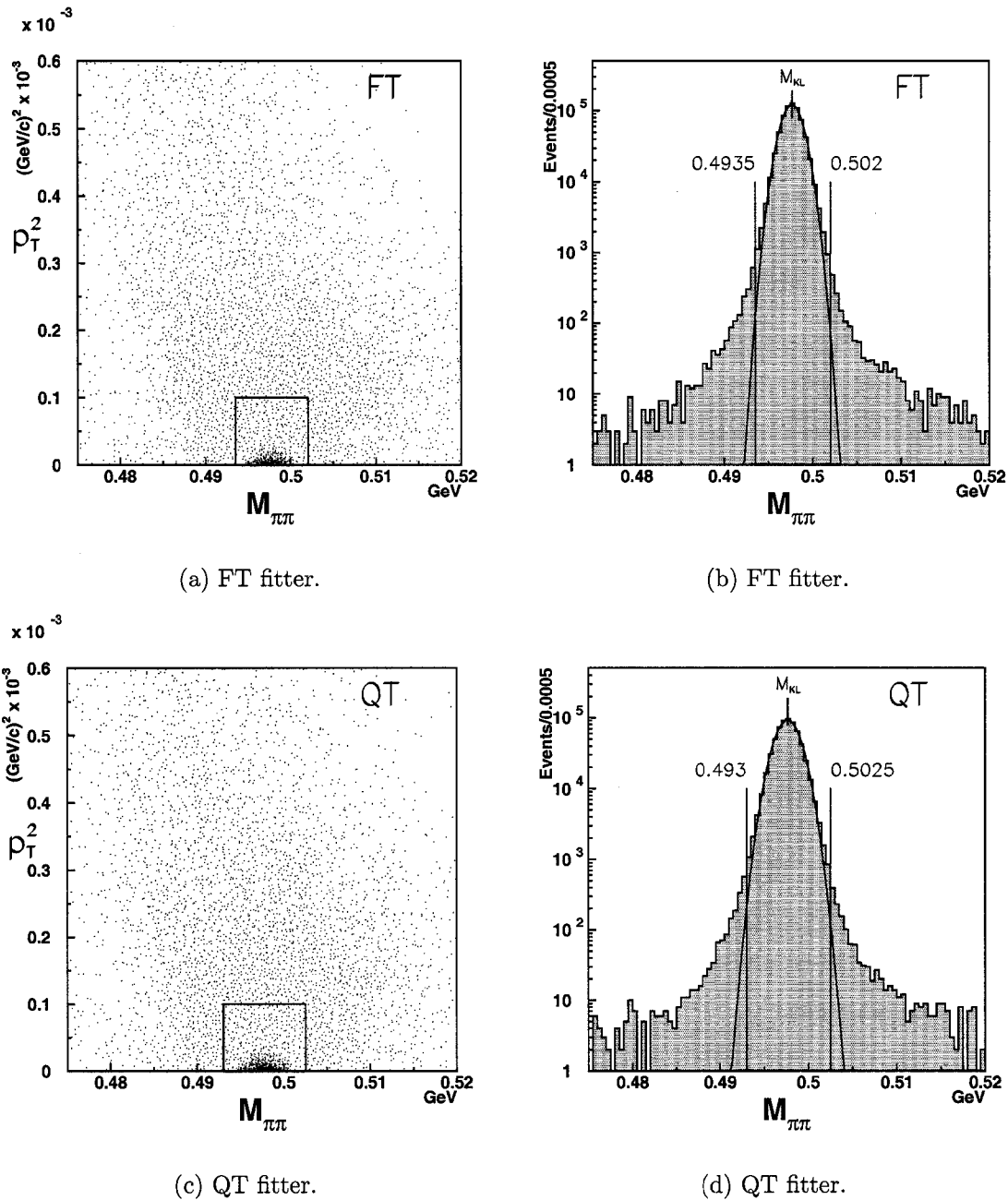
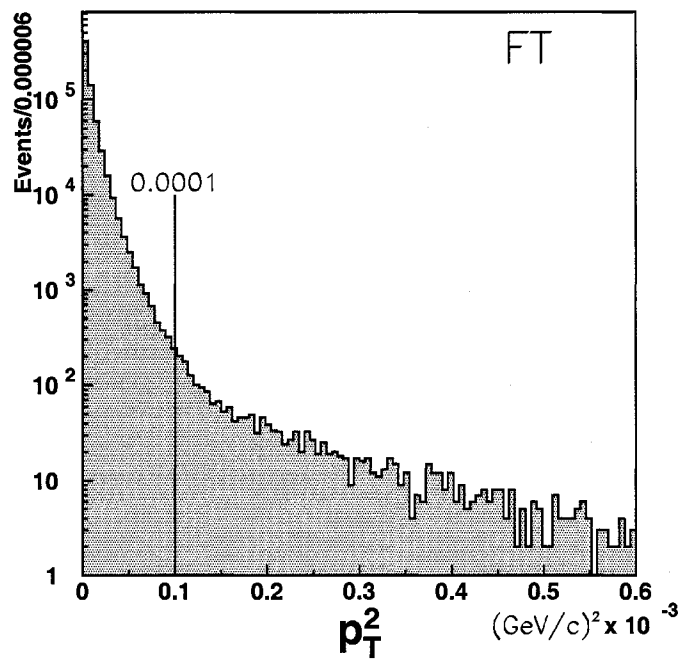
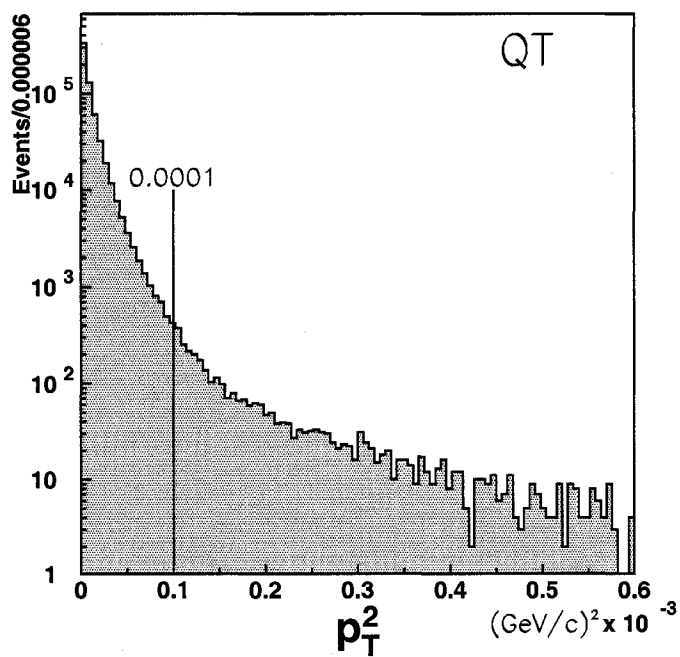


Figure 6.26: Invariant mass versus transverse momentum distributions for Monte Carlo $K_L^0 \rightarrow \pi^+\pi^-$ events which pass all two-body cuts are shown in (a) and (c). (b) and (d) are the projections of the distributions in (a) and (c) onto the mass axis. The box represents the signal region of $0.4935 < M_{\pi\pi ee} < 0.502$ GeV and $p_T^2 < 0.0001$ $(\text{GeV}/c)^2$ for the FT fitter and $0.493 < M_{\pi\pi ee} < 0.5035$ GeV and $p_T^2 < 0.01$ $(\text{GeV}/c)^2$ for the QT fitter.



(a) FT fitter.



(b) QT fitter.

Figure 6.27: Transverse momentum squared distributions for Monte Carlo $K_L^0 \rightarrow \pi^+\pi^-$ events which pass all two-body cuts are shown for the FT and QT fitters.

| FT fitter: | | | |
|--|---|------------------------------------|------------------------------------|
| | Normalization $K_L^0 \rightarrow \pi^+\pi^-$ | Phenomenological model | χ pt model |
| events pass all cuts & in signal region | 684313 | 13864 | 8807 |
| events generated | 57 510 000 | 134 869 000 | 23 393 000 |
| Acceptance | $(1.190 \pm 0.001) \times 10^{-2}$ | $(1.028 \pm 0.009) \times 10^{-4}$ | $(3.765 \pm 0.041) \times 10^{-4}$ |
| $\frac{A_{\pi\pi}}{A_{\pi\pi ee}}$ | - | 115.75 ± 1.00 | 31.60 ± 0.34 |
| | | | |
| QT fitter: | | | |
| | Normalization $K_L^0 \rightarrow \pi^+\pi^-$ | Phenomenological model | χ pt model |
| events pass all cuts & in signal region | 617002 | 13784 | 8706 |
| events generated | 52 090 000 | 124 965 000 | 23 284 000 |
| Acceptance | $(1.185 \pm 0.002) \times 10^{-2}$ | $(1.103 \pm 0.009) \times 10^{-4}$ | $(3.739 \pm 0.040) \times 10^{-4}$ |
| $\frac{A_{\pi\pi}}{A_{\pi\pi ee}}$ | - | 107.39 ± 0.92 | 31.68 ± 0.34 |

Table 6.5: Acceptance summary for events reconstructed using the FT and QT fitter.

CHAPTER 7

Background

The background processes for this analysis comprise any non-signal event that can mimic a four-body final state and whose reconstructed properties allow the event to pass all the analysis cuts and enter the signal region for $K_L^0 \rightarrow \pi^+\pi^-e^+e^-$. For these events to be written to the $\pi^+\pi^-$ data stream, the trigger must identify two of the tracks, correctly or incorrectly, as pions. The final state products must also be consistent with originating from a common vertex which falls inside the neutral beam profile. In this chapter, the maximum level at which these processes contaminate the $K_L^0 \rightarrow \pi^+\pi^-e^+e^-$ signal region is investigated through Monte Carlo analysis. Due to the complicated nature of most of the decays and the need to track photons and neutral particles in many of them, a Geant3 toy Monte Carlo was used to model the geometric acceptances of these backgrounds in order to supplement the E871 analysis routines.

7.1 $K_L^0 \rightarrow \pi^+\pi^-\pi^0$

In other $K_L^0 \rightarrow \pi^+\pi^-e^+e^-$ searches such as KTeV and NA48, $K_L^0 \rightarrow \pi^+\pi^-\pi^0$ was the most troublesome background, as it occurs 4×10^5 times more frequently.

Two charged pions are created in the initial decay which can satisfy the two-body trigger requirements. The neutral pion can decay to two photons (98.80%) or to $e^+e^-\gamma$ (1.20%). For the former mode, it is necessary for one of the two photons to pair produce upstream of the first straw drift chamber to create an electron-positron tracks which can satisfy the partial track requirements. In the latter decay mode of the neutral pion, the e^+e^- pair is create initially and has a much high probability of projecting upstream to satisfy the four-body selection criteria. Fortunately, the tight trigger requirements that reduces the phase space for the signal also eliminates this background from the data sample. Only events with a two-body invariant mass hypothesis of at least 460 MeV are written to tape. The creation of a π^0 limits the charged pion pair to a maximum invariant mass of 362 MeV. Consequently, there is no acceptance for this decay due to the limited phase space.

7.2 Pileup Events

The background due to accidental coincidence between multiple K_L^0 decays is classified as pileup. The daughters from one K_L^0 are accepted into the spectrometer and satisfy the trigger requirements for a two-body decay. These two tracks must be identified as pions. Next, tracks from a separate temporally correlated K_L^0 decay, which may or may not be spatially correlated, create hits in the first and second straw drift chambers such that the stub-finding routine recognizes and accepts the partial tracks as originating from the two-body vertex. Another way in which a pileup event can occur is for a daughter from each of two different K_L^0 decays to be accepted into the spectrometer such that the pair of tracks satisfies the two-body trigger and particle identification requirements. Due to the resolution of the pattern recognition and FT and QT fitting routines, the K_L^0 decays must be highly correlated in space and time. The remaining charged daughters must create hits in

the first and second straw drift chambers that are reconstructed as an e^+e^- pair from a four body decay.

A pileup event which occurs according to the first mechanism is much more likely to be accepted into the data stream, but requires inefficiency in the stub-finding routines or accidental coincidence to mimic the four-body signal. The second mechanism is suppressed due to the geometric acceptance as well as the low probability of two K_L^0 decays showing a large spatial and temporal correlation.

In order to model the contribution of pileup events to the background, the E871 Monte Carlo routine was modified to simulate multiple K_L^0 decays per event. In the modified simulation, two K_L^0 are emitted from the target with random momentum distributed according to the E871 parameterization of the neutral beam [41] and are forced to decay inside the vacuum decay region. Each kaon was allowed to decay through one of seven modes listed in Table 7.1 according to their normalized branching fractions.

This simulation did not measure the single event sensitivity for pileup decays in E871, but did allow the shape of the expected background distribution for the four-body invariant mass to be generated. The Monte Carlo background's shape was used to fit the candidate event set's invariant mass distribution (Chapter 8) so that the number of background events could be measured. In order to calculate the expected number of pileup events in the E871 data set, the structure of the neutral beam must be known. But due to the fluctuations in the intensity and pulse structure of the AGS, the precise distribution of K_L^0 's in time for a spill is not known. In order to determine if these events would contribute to the background of $K_L^0 \rightarrow \pi^+\pi^-e^+e^-$, the effective branching ratios for pileup decays were found to be at the on the same order of magnitude as the signal. This was done using a Geant3 Monte Carlo simulation which used the most generic geometric acceptance.

The E871 pileup simulation was run over a period of 8 weeks on the 8 duel-

| Decay Channel | Branching Ratio |
|---|-----------------|
| $K_L^0 \rightarrow \pi^\pm e^\mp \nu_e$ | 40.53% |
| $K_L^0 \rightarrow \pi^\pm \mu^\mp \nu_\mu$ | 27.02% |
| $K_L^0 \rightarrow \pi^0 \pi^0 \pi^0$ | 19.56% |
| $K_L^0 \rightarrow \pi^+ \pi^- \pi^0$ | 12.56% |
| $K_L^0 \rightarrow \pi^+ \pi^-$ | 0.1976% |

Table 7.1: Branching fractions for the decay channels used in the pileup event simulation.

processing nodes of the NOVA cluster at The College of William and Mary. Approximately 50 billion events were generated and analyzed using the FT fitter. The resulting sample consisted of 125 events which pass the $K_L^0 \rightarrow \pi^+ \pi^- e^+ e^-$ selection requirements and have a four-body transverse momentum less than 10 MeV. The 4-body invariant mass spectrum is shown in Figure 7.1. Since the muon identification routines were not implemented in the E871 Monte Carlo, an artificial muon veto was imposed using the measured efficiency of the muon rangefinder and hodoscope to cut 97% of all the events which contain a track known to be a muon.

7.3 $K_L^0 \rightarrow \pi^+ \pi^- \gamma$

$K_L^0 \rightarrow \pi^+ \pi^- \gamma$ decays, with a branching fraction of 4.17×10^{-5} , can contribute as background to $K_L^0 \rightarrow \pi^+ \pi^- e^+ e^-$ in E871 if the photon converts to a Dalitz pair upstream of the second layer of straws in the first drift chamber. In this case, the final products are the same as those of the signal. These events would be difficult to remove from the sample as the tracking resolution for stubs is not sufficient to conclusively differentiate the Dalitz pair's vertex as originating from the material in the downstream end of the vacuum decay tank rather than matching the primary pion vertex. Due to the large Lorentz boost and subsequent small opening angle between the positron and electron, the pair leaves hits in the front drift

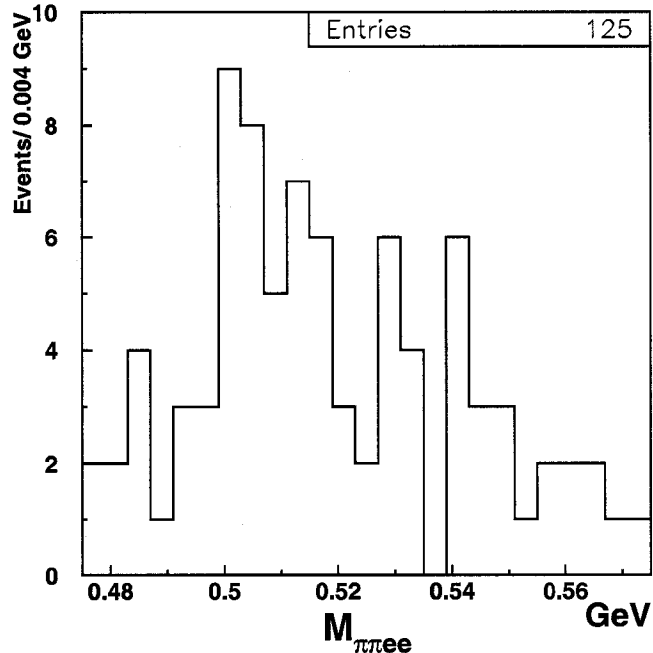


Figure 7.1: Invariant mass spectrum for pileup background events which pass the $K_L^0 \rightarrow \pi^+\pi^-e^+e^-$ acceptance criteria.

chambers that are nearly parallel to the photon that produced it. When projected upstream into the decay tank, the stub tracks can satisfy the stub to vertex DOCA requirement. The invariant mass for such a decay should reconstruct close to the K_L^0 mass with low transverse momentum, leading to contamination of the sample.

The probability for a photon to undergo pair production as it travels in materials with fractional interaction length f_{λ_T} is

$$P_{pair}(f_{\lambda_T}(E)) = 1 - e^{-f_{\lambda_T}(E)}, \quad (7.1)$$

where

$$f_{\lambda_T} = \sum_{materials} \frac{\lambda^i}{\lambda_0^i}. \quad (7.2)$$

λ is the number of interaction lengths that the photon passes through for a given material and λ_0 is the momentum dependent pair production cross section [42] for

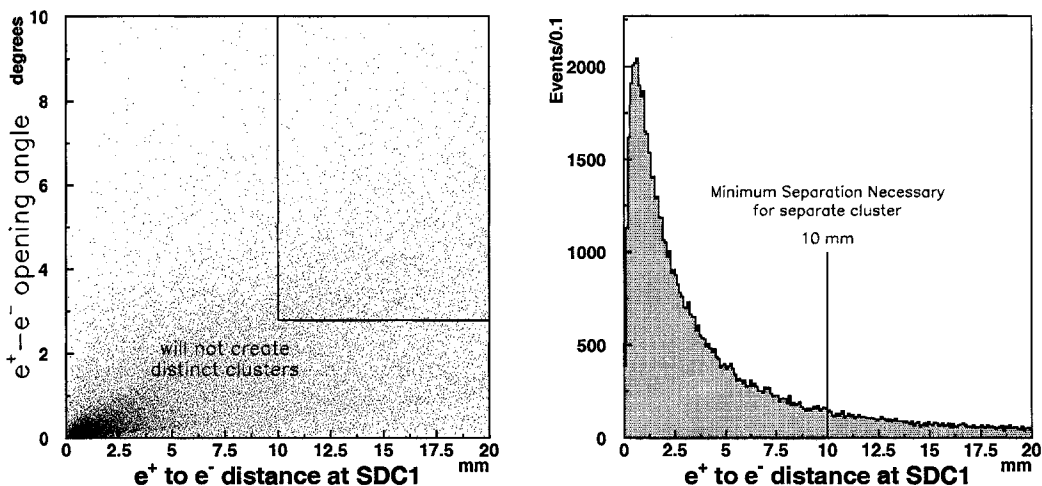
that material. The total fractional interaction length is a function of momentum and is shown in Figure 7.3(a). The pair production probability is also dependent on the energy of the photon and is plotted in Figure 7.3(b). Table 7.2 lists the materials present for conversion of the photon as well as the number of interaction lengths of each.

To find the total pair-production probability P_{total} upstream of the first drift chamber, Eq. (7.1) must be weighted by the energy distribution of the photon and integrated over all possible energies as in

$$P_{total} = \int_{0.002 \text{ GeV}}^{6 \text{ GeV}} P_{pair}(E) P_{\gamma}(E) dE. \quad (7.3)$$

$P_{\gamma}(E)$ is the probability that the decay $K_L^0 \rightarrow \pi^+\pi^-\gamma$ produces a photon of energy E . It was calculated from the photon energy spectrum, Figure 7.4, determined from a Geant3 simulation. From Eq. (7.3), the total probability of a photon from $K_L^0 \rightarrow \pi^+\pi^-\gamma$ giving a Dalitz pair that could mimic the signal is 1.237×10^{-3} .

The stub-finding routine requires that the each cluster of hits in a straw drift chamber can be associated with one partial track. An e^+e^- pair produced in the downstream vacuum window must have the tracks open up enough to create hits in the first x -viewing layer of straws that are consistent with two separate clusters. A Geant4 simulation was performed to measure the properties of the e^+ and e^- tracks in SDC1 and SDC2. The critical quantities are the distance between the tracks at the downstream end of the x -viewing straws in the first drift chamber and the opening angle between the tracks. The minimum separation necessary for hits in the third layer of x -viewing tracks to register as separate clusters is 10 mm. If the hits are any closer, the straws will be geometrically contiguous and only show up as one cluster. Similarly, if the opening angle between the tracks is less than 2.8° , the separation distance can not be greater than 10 mm. This assumes that the photon pair produces at the upstream end of the Kevlar/Mylar vacuum decay windows.



(a) Opening angle versus Separation distance.

(b) Separation distance at third straw layer of SDC1.

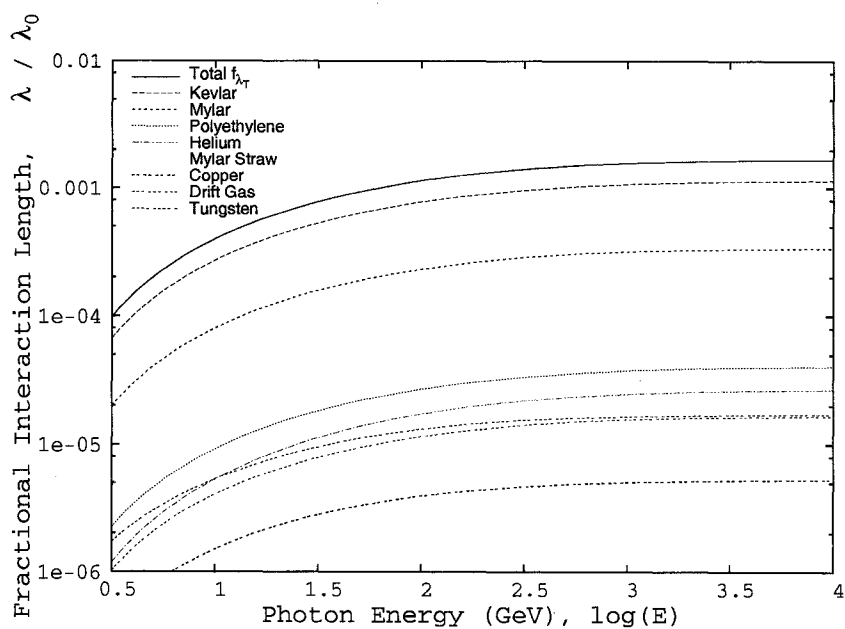
Figure 7.2: (a) The opening angle for the e^+ and e^- tracks created from the pair production of a photon in $K_L^0 \rightarrow \pi^+\pi^-\gamma$ events versus the separation distance at the first straw drift chamber. (b) Track separation distance for pair produced e^+ and e^- tracks at the front layer of SDC1.

Figure 7.2 shows the distribution of $\gamma \rightarrow e^+e^-$ events for these critical quantities. The probability of the e^+ and e^- tracks passing both requirements is 0.1075.

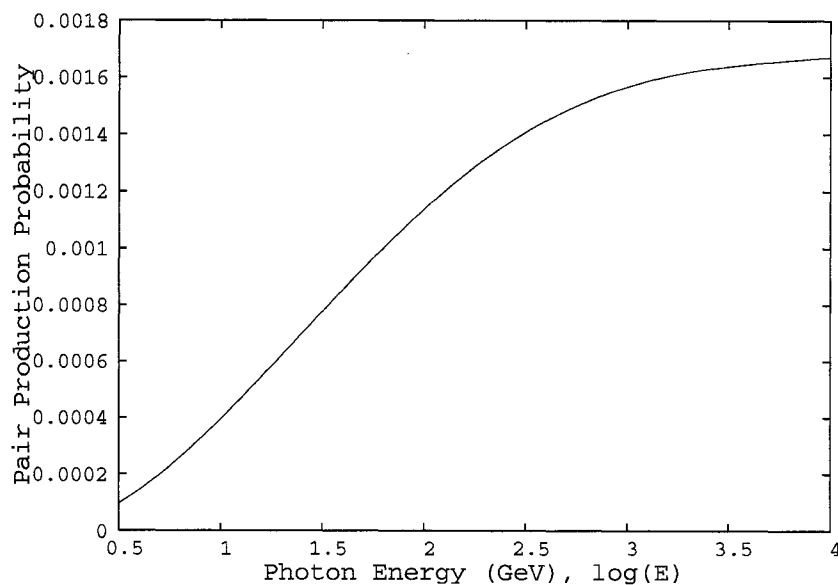
The effective branching ratio of for the process $K_L^0 \rightarrow \pi^+\pi^-(\gamma \rightarrow e^+e^-)$ is 5.544×10^{-9} . An upper bound of 0.02 events is placed on the expected background from this channel using the effective branching ratio combined with the geometric acceptance computed with Geant3.

7.4 $K_L^0 \rightarrow l^+l^-\gamma$ and $K_L^0 \rightarrow (l^+l^-)(l^+l^-)$

The leptonic decays $K_L^0 \rightarrow \mu^+\mu^-\gamma$ and $K_L^0 \rightarrow e^+e^-\gamma$ have branching ratios of 3.59×10^{-7} and 1.0×10^{-5} , respectively, and can contaminate the signal in a manner similar to $K_L^0 \rightarrow \pi^+\pi^-\gamma$. In each case, the photon must convert to a Dalitz pair to create the required four daughter particles. In addition, the primary lepton tracks



(a) Total Fractional Interaction length, calculated from Eq. (7.2), for the sum of all the materials listed in Table ??



(b) Probability of a photon undergoing pair production, calculated from Eq. (7.1) using the total fractional interaction length (Eq. (7.2)).

Figure 7.3: Fractional Interaction lengths and pair production probabilities for photons in the material prior to the second layer of x-viewing straws in SDC1.

| Material | Thickness (cm) | Density (g/cm ³) | Interaction Length (g/cm ²) |
|--|----------------------|------------------------------|---|
| Kevlar 29 | 0.0432 | 1.44 | 0.06218 |
| Mylar | 0.0127 | 1.40 | 0.1778 |
| Polyethylene | 0.0254 | 0.94 | 0.2388 |
| Helium | 18.3 | 1.79×10^{-4} | 0.003276 |
| Mylar Straw | 0.003 | 1.40 | 0.0042 |
| Copper | 1.0×10^{-5} | 8.92 | 8.92×10^{-5} |
| Drift Gas (CF ₄ C ₂ H ₆) | 0.4 | 0.002 | 0.0008 |
| Tungsten | 8.0×10^{-6} | 19.25 | 0.000154 |

Table 7.2: Properties of materials prior to the second layer of straws in SDC1 for use in pair production calculations.

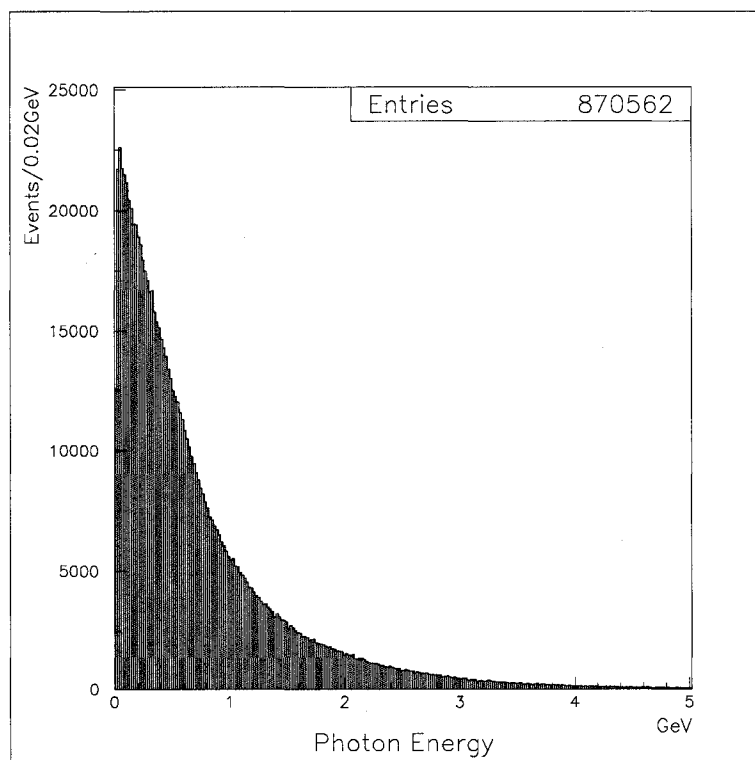


Figure 7.4: The Photon energy distribution for $K_L^0 \rightarrow \pi^+ \pi^- \gamma$ in the lab frame, from Geant3 MC.

| Decay Branch | Branching Ratio | MisID Probability | Pair Production Probability | Expected Background |
|---|-----------------------|-----------------------|-----------------------------|--------------------------|
| $K_L^0 \rightarrow \mu^+ \mu^- \gamma$ | 3.59×10^{-7} | 1.09×10^{-3} | 1.2×10^{-3} | $< 1.812 \times 10^{-4}$ |
| $K_L^0 \rightarrow e^+ e^- \gamma$ | 1.0×10^{-5} | 1.21×10^{-4} | 1.2×10^{-3} | $< 5.61 \times 10^{-4}$ |
| $K_L^0 \rightarrow \mu^+ \mu^- e^+ e^-$ | 2.69×10^{-9} | 1.09×10^{-3} | | $< 1.13 \times 10^{-3}$ |
| $K_L^0 \rightarrow e^+ e^- e^+ e^-$ | 3.56×10^{-8} | 1.21×10^{-4} | | $< 1.66 \times 10^{-3}$ |

Table 7.3: Properties of the leptonic background decay modes along with the expected number of background events for each.

must both be misidentified by the particle identification routines in order for the E871 trigger to accept the event into the $\pi^+\pi^-$ data stream. In order to get an upper limit on the contamination of these decays, the conversion probability for a 2 GeV photon was found from Figure 7.3(b) and combined with the probabilities for misidentification of the dilepton tracks as dipion tracks.

$$N_{background} = N_{\pi\pi} \cdot \frac{B(K_L^0 \rightarrow \ell^+ \ell^- \gamma) \cdot P_{misid} \cdot P_{\gamma \rightarrow e^+ e^-}}{B(K_L^0 \rightarrow \pi^+ \pi^-)} \quad (7.4)$$

$N_{\pi\pi}$ is the number of $K_L^0 \rightarrow \pi^+\pi^-$ events found in the normalization analysis (Sec. 8.2). P_{misid} is the probability of misidentifying both of the primary tracks as pions, and $P_{\gamma \rightarrow e^+ e^-}$ is the probability of pair production forward of the second layer of straws in SDC1. Table 7.3 lists the misidentification and conversion probabilities along with the upper limit on the expected number of background decays in the signal region.

The background due to the four body leptonic decays is small in the $\pi^+\pi^-$ data stream. In this case, the four-daughter final state is produced initially, but two of the four leptons must be misidentified as pions. As with $K_L^0 \rightarrow \pi^+\pi^- e^+ e^-$, there is an enhancement to the acceptance for $K_L^0 \rightarrow \mu^+ \mu^- e^+ e^-$ due to form factors which increase likelihood of the $\mu^+ \mu^-$ invariant mass being above the trigger threshold. But, the branching ratios for the leptonic four-body decays are already smaller than the signal's before the misidentification probability is even taken into account.

Table 7.3 shows the branching ratios and the upper limit on the expected number of background events for these decay modes.

CHAPTER 8

Event Counting

8.1 Overview

To calculate the branching fraction for $K_L^0 \rightarrow \pi^+\pi^-e^+e^-$, it is necessary to find the number of events in the data sample which can be classified as the normalization $K_L^0 \rightarrow \pi^+\pi^-$, $N_{\pi\pi}$ and the number of events which can be classified as the signal $K_L^0 \rightarrow \pi^+\pi^-e^+e^-$, $N_{\pi\pi ee}$. These sets of events are mutually exclusive. The candidate samples are found by applying the kinematic and particle ID requirements described in Chapter 6 and examining the resulting distributions in invariant mass and transverse momentum. Each sample contains background which must be accounted for by matching the expected background distributions from Monte Carlo to the candidate distributions. The procedure used for calculating $N_{\pi\pi}$ and $N_{\pi\pi ee}$ is outlined in the following sections.

8.2 Normalization Sample

In order to measure the branching fraction of a decay mode, the total number of particle decays must be known, which in the case of E871 was not possible.

The number of K_L^0 which decay in the vacuum region, $N_{K_L^0}^{decay}$, can be calculated by measuring the number of events for a decay channel whose branching ratio and acceptance are well known. The ideal choice for this calculation is the $K_L^0 \rightarrow \pi^+\pi^-$ mode as it has a high acceptance and a well-measured branching fraction ($B(K_L^0 \rightarrow \pi^+\pi^-) = (1.976 \pm 0.008) \times 10^{-3}$ [19]). In this case,

$$N_{K_L^0}^{decay} = \frac{N_{\pi\pi}}{B(K_L^0 \rightarrow \pi^+\pi^-) \cdot A_{\pi\pi}}, \quad (8.1)$$

where $N_{\pi\pi}$ is the number of $K_L^0 \rightarrow \pi^+\pi^-$ events occurring within the vacuum tank fiducial volume and $A_{\pi\pi}$ is the related Monte Carlo measured acceptance. The $K_L^0 \rightarrow \pi^+\pi^-$ events were reconstructed from the same data sample as the signal events and were reconstructed from pattern recognition and the FT and QT fitters. The same requirements were applied to the pion tracks in the $K_L^0 \rightarrow \pi^+\pi^-$ events as in $K_L^0 \rightarrow \pi^+\pi^-e^+e^-$ events. Details for this are given in Chapter 6.

The selection criteria for counting $K_L^0 \rightarrow \pi^+\pi^-$ events are summarized in Table 8.1. As the electron particle identification routines were implemented in the E871 Monte Carlo, the electron identification requirements (Sec. 6.3) were imposed on the data as well. The efficiency of the electron veto reduces the background from K_{e3} decays to negligible levels (on the order of 1%). The muon identification requirement is not included in the selection criteria because the routines for the muon rangefinder and the muon hodoscope are not fully implemented in the E871 Monte Carlo. Due to this exclusion, the dominant background for the normalization sample are $K_{\mu 3}$ events which contaminate the signal region at a level of 10%. The invariant mass for $K_{\mu 3}$ under a $\pi^+\pi^-$ hypothesis has a kinematic endpoint of 514 MeV/ c^2 . This results in a broad-shaped spectra for both $M_{\pi\pi}$ and p_T^2 as shown in Figure 8.1.

After applying the analysis cuts as well as the transverse momentum requirement of $p_T^2 < 0.0001$ (GeV/ c)² to the minimum bias data, a spectrum peaked at

| Selection Quantity | Cut Value |
|------------------------------|--------------------------------|
| $ V_x $, vertex angle - x | < 0.0027 radians |
| $ V_y $, vertex angle - y | < 0.01 radians |
| V_z , vertex position - z | $9.55 < V_x < 20.6$ meters |
| χ_{trk}^2 (FT) | < 25 |
| χ_{vtx}^2 (FT) | < 30 |
| χ_{trk}^2 (QT) | < 35 |
| χ_{vtx}^2 (QT) | < 15 |
| $ \vec{p} $, track momentum | $1.05 < \vec{p} < 6.5$ GeV/c |

Table 8.1: Selection criteria for reconstructing normalization events. The choice of fitter will determine whether the FT or QT χ^2 cuts will be used.

the K_L^0 mass is formed for the invariant mass of two pions (Figure 8.2(a) for the FT analysis and Figure 8.3(a) for the QT analysis). This peak stands upon a slowly varying background of $K_{\mu 3}$ events. In order to measure and subtract this background from the signal region, the $K_{\mu 3}$ Monte Carlo distribution is area-normalized to the sideband regions of $0.475 \leq M_{\pi\pi} \leq 0.488$ GeV and $0.505 \leq M_{\pi\pi} \leq 0.520$ GeV where the background is dominant. The buffer regions are necessary to separate $K_L^0 \rightarrow \pi^+\pi^-$ events which have been shifted out of the signal region from the background region. This shift is evident mainly in a low mass tail which is due to bremsstrahlung interactions of the pions and accounts for a reduction in the invariant mass. The number of $K_{\mu 3}$ background events in the signal region can be found from

$$N_{K_{\mu 3}}^{SigReg.} = M_{K_{\mu 3}}^{SigReg.} \cdot \frac{N_{K_{\mu 3}}^{Sideband}}{M_{K_{\mu 3}}^{Sideband}}, \quad (8.2)$$

where $N_{K_{\mu 3}}^{SigReg.}$ and $N_{K_{\mu 3}}^{Sideband}$ are the number of background events in the signal and sideband regions, respectively and $M_{K_{\mu 3}}^{SigReg.}$ and $M_{K_{\mu 3}}^{Sideband}$ are the number of Monte Carlo background events in the signal and sideband regions, respectively. The error

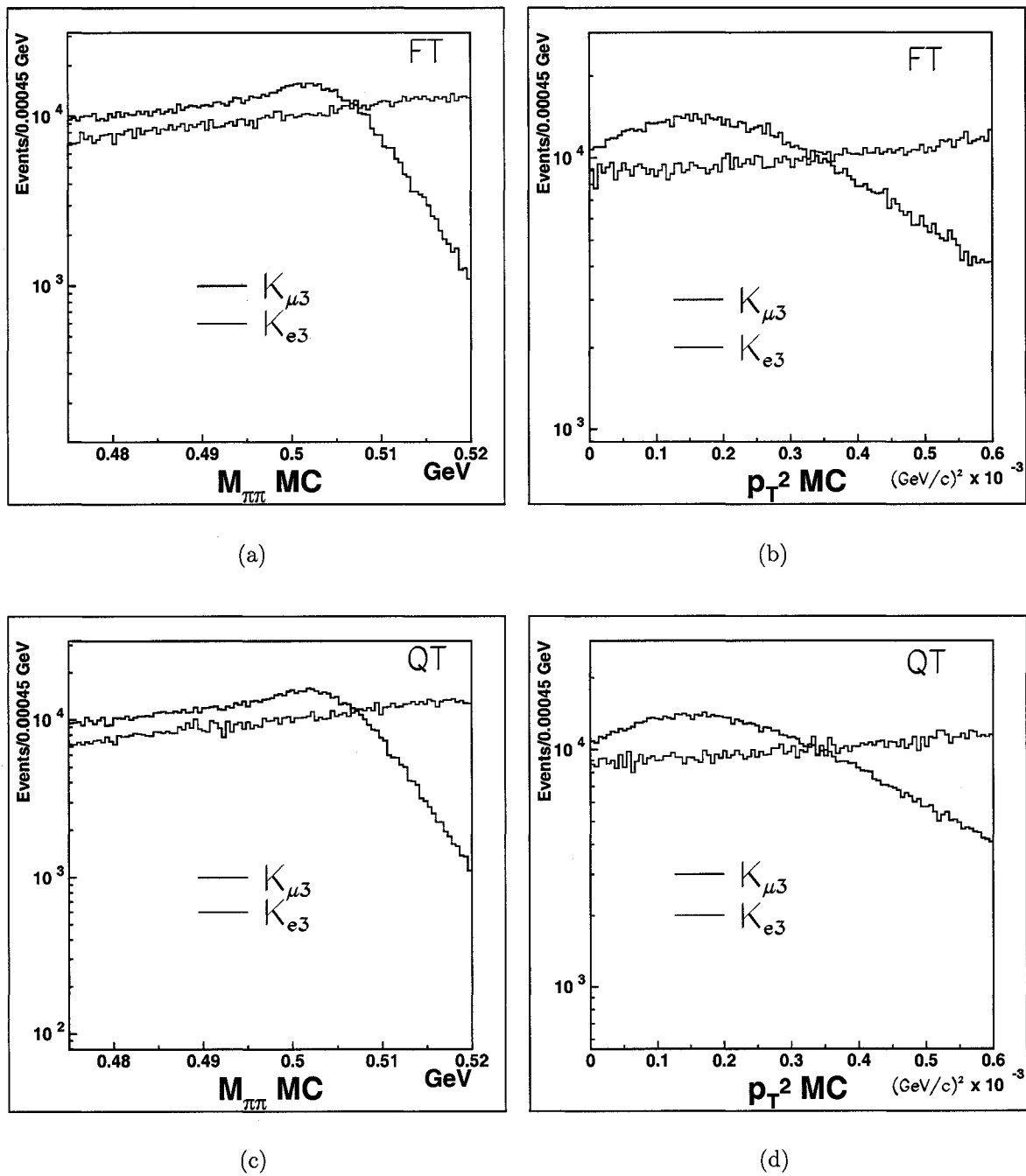


Figure 8.1: Mis-identified $K_{\mu 3}$ and $K_{e 3}$ reconstruction under a $\pi^+\pi^-$ hypothesis. The relative contribution of $K_{\mu 3}$ to $K_{e 3}$ is not represented here. The plots are area normalized to show the shape of the distributions.

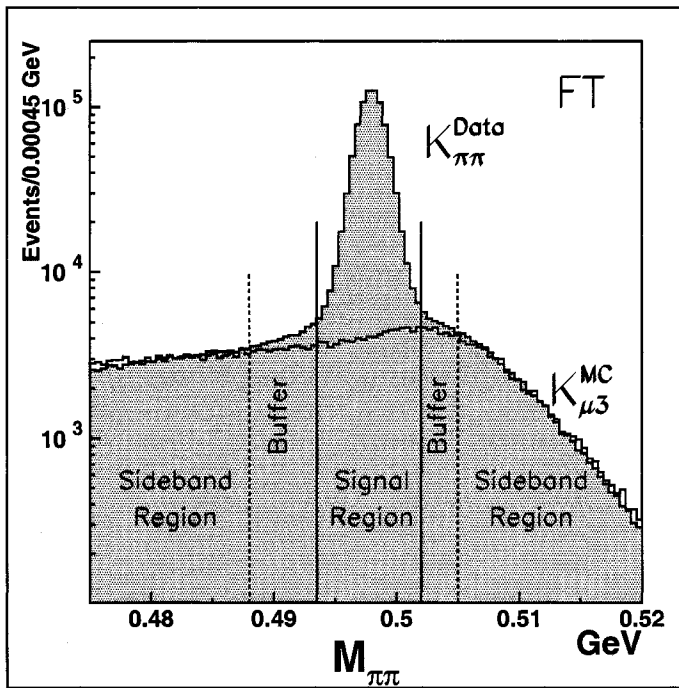
on the number of background events in the signal region is

$$\sigma_{bkgd}^2 = M_{K\mu 3}^{SigReg.} \left(\frac{N_{K\mu 3}^{Sideband}}{M_{K\mu 3}^{Sideband}} \right)^2 + \frac{(M_{K\mu 3}^{SigReg.})^2 N_{K\mu 3}^{Sideband}}{(M_{K\mu 3}^{Sideband})^2} + \frac{(M_{K\mu 3}^{SigReg.})^2 (N_{K\mu 3}^{Sideband})^2}{(M_{K\mu 3}^{Sideband})^3}, \quad (8.3)$$

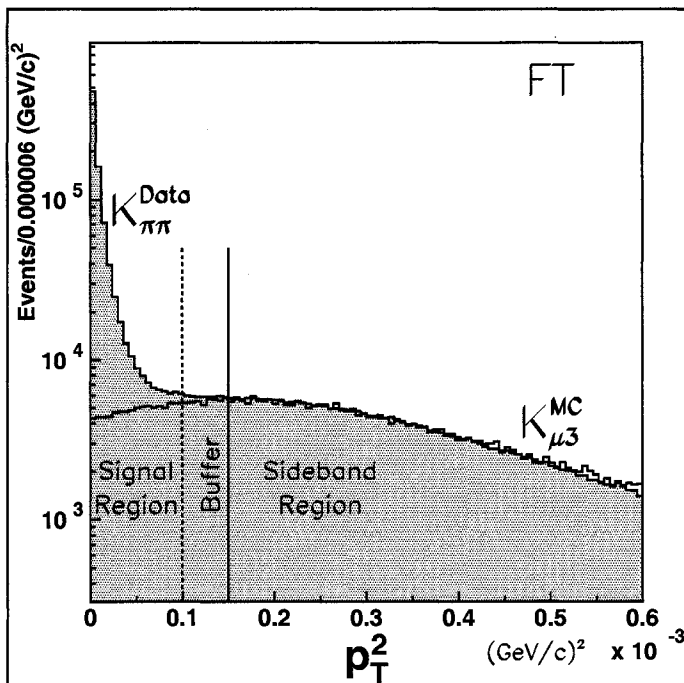
which assumes binomial statistics and independence of errors [35]. The tables in Figure 8.2(b) and Figure 8.3(b) give the background subtracted results as well as the statistical errors on both the signal and background. The statistical error on the signal was found by adding in quadrature those from the total sample and from the background.

The sideband analysis was done for the signal region projected onto the transverse momentum axis as well. Events must have passed all the cuts in Table 8.1 and must be in the invariant mass signal region for the appropriate fitter. The sideband region was set to $0.00015 \leq p_T^2 \leq 0.0006$ (GeV/c)² with a buffer region beginning at $p_T^2 = 0.00005$ (GeV/c)² down to the signal region ($p_T^2 < 0.0001$ (GeV/c)²). Figure 8.2(d) and Figure 8.3(d) show the results and errors from sideband analysis in the transverse momentum sector.

The number of $K_L^0 \rightarrow \pi^+\pi^-$ events was found by averaging the results from the invariant mass and transverse momentum methods and taking the larger statistical error. The difference in the normalized backgrounds from the transverse momentum and mass methods was 4.4% for the FT fitter and 5.5% for the QT fitter and was used as a measure of the systematic error in using this background subtraction method. The total error was found by adding the statistical uncertainty in quadrature with half of the normalized background difference. Table 8.2 shows the results and errors associated with the FT and QT fitters.

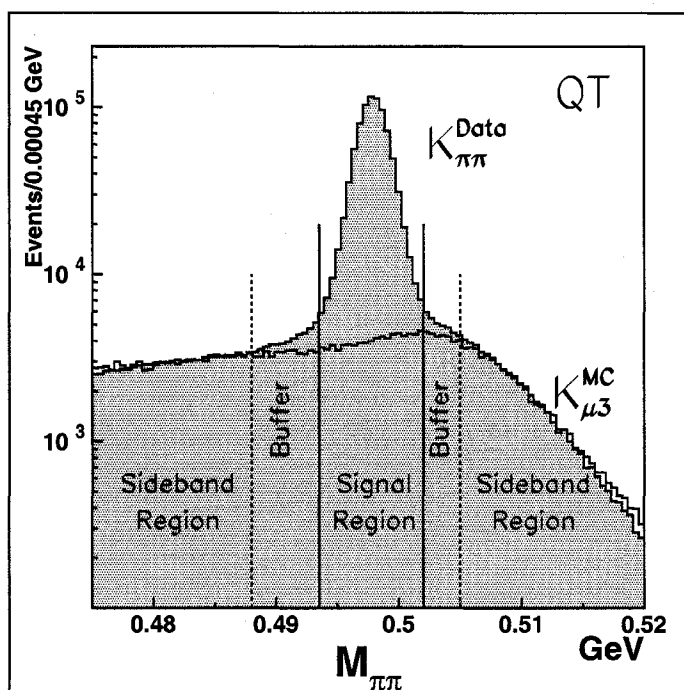
(a) $M_{\pi\pi}$ sideband analysis.

| $M_{\pi\pi}$ | $N \pm \sigma$ |
|-------------------|-------------------|
| Total: | 871474 ± 933 |
| <u>Background</u> | |
| low sideband: | 77632 ± 758 |
| high sideband: | 77032 ± 952 |
| average: | 77332 ± 608 |
| Signal: | 794144 ± 1114 |
| Bkgd/Sig: | 0.0978 |

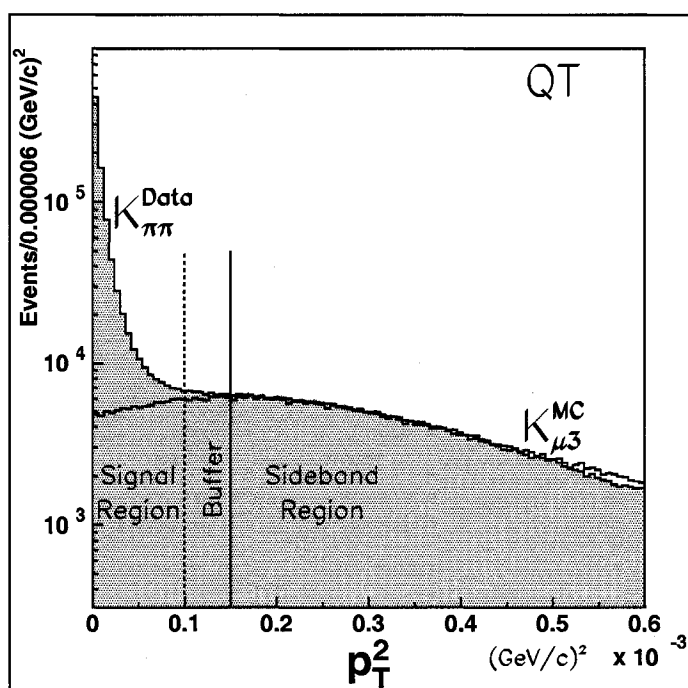
(b) $M_{\pi\pi}$ analysis results.(c) p_T^2 sideband analysis.

| p_T^2 | $N \pm \sigma$ |
|-------------|-------------------|
| Total: | 871474 ± 933 |
| Background: | 80788 ± 632 |
| Signal: | 790687 ± 1127 |
| Bkgd/Sig: | 0.1022 |

(d) p_T^2 analysis results.Figure 8.2: Background subtraction results for the $K_L^0 \rightarrow \pi^+\pi^-$ sample analyzed with the FT fitter.

(a) $M_{\pi\pi}$ sideband analysis.

| $M_{\pi\pi}$ | $N \pm \sigma$ |
|----------------|-------------------|
| Total: | 871560 ± 933 |
| Background | |
| low sideband: | 85005 ± 686 |
| high sideband: | 83451 ± 872 |
| average: | 84228 ± 555 |
| Signal: | 787332 ± 1086 |
| Bkgd/Sig: | 0.1071 |

(b) $M_{\pi\pi}$ analysis results.(c) p_T^2 sideband analysis.

| p_T^2 | $N \pm \sigma$ |
|-------------|-------------------|
| Total: | 871560 ± 933 |
| Background: | 89004 ± 551 |
| Signal: | 782556 ± 1083 |
| Bkgd/Sig: | 0.1137 |

(d) p_T^2 analysis results.Figure 8.3: Background subtraction results for the $K_L^0 \rightarrow \pi^+\pi^-$ sample analyzed with the QT fitter.

| FT fitter | $N_s \pm \sigma_s [\sigma_s/N_s]$ | $N_b \pm \sigma_b [\sigma_b/N_b]$ |
|----------------------|-----------------------------------|---|
| $M_{\pi\pi}$ Region: | $794114 \pm 1114 [0.0014]$ | $77332 \pm 608 [0.0079]$ |
| p_T^2 Region: | $790687 \pm 1127 [0.0014]$ | $80788 \pm 632 [0.0078]$ |
| Average: | $792416 \pm 2063 [0.0026]$ | $\sigma_{sys} = \frac{1}{2}\Delta N_b = 1728$ |
| QT fitter | $N_s \pm \sigma_s [\sigma_s/N_s]$ | $N_b \pm \sigma_b [\sigma_b/N_b]$ |
| $M_{\pi\pi}$ Region: | $787332 \pm 1086 [0.0014]$ | $84228 \pm 555 [0.0066]$ |
| p_T^2 Region: | $782556 \pm 1083 [0.0014]$ | $89004 \pm 551 [0.0062]$ |
| Average: | $784994 \pm 2623 [0.0033]$ | $\sigma_{sys} = \frac{1}{2}\Delta N_b = 2388$ |

Table 8.2: $K_L^0 \rightarrow \pi^+\pi^-$ events in the normalization sample when reconstructed with the FT and QT fitters.

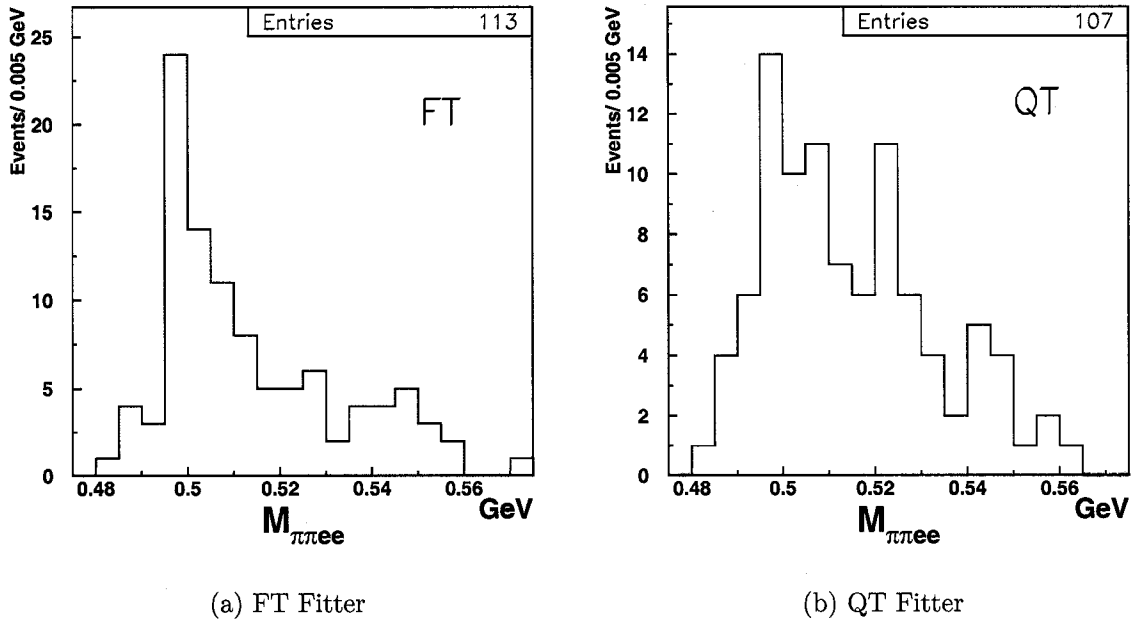


Figure 8.4: Candidate samples for the FT and QT fitters. None of the events in the samples are part of the normalization sample and have passed two and four-body selection requirements as well as particle ID.

8.3 $K_L^0 \rightarrow \pi^+\pi^-e^+e^-$ Sample

Figure 8.4 shows the $K_L^0 \rightarrow \pi^+\pi^-e^+e^-$ candidate event samples as functions of the four-body invariant mass in the region $0.475 \geq M_{\pi\pi ee} \geq 0.575$ GeV. These samples include the pion track cuts, shown in Tables 6.2 and 6.3, and the e^+/e^- partial track cuts, shown in Table 6.4, along with the particle identification requirements described in Chapter 6, Sec. 6.3. The four-body transverse momentum of each event was required to be less than 10 MeV/c. To ensure that the $K_L^0 \rightarrow \pi^+\pi^-$ normalization and $K_L^0 \rightarrow \pi^+\pi^-e^+e^-$ signal samples were mutually exclusive, any events which were accepted into the normalization signal region described in the previous section were removed from the $K_L^0 \rightarrow \pi^+\pi^-e^+e^-$ sample. The remaining events form the candidate event samples that contain 113 and 107 events for the FT and QT fitters, respectively.

To extract the number of $K_L^0 \rightarrow \pi^+\pi^-e^+e^-$ events in the candidate sample, the

background in the signal region, $0.4905 \geq M_{\pi\pi ee} \geq 0.505$ GeV, must be measured. The dominant background is expected to be composed of pileup events in which two uncorrelated K_L^0 produce daughters that are accepted in the spectrometer, as described in Sec. 7.2. The invariant mass spectrum for the pileup background was simulated using the E871 Monte Carlo code for uncorrelated K_L^0 in the decay tank, but the sample contains 125 events. Due to the low statistics, the histogram matching method used with the normalization analysis was not practical. Instead, three sets of functions were used to fit the background sample. Each set contained a Gaussian distribution to match the peaked structure and either a Gaussian, a constant, or a second order polynomial to match the diffuse background under the peak:

$$B_g = \frac{A_1}{\sigma_1\sqrt{2\pi}}e^{-\frac{1}{2}\left(\frac{x-\mu_1}{\sigma_1}\right)^2} + \frac{A_2}{\sigma_2\sqrt{2\pi}}e^{-\frac{1}{2}\left(\frac{x-\mu_2}{\sigma_2}\right)^2} \quad (8.4)$$

$$B_c = \frac{A_1}{\sigma_1\sqrt{2\pi}}e^{-\frac{1}{2}\left(\frac{x-\mu_1}{\sigma_1}\right)^2} + C \quad (8.5)$$

$$B_p = \frac{A_1}{\sigma_1\sqrt{2\pi}}e^{-\frac{1}{2}\left(\frac{x-\mu_1}{\sigma_1}\right)^2} + (P_0 + P_1x + P_2x^2). \quad (8.6)$$

To remove any bias in the fit introduced by the bin choice for the histogram, bin widths of 4 MeV, 5 MeV, and 6 MeV as well as two different bin starting position. Two sets of histograms were constructed, one with a starting position of 0.475 GeV and a second with the starting position shifted by half of a binwidth. The 18 fits to the Monte Carlo background sample from pileup decays are shown in Figures 8.5 and 8.6.

The FT and QT candidate event samples shown in Figure 8.4 were fit to a distribution containing a Gaussian for the $K_L^0 \rightarrow \pi^+\pi^-e^+e^-$ peak and one of the three background functions. The distribution has the form

$$S_i = \frac{A_{sig}}{\sigma_{sig}\sqrt{2\pi}}e^{-\frac{1}{2}\left(\frac{x-\mu_{sig}}{\sigma_{sig}}\right)^2} + B_i, \quad (8.7)$$

where $i = g, c, p$. Fits were performed for bin widths of 4 MeV, 5 MeV, and 6 MeV and for shifted and unshifted bin starting positions. The mean, A_{sig} , and stan-

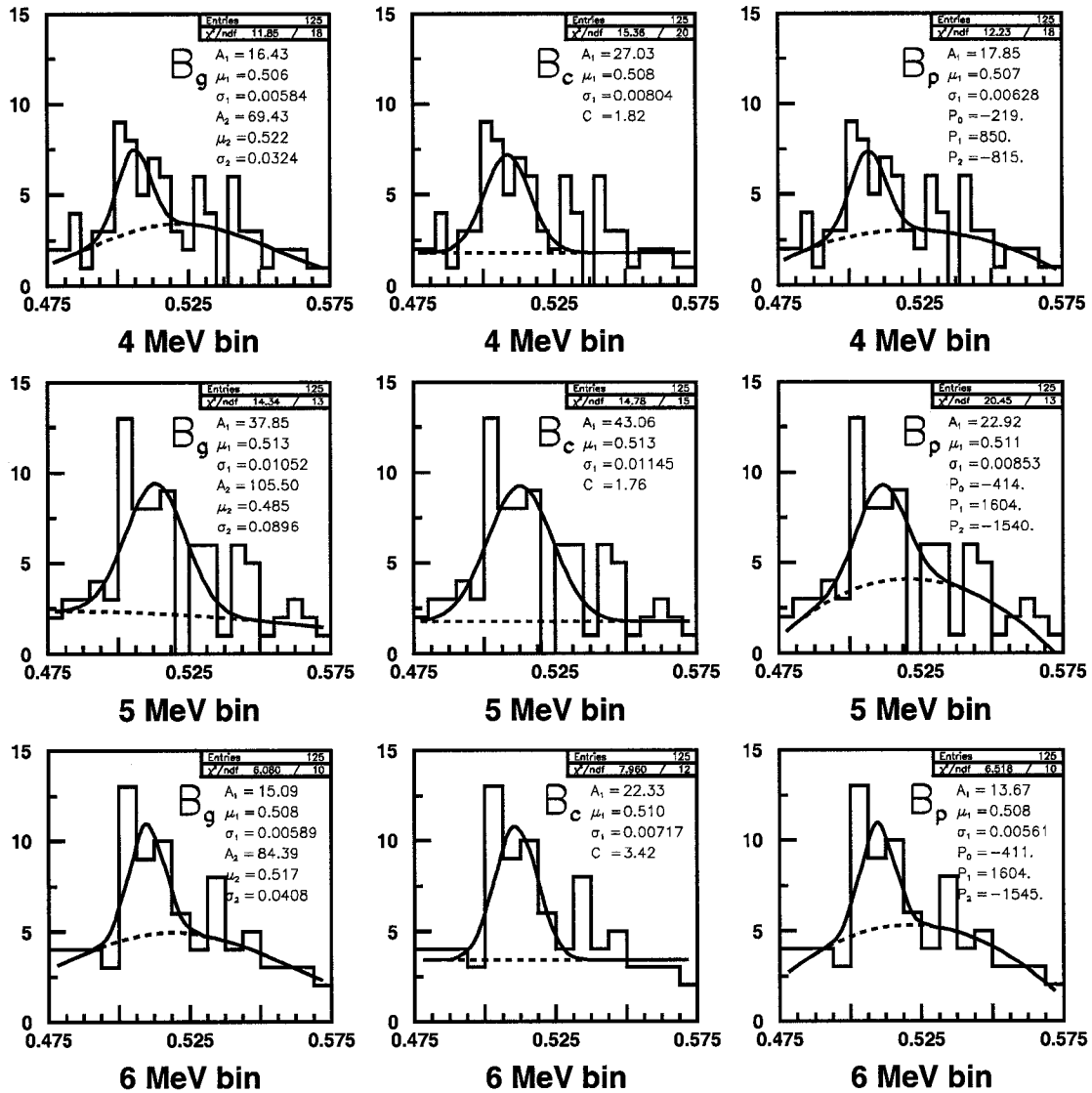


Figure 8.5: The pileup event sample from Monte Carlo plotted against four-body invariant mass was fit using three functions and three separate bin widths. The first bin in each histogram starts at 0.475 GeV. The plots in the first, second and third columns use the fit function B_g , B_c , B_p respectively, described in Equations (8.4), (8.5) and (8.6). The bin width for each plot is shown along the x-axis.

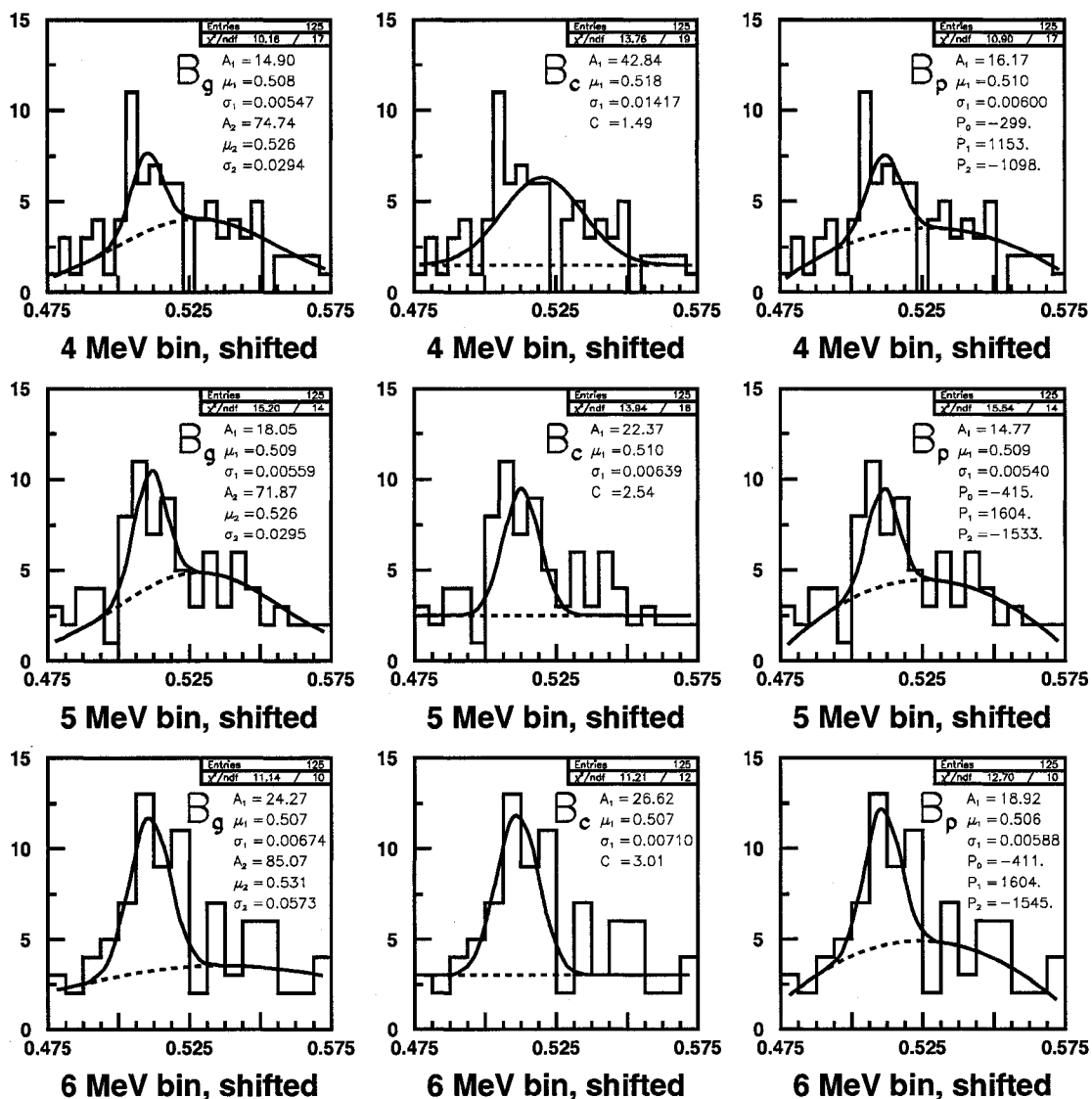


Figure 8.6: The pileup event sample from Monte Carlo plotted against four-body invariant mass was fit using three functions and three separate bin widths. The first bin in each histogram is shifted by one half of a bin compared to those from Figure 8.5. The plots in the first, second and third columns use the fit function B_g , B_c , B_p respectively, described in Equations (8.4), (8.5) and (8.6). The bin width for each plot is shown along the x -axis.

dard deviation, σ_{sig} were determined for each fitter from the accepted Monte Carlo four-body invariant mass distributions shown in Figure 8.7, and were fixed in all fits. The average of the phenomenological and χ PT model fits was used. The mean, A_1 , and standard deviation, σ_1 for the background Gaussians determined in Figures 8.5 and 8.6 were used for the corresponding bin width and shift in the candidate sample fits, and were held fixed. The amplitude of the signal and background Gaussians as well as all parameters in the constant and the parabolic diffuse background functions were allowed to vary. Figures 8.8 and 8.9 and Figures 8.10 and 8.11 show the 18 fits to the FT and QT candidate samples, respectively.

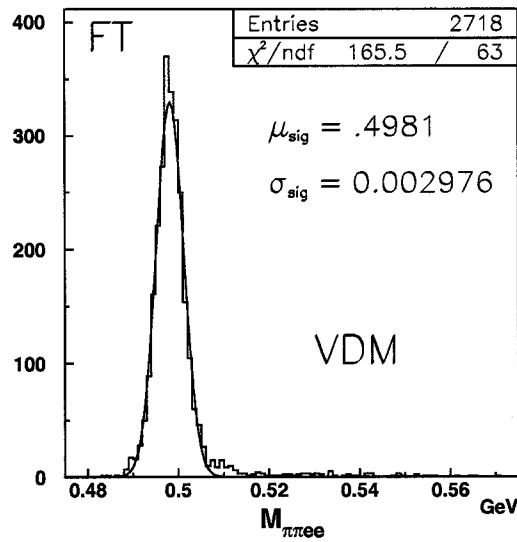
The number of pileup events in the signal region for each fit was found by integrating the background function over the region $0.4905 \geq M_{\pi\pi ee} \geq 0.505$. The results are shown in Tables 8.3 and 8.4. The average over all fit types and binning strategies was taken as the total number of background events in each of the FT and QT signal region:

$$FT : N_{\pi\pi ee}^{background} = 13.32 \pm 3.65(stat) \pm 3.18(sys) \quad (8.8)$$

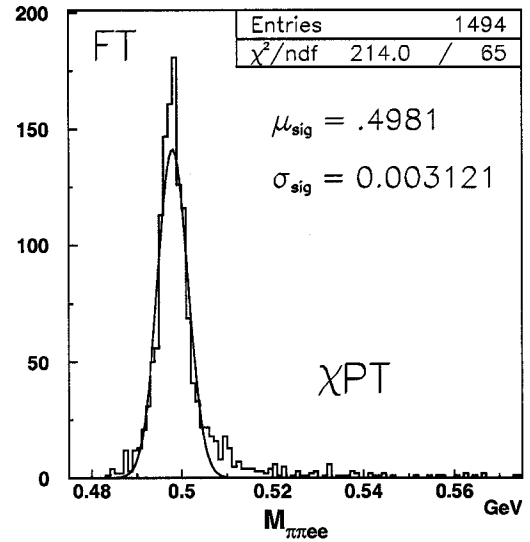
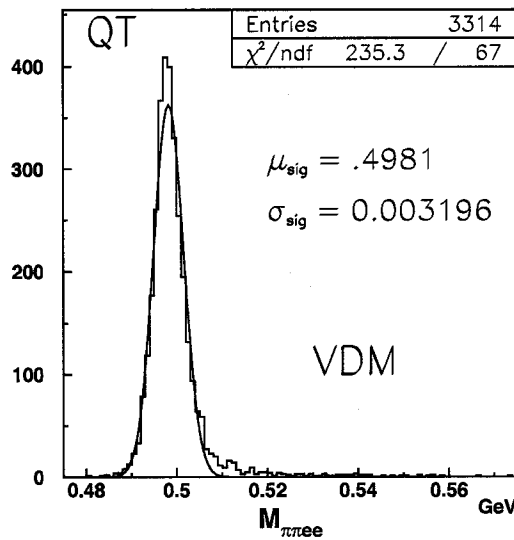
$$QT : N_{\pi\pi ee}^{background} = 14.05 \pm 3.74(stat) \pm 2.59(sys). \quad (8.9)$$

The systematic error in the background arises from two sources, the bin choice and the fit. For the bin choice, the average of the results for one bin width and shift is used, and then the maximum deviation above and below the mean determined. The systematic error on the bin is defined as half of the difference between the high and low deviations. The unshifted and shifted histograms were examined separately and then averaged. The analogous method was used for the systematic fitting error. The background results were averaged over the bin widths and half of the difference in the deviations was determined as the systematic error in the fit. The total systematic error on the background was the RMS of the fitting and binning systematics.

For the FT fitter, 41 of 113 candidate events fall in the invariant mass signal



(a) Phenomenological Model, FT Fitter

(b) χ PT Model, FT Fitter

(c) Phenomenological Model, QT Fitter

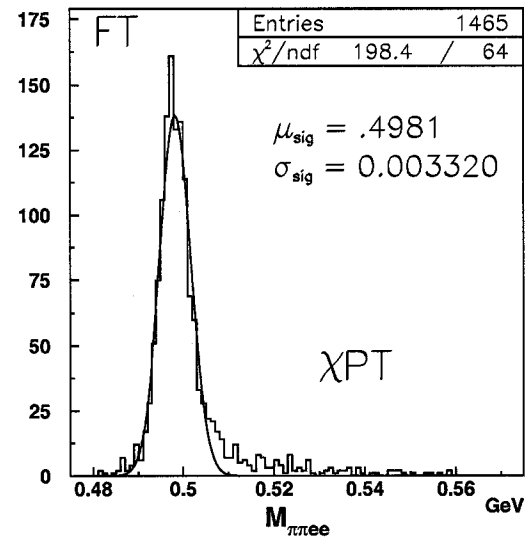
(d) χ PT Model, QT Fitter

Figure 8.7: Gaussian fits to the $K_L^0 \rightarrow \pi^+\pi^-e^+e^-$ Monte Carlo data for each fitter and model are shown. The average of the mean and standard deviation for each fitter type, FT and QT, were used in the fits to the candidate events samples in order to model the background in the signal region.

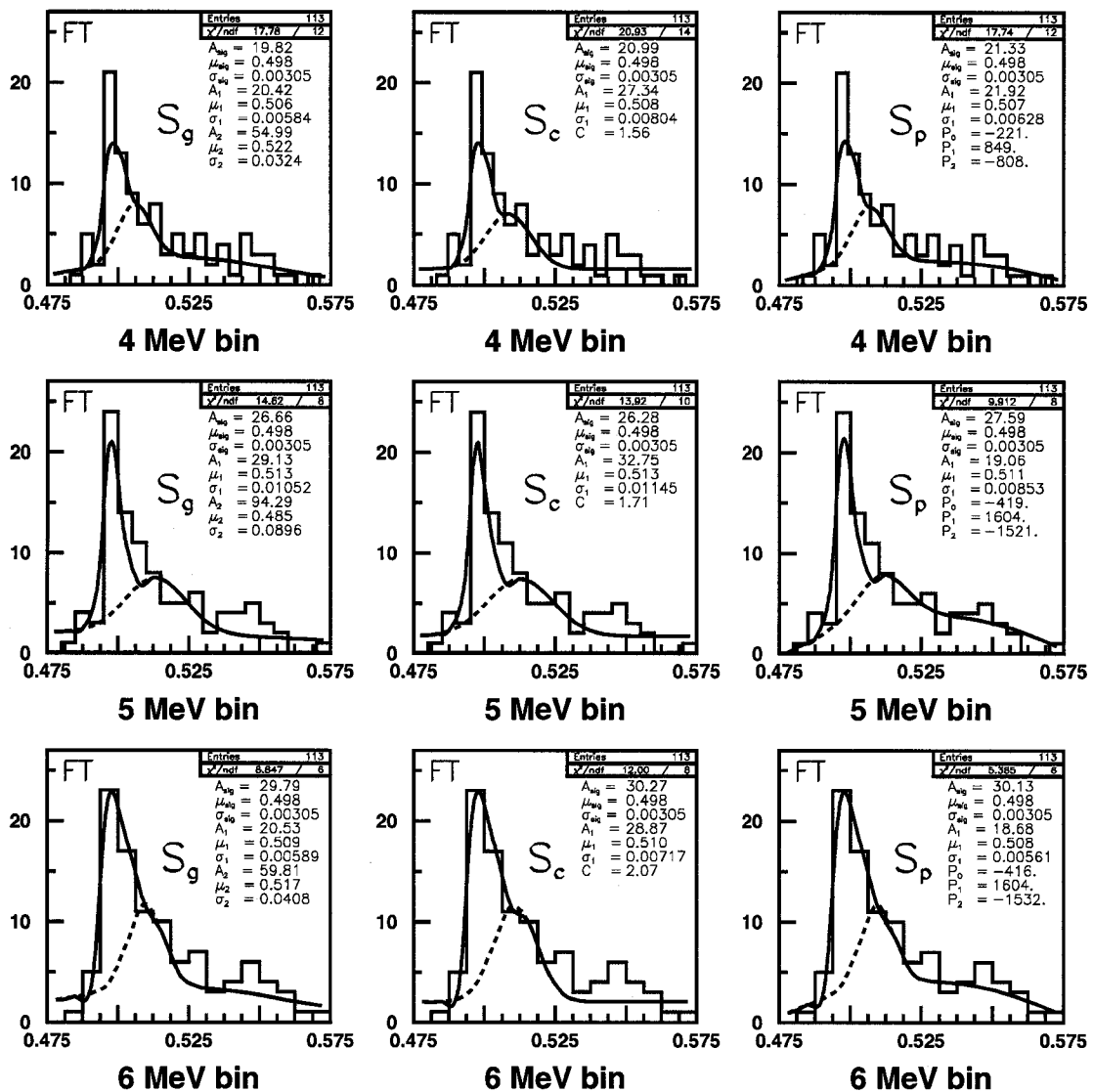


Figure 8.8: The candidate event sample for the FT fitter plotted against four-body invariant mass was fit to the distribution defined in Eq. (8.7). The first bin in each plot starts at 0.475 GeV. The plots in the first, second and third columns use the function S_g , S_c , S_p respectively. The mean and standard deviation were fixed for the signal Gaussian and the peaked-background Gaussian. The bin width for each plot is shown along the x -axis.

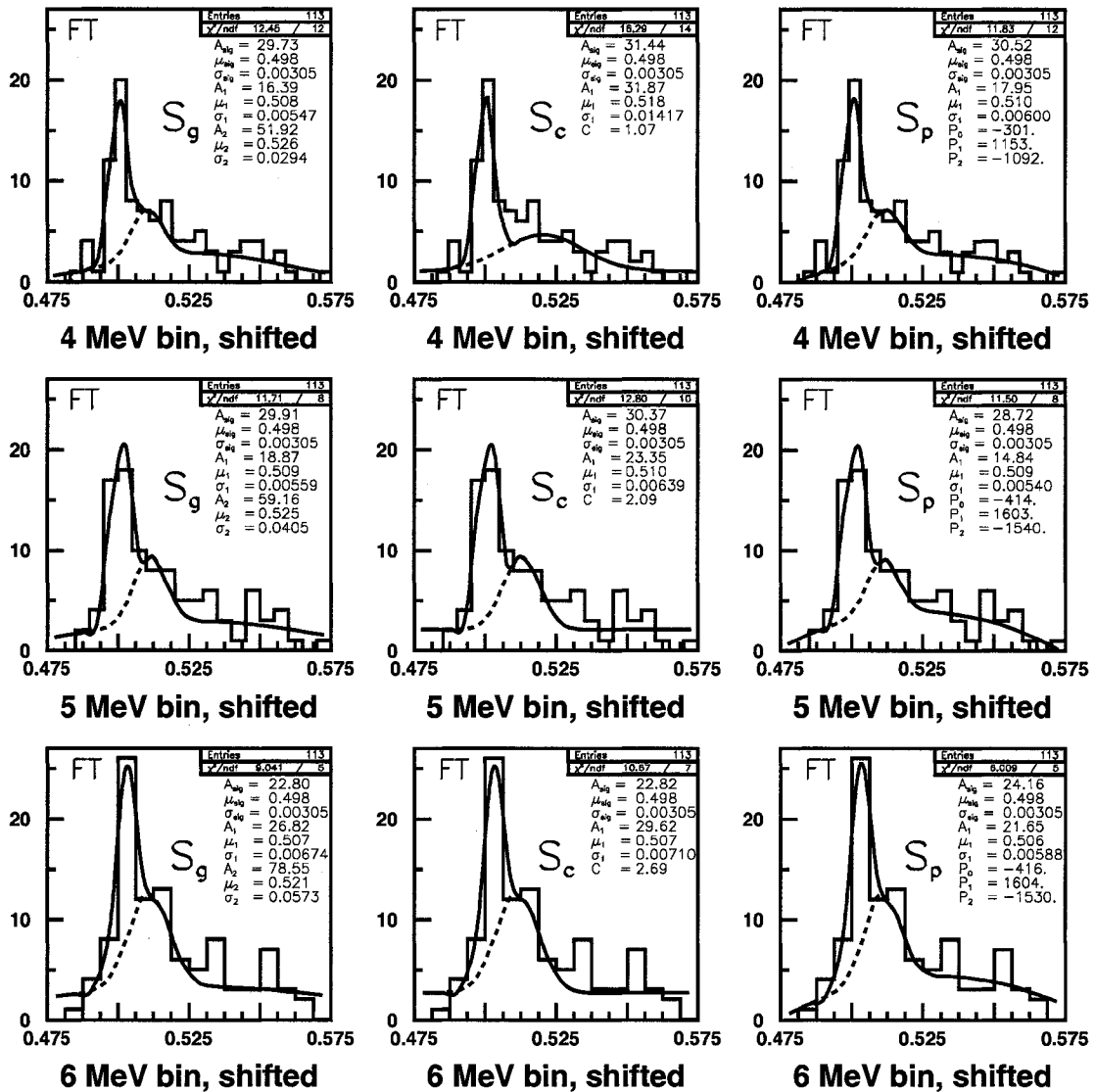


Figure 8.9: The candidate event sample for the FT fitter plotted against four-body invariant mass was fit to the distribution defined Eq. (8.7). The first bin in each plot is shifted by one half of a bin compared to those from Figure 8.8. The plots in the first, second and third columns use the function S_g , S_c , S_p respectively. The mean and standard deviation were fixed for the signal Gaussian and the peaked-background Gaussian. The bin width for each plot is shown along the x -axis.

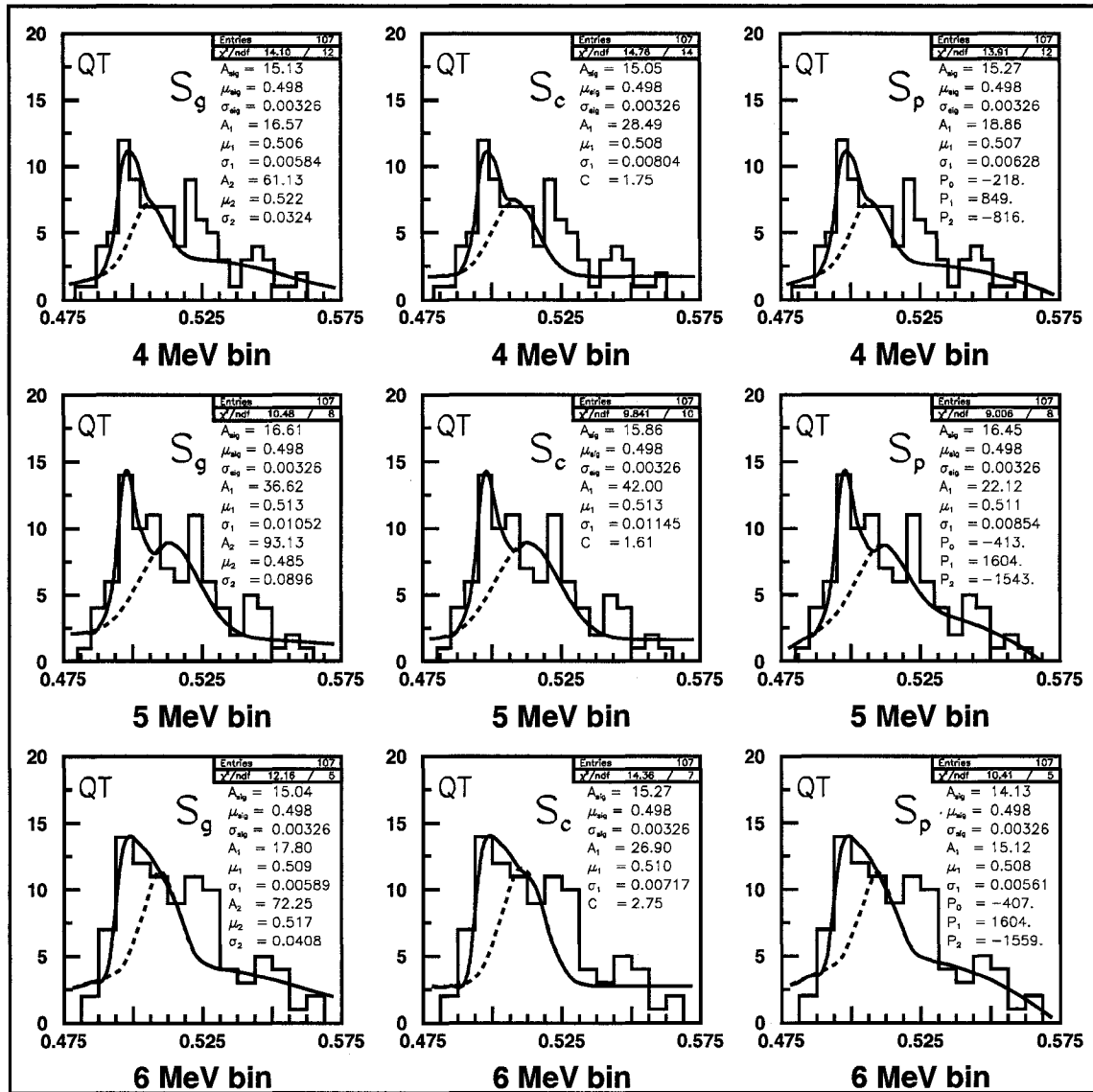


Figure 8.10: The candidate event sample for the QT fitter plotted against four-body invariant mass was fit to the distribution defined in Eq. (8.7). The first bin in each plot starts at 0.475 GeV. The plots in the first, second and third columns use the function S_g , S_c , S_p respectively. The mean and standard deviation were fixed for the signal Gaussian and the peaked-background Gaussian. The bin width for each plot is shown along the x -axis.

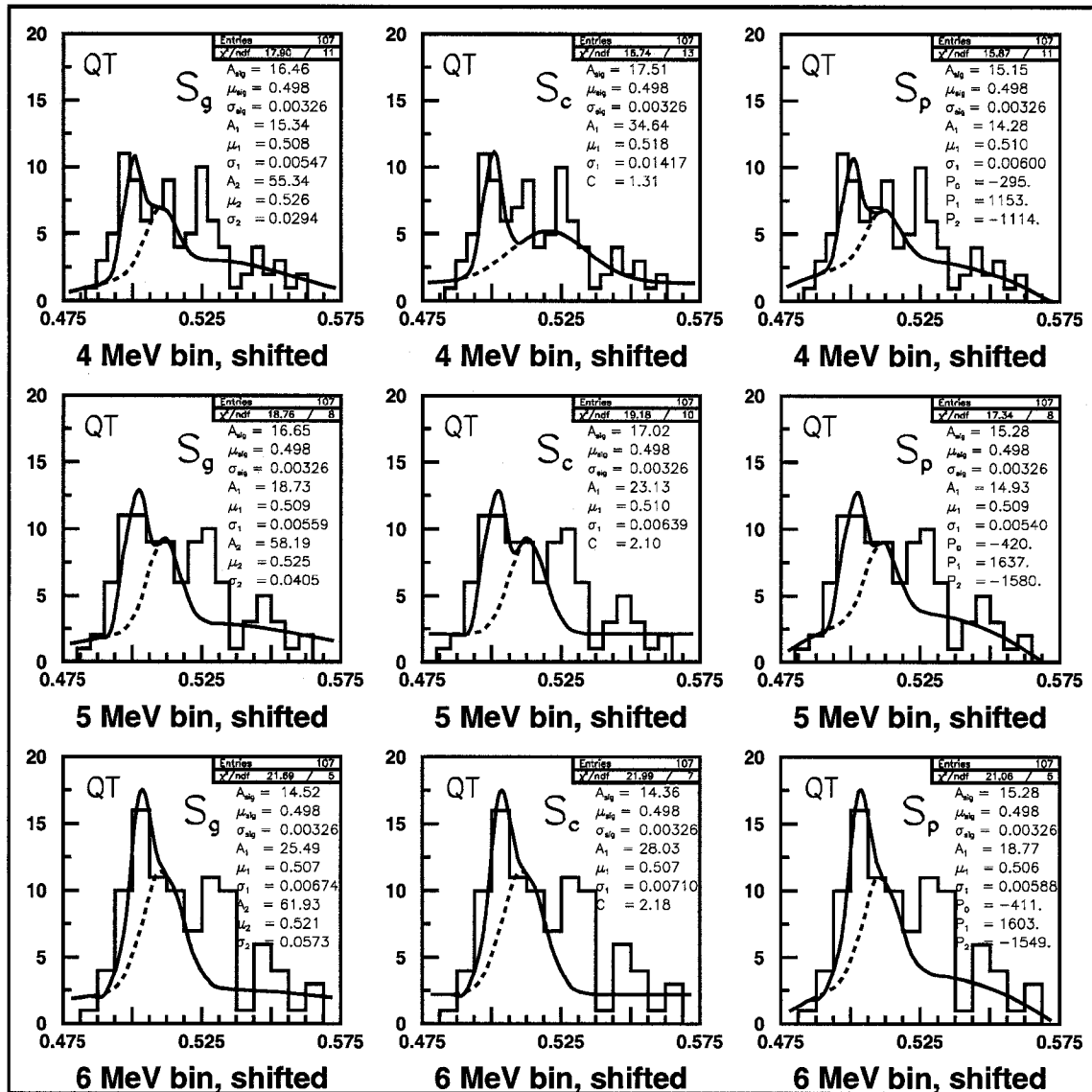


Figure 8.11: The candidate event sample for the QT fitter plotted against four-body invariant mass was fit to the distribution defined in Eq. (8.7). The first bin in each plot is shifted by one half of a bin compared to those from Figure 8.10. The plots in the first, second and third columns use the function S_g , S_c , S_p respectively. The mean and standard deviation were fixed for the signal Gaussian and the peaked-background Gaussian. The bin width for each plot is shown along the x-axis.

| Unshifted histograms | | | FT fitter | |
|---|-------------------------|-------------------------|-------------------------|--------------------------|
| | Fitter types | | | |
| <u>Bin Width</u> | <u>S_g</u> | <u>S_c</u> | <u>S_p</u> | <u>Average over fits</u> |
| 4 MeV | 16.6 | 14.7 | 15.0 | 15.5 |
| 5 MeV | 12.1 | 12.5 | 11.2 | 11.9 |
| 6 MeV | 13.4 | 12.7 | 13.3 | 13.1 |
| Average over bin widths | 14.0 | 13.3 | 13.2 | 13.5 |
| Shifted histograms | | | FT fitter | |
| | Fitter types | | | |
| <u>Bin Width</u> | <u>S_g</u> | <u>S_c</u> | <u>S_p</u> | <u>Average over fits</u> |
| 4 MeV | 11.1 | 8.8 | 11.0 | 10.3 |
| 5 MeV | 11.6 | 11.0 | 11.7 | 11.4 |
| 6 MeV | 18.2 | 18.2 | 16.7 | 17.7 |
| Average over bin widths | 13.7 | 12.7 | 13.1 | |
| Average Number of Background events: $13.3 \pm 7.4(stat) \pm 3.2(sys)$ | | | | |

Table 8.3: The number of background events in the $K_L^0 \rightarrow \pi^+\pi^-e^+e^-$ FT candidate event sample extracted using the fits of Figures 8.8 and 8.9.

| Unshifted histograms | | | QT fitter | |
|---|-------------------------|-------------------------|-------------------------|--------------------------|
| | Fitter types | | | |
| <u>Bin Width</u> | <u>S_g</u> | <u>S_c</u> | <u>S_p</u> | <u>Average over fits</u> |
| 4 MeV | 15.8 | 15.8 | 16.1 | 15.9 |
| 5 MeV | 13.5 | 14.4 | 13.9 | 13.9 |
| 6 MeV | 14.3 | 13.9 | 16.7 | 15.0 |
| Average over bin widths | 14.5 | 14.7 | 15.6 | |
| Shifted histograms | | | QT fitter | |
| | Fitter types | | | |
| <u>Bin Width</u> | <u>S_g</u> | <u>S_c</u> | <u>S_p</u> | <u>Average over fits</u> |
| 4 MeV | 11.3 | 10.1 | 13.6 | 11.7 |
| 5 MeV | 11.4 | 11.0 | 13.5 | 12.0 |
| 6 MeV | 16.1 | 16.3 | 15.0 | 15.8 |
| Average over bin widths | 12.9 | 12.5 | 14.1 | |
| Average Number of Background events: $14.1 \pm 6.6(stat) \pm 2.6(sys)$ | | | | |

Table 8.4: The number of background events in the $K_L^0 \rightarrow \pi^+\pi^-e^+e^-$ QT candidate event sample extracted using the fits of Figures 8.10 and 8.11.

region while 30 of 103 events are in the same region for the QT fitter. These results along with the total number of background events calculated above allow us to calculate the number of $K_L^0 \rightarrow \pi^+\pi^-e^+e^-$ signal events to be

$$FT : N_{\pi\pi ee}^{signal} = 27.7 \pm 7.4(stat) \quad (8.10)$$

$$QT : N_{\pi\pi ee}^{signal} = 16.0 \pm 6.6(stat). \quad (8.11)$$

One possible reason for the large difference between the results of the FT and QT fitters could be from the pileup background fits. The Monte Carlo sample used for the shape of the background was produced using the FT fitter, primarily because of computational restrictions. The 125 events in the pileup background sample was generated using at least half of an 8-node, dual processing cluster continuously for over eight weeks. As seen in Figures 8.10 and 8.11, the background is much more diffuse than its FT counterpart.

CHAPTER 9

Results

9.1 Branching Fraction Measurement

The number of normalization events, their Monte Carlo measured acceptance in the detector, and the world average of the $K_L^0 \rightarrow \pi^+\pi^-$ branching fraction are used to measure the total number of K_L^0 that decay in the fiducial volume of the E871 vacuum tank. The branching fraction of the $K_L^0 \rightarrow \pi^+\pi^-e^+e^-$ decay channel is calculated as the ratio of the number of events observed, corrected by its acceptance in the E871 detector, and the total number of K_L^0 decaying in the vacuum tank as,

$$B(K_L^0 \rightarrow \pi^+\pi^-e^+e^-) = \left(\frac{N_{\pi\pi ee}}{N_{\pi\pi}} \right) \left(\frac{A_{\pi\pi}}{A_{\pi\pi ee}} \right) \left(\frac{\mathcal{L}_{\pi\pi}^{abs}}{\mathcal{L}_{\pi\pi ee}^{abs}} \right) \left(\frac{\mathcal{L}_{\pi\pi}^{\pi decay}}{\mathcal{L}_{\pi\pi ee}^{\pi decay}} \right) R_{eff} B(K_L^0 \rightarrow \pi^+\pi^-) \quad (9.1)$$

where \mathcal{L}^{abs} and $\mathcal{L}^{\pi decay}$ are the likelihoods of a pion to *not* be absorbed in the detector through hadronic interactions and *not* to decay upstream of the trigger scintillating counters, respectively, and R_{eff} is

$$R_{eff} = \left(\frac{\epsilon_{\pi\pi}^{L1}}{\epsilon_{\pi\pi ee}^{L1}} \right) \left(\frac{\epsilon_{\pi\pi}^{L3}}{\epsilon_{\pi\pi ee}^{L3}} \right) \left(\frac{\epsilon_{\pi\pi}^{trk}}{\epsilon_{\pi\pi ee}^{trk}} \right) \left(\frac{\epsilon_{\pi\pi}^{vtx}}{\epsilon_{\pi\pi ee}^{vtx}} \right) \left(\frac{\epsilon_{\pi\pi}^{\mu-id}}{\epsilon_{\pi\pi ee}^{\mu-id}} \right) \left(\frac{\epsilon_{\pi\pi}^{e-id}}{\epsilon_{\pi\pi ee}^{e-id}} \right). \quad (9.2)$$

The ratio R_{eff} includes the efficiencies for the pion tracks in the normalization

and signal samples to pass the Level 1 and Level 3 triggers, the track and vertex reconstruction, and the muon and electron identification requirements. As the primary pions have similar kinematic profiles with the same set of reconstruction selection criteria as applied to the samples, all the ratios in R_{eff} except one are treated as unity. Since the muon identification routines were used to eliminate muon tracks in the $K_L^0 \rightarrow \pi^+\pi^-e^+e^-$ sample but not in the $K_L^0 \rightarrow \pi^+\pi^-$ sample (Chapter 8), the efficiency for a pion to be identified as a muon and removed from the sample must be taken into account. The efficiency ratio term then reduces to

$$R_{eff} = \frac{1}{\epsilon^{\mu-id}}. \quad (9.3)$$

The muon identification efficiency was measured using the $K_{\mu 3}$ decays in the lower sideband of the normalization sample. The events in this set were subjected to the two-body track requirements and electron identification, and were then submitted to the muon identification routines. $K_L^0 \rightarrow \pi^\pm\mu^\mp\nu_\mu$ events having two tracks identified as muons were assumed to have one of the tracks misidentified. Of the 76,205 $K_{\mu 3}$ events, 4176 were identified as $K_L^0 \rightarrow \mu^+\mu^-$ which gives an efficiency in the muon identification routines of $0.945 \pm 0.015(stat)$. This result agrees with those from the thesis of Ambrose [35].

If the probabilities for a pion track to be lost due to decay or absorption in the spectrometer are represented by $P^{\pi decay}$ and P^{abs} , then the likelihoods for the tracks to survive the reconstruction process without undergoing decay or being absorbed due to hadronic interactions are $\mathcal{L}^{\pi decay} = 1 - P^{\pi decay}$ and $\mathcal{L}^{abs} = 1 - P^{abs}$. Both of these processes are dependent on the momentum of the track but are independent of the origin of the pion, whether it be from $K_L^0 \rightarrow \pi^+\pi^-e^+e^-$ or from $K_L^0 \rightarrow \pi^+\pi^-$. As shown in Figures 6.4 and 6.5, the momentum distributions for the pions in $K_L^0 \rightarrow \pi^+\pi^-$ and $K_L^0 \rightarrow \pi^+\pi^-e^+e^-$ decays accepted by the spectrometer have the same shape and are peaked around 2 GeV/c. Due to this similarity, the likelihood

| | FT fitter | QT fitter |
|-----------------------------------|------------------------------------|------------------------------------|
| $N_{\pi\pi ee}$ | 27.68 ± 7.37 | 15.95 ± 6.64 |
| $N_{\pi\pi}$ | 792416 ± 2063 | 784994 ± 2623 |
| $e^{\mu-id}$ | 0.945 ± 0.015 | 0.945 ± 0.015 |
| $B(K_L^0 \rightarrow \pi^+\pi^-)$ | $(1.976 \pm 0.008) \times 10^{-3}$ | $(1.976 \pm 0.008) \times 10^{-3}$ |
| $A_{\pi\pi}/A_{\pi\pi ee}$: | | |
| phenomenological | 115.75 ± 1.00 | 107.39 ± 0.92 |
| model | | |
| χ PT model | 31.60 ± 0.34 | 31.68 ± 0.34 |

Table 9.1: The quantities used in the branching fraction calculations and their statistical uncertainty.

ratios of Eq. (9.1) are taken to be one.

The values used in the branching fraction calculations with their statistical errors are summarized in Table 9.1. From Eq. (9.1), the branching fraction for $K_L^0 \rightarrow \pi^+\pi^-e^+e^-$ was determined to be

$$FT : B(K_L^0 \rightarrow \pi^+\pi^-e^+e^-) = (8.5 \pm 2.3(stat) \pm 1.0(sys)) \times 10^{-6} \quad (9.4)$$

$$QT : B(K_L^0 \rightarrow \pi^+\pi^-e^+e^-) = (4.6 \pm 1.9(stat) \pm 0.8(sys)) \times 10^{-6} \quad (9.5)$$

using the acceptance ratio from the phenomenological model and

$$FT : B(K_L^0 \rightarrow \pi^+\pi^-e^+e^-) = (2.3 \pm 0.6(stat) \pm 0.3(sys)) \times 10^{-6} \quad (9.6)$$

$$QT : B(K_L^0 \rightarrow \pi^+\pi^-e^+e^-) = (1.4 \pm 0.6(stat) \pm 0.2(sys)) \times 10^{-6} \quad (9.7)$$

when the acceptance ratio from the chiral perturbation model is used. The statistical errors were calculated using the sum of the squares of the relative uncertainties in Table 9.1. The error from the number of $K_L^0 \rightarrow \pi^+\pi^-e^+e^-$ events observed dominates these results.

The systematic uncertainty in the branching fraction is due to two sources: the acceptance ratio $\frac{A_{\pi\pi}}{A_{\pi\pi ee}}$, and the fit and bin selection used in the the background extraction from the $K_L^0 \rightarrow \pi^+\pi^-e^+e^-$ candidate event sample. The systematic error in the acceptance ratio can be decomposed into the geometric and reconstruction

efficiency uncertainty in the acceptance ratio of the primary pion tracks and the uncertainty associated with the kinematic reconstruction of the lepton pair. The pion track uncertainty was measured to be 0.97% for the FT fitter and 0.91% for the QT fitter. These errors were taken from the $K_L^0 \rightarrow \mu^+\mu^-$ analysis in [35] in which $K_L^0 \rightarrow \pi^+\pi^-$ events were used as the normalization. In the partial track reconstruction routines, it is assumed that the leptons in the pair share the total momentum available equally. In order to measure the systematic effect of this choice, the $K_L^0 \rightarrow \pi^+\pi^-e^+e^-$ Monte Carlo was reanalyzed using many different momentum sharing hypotheses to a maximum of $\pm 20\%$ asymmetry to determine the effect on the acceptance. The uncertainty in the four-body track cuts was determined by varying the cut by $\pm 10\%$ to measure the effect on the acceptance. The systematic errors for each cut were added in quadrature to the error from e^+e^- momentum sharing error and determined to be 2.93% (phenomenological model) and 3.59% (χ PT model) for the FT fitter while the QT fitter had errors of 2.85% (phenomenological model) and 3.43% (χ PT model). The systematic uncertainty in $N_{\pi\pi ee}$ is due to the method of extracting the background and was determined in Chapter 8 to be 11.50% for the FT fitter and 16.26% for the QT fitter. It is these last effects that dominate the systematic uncertainty in the branching fractions.

Both the FT and QT fitters were used to analyze the $K_L^0 \rightarrow \pi^+\pi^-e^+e^-$ event sample in order to provide a consistency check on the final result. However, the pileup background Monte Carlo was not completed for the QT fitter. The shape of the background determined using the FT fitter was assumed to be the same shape as the background which would be determined using the QT fitter. While this provided a method for extracting a background estimate for the QT data, the validity of such an assumption remains in question. Thus, for this work, the branching fraction

constructed using the FT fitter will be taken as the final result:

$$B(K_L^0 \rightarrow \pi^+\pi^-e^+e^-) = (8.5 \pm 2.3(stat) \pm 1.0(sys)) \times 10^{-6} \quad (9.8)$$

for the phenomenological model and

$$B(K_L^0 \rightarrow \pi^+\pi^-e^+e^-) = (2.3 \pm 0.6(stat) \pm 0.3(sys)) \times 10^{-6} \quad (9.9)$$

for the χ PT model.

9.2 Conclusions

In the signal region $0.4905 < M_{\pi\pi ee} < 0.505$ GeV, 27.7 ± 7.4 $K_L^0 \rightarrow \pi^+\pi^-e^+e^-$ signal events were obtained with a background of 13.3 ± 3.7 events. The signal events were contained in a peak consistent with the characteristics of a Gaussian fit determined through Monte Carlo simulations. The dipion invariant mass for each event was in the region 0.475 GeV $< M_{\pi\pi} < 0.497$ GeV.

The branching fractions, given in Equations (9.8) and (9.9), are model-dependent. The phenomenological model result is in disagreement with the current world average, $B(K_L^0 \rightarrow \pi^+\pi^-e^+e^-) = (3.11 \pm 0.19) \times 10^{-7}$ [19]. The world average comprises a sample of 6175 $K_L^0 \rightarrow \pi^+\pi^-e^+e^-$ events observed in the KTeV and NA48 experiments. In these, the acceptances in the branching fraction measurements were calculated using the phenomenological model. The world average agrees with the theoretically predicted branching fraction and the theoretically predicted dipion invariant mass $M_{\pi\pi}$ spectrum of Sehgal *et al.* [4], [3]. The invariant mass region encompassed by this sample is determined from the experimental acceptance of KTeV and NA48, namely, 0.279 GeV $< M_{\pi\pi} < 0.475$ GeV.

The phenomenological result presented in this work provides the first measurement of the branching fraction for events with $M_{\pi\pi} > 0.475$ GeV but is inconsistent

with the predictions of Sehgal *et al.* [4], [3] and the world average. In order to remove the discrepancy, the model would have to be modified such that the decay rate for the phase space region above 0.475 GeV is increased while leaving the shape of the differential decay rate $\frac{d\Gamma}{dM_{\pi\pi}}$ in the region below unchanged. Such modification would result in the acceptance for $K_L^0 \rightarrow \pi^+\pi^-e^+e^-$ events in E871 to increase, while decreasing the acceptance in the region accessible to KTeV and NA48. The overall effect would then lower the branching fraction measured in E871 and increase that from KTeV and NA48.

The branching fraction presented here using the chiral perturbation model is the first experimentally determined for $K_L^0 \rightarrow \pi^+\pi^-e^+e^-$. The result is inconsistent with the world average, but as noted earlier, the world average is determined by including the phenomenological model. In order for direct comparisons to the results of KTeV and NA48 to be made, the branching fractions for those experiments would need to be determined using the acceptance calculated in χ PT. This can be estimated by assuming that a change in the model would not change the geometric acceptance, but would change the number of K_L^0 that decay in the accepted phase space region. In the phenomenological model, 84.1% of the phase space occurs in the region accepted by KTeV and NA48 while in the χ PT model used in this work, 47.3% of the phase space occurs in that same region. The world average branching fraction in the χ PT model would then be

$$B_{\chi PT}(K_L^0 \rightarrow \pi^+\pi^-e^+e^-) = B_{KTeV}^{NA48}(K_L^0 \rightarrow \pi^+\pi^-e^+e^-) \left(\frac{0.841}{0.473} \right) \quad (9.10)$$

$$B_{\chi PT}(K_L^0 \rightarrow \pi^+\pi^-e^+e^-) = 5.53 \times 10^{-7}$$

The χ PT result from this work, $(2.3 \pm 0.6(stat) \pm 0.3(sys)) \times 10^{-6}$, is 2.6σ away from the world average estimate.

APPENDIX A

E871 Collaboration

D. Ambrose, S. Graessle, G. W. Hoffmann, J. McDonough, A. Milder, P.J. Riley,
J.L. Ritchie, V.I. Vassilakopoulos, C.B. Ware, S. Worm
University of Texas, Austin, Texas 78712

C. Arroyo, K.M. Ecklund, K. Hartman, M. Hebert, G.M. Irwin, M. Pommot-Maia,
S.G. Wojcicki
Stanford University, Stanford, California 94305

M. Bachman, P. de Cecco, D. Connor, N. Kanematsu, R. Lee, W.R. Molzon
University of California, Irvine, California 92697

M. Eckhause, A.D. Hancock, C.H. Hoff, J.R. Kane, Y. Kuang, R.D. Martin, R.E.
Welsh, E. Wolin
College of William and Mary, Williamsburg, Virginia 23187

P.D. Rubin
University of Richmond, Richmond, Virginia 94305

Collaboration Publications

Improved branching ratio measurement of the decay $K_L^0 \rightarrow \mu^+ \mu^-$ [7].

First observation of the rare decay mode $K_L^0 \rightarrow e^+ e^-$ [8].

New limit on muon and electron lepton number violation from $K_L^0 \rightarrow \mu^\pm e^\mp$ decay [9].

A compact beam stop for a rare kaon decay experiment [46].

BIBLIOGRAPHY

- [1] E. Abouzaid *et al.*, Phys. Rev. Lett. **96**, 101801 (2006).
- [2] A. Dolgov and P. L.A., Sov. J. Nucl. Phys. **4**, 262 (1967).
- [3] L. Sehgal and M. Wanninger, Phys. Rev. D **46**, 1035 (1992).
- [4] P. Heiliger and L. Sehgal, Phys. Rev. D **48**, 4146 (1993).
- [5] J. Adams *et al.*, Phys. Rev. Lett. **80**, 4123 (1998).
- [6] A. Lai *et al.*, European Physical Journal **C30**, 33 (2003).
- [7] Ambrose *et al.*, Phys. Rev. Lett. **87**, 1398 (2000).
- [8] D. Ambrose *et al.*, Phys. Rev. Lett. **81**, 4309 (1998).
- [9] D. Ambrose *et al.*, Phys. Rev. Lett. **81**, 5734 (1998).
- [10] A. J. Norman, Ph.D. thesis, The College of William and Mary, 2004.
- [11] R. Belusevic, *Neutral Kaons*, 4th ed. (Springer-Verlag, Berlin, Germany, 1999).
- [12] I. Bigi and A. Sanda, *CP Violation*, 1st ed. (Cambridge University Press, Cambridge, UK, 2000).
- [13] R. H. Dalitz, in *Kaon Physics*, edited by J. Rosner and B. Winstein (University of Chicago Press, Chicago, 2001), pp. 5–21.
- [14] G. Rochester and C. Butler, Nature (London) **160**, 855 (1947).
- [15] C. S. Wu *et al.*, Phys. Rev. **105**, 1413 (1957).
- [16] M. Gell-Mann and A. Pais, Phys. Rev. **97**, 1387 (1955).

- [17] K. Lande *et al.*, Phys. Rev. **103**, 1901 (1956).
- [18] J. Christenson, J. Cronin, V. Fitch, and R. Turlay, Phys. Rev. Lett. **13**, 138 (1964).
- [19] C. Caso *et al.*, European Physical Journal **C**, 010001 (1998).
- [20] H. Burkhardt *et al.*, Phys. Lett. B **206**, 169 (1988).
- [21] V. Fanti *et al.*, Phys. Lett. B **265**, 22 (1999).
- [22] A. Alavi-Harati *et al.*, Phys. Rev. Lett. **93**, 131801 (1999).
- [23] D. Majumbar and J. Smith, Phys. Rev. **187**, 2039 (1969).
- [24] J. Belz, hep-ex/9903025 (unpublished).
- [25] A. Alavi-Harati *et al.*, Phys. Rev. Lett. **86**, 761 (2001).
- [26] E. Abouzaid *et al.*, Phys. Rev. D **74**, 32004 (2006).
- [27] S. Scherer, Adv. Nucl. Phys. **27**, 277 (2003).
- [28] A. Pich, Rept. Prog. Phys. **58**, 563 (1995).
- [29] H. Leutwyler, Ann. Phys. **235**, 165 (1994).
- [30] G. Ecker, ArXiv High Energy Physics - Phenomenology e-prints (1995).
- [31] J. Elwood, M. Wise, and M. Savage, Phys. Rev. D **52**, 5095 (1995).
- [32] M. J. Savage, 4th ed. (Cambridge University Press, Cambridge, UK, 2000).
- [33] H. Pichl, Eur. Phys. J. C **20**, 371 (2001).
- [34] G. Ecker and H. Pichl, Phys. Lett. B **507**, 193 (2001).
- [35] D. A. Ambrose, Ph.D. thesis, The University of Texas at Austin, 1998.
- [36] B. Cousins and T. Kaarsberg, Technical Report No. KL-248, Brookhaven National Laboratory AGS, (unpublished), E871 internal memorandum.

- [37] P. Mèlèse, Technical Report No. KL-145, Brookhaven National Laboratory AGS, (unpublished), E871 internal memorandum.
- [38] R. Lee, Technical Report No. KL-472, Brookhaven National Laboratory AGS, (unpublished), E871 internal memorandum.
- [39] R. K. Lee, Ph.D. thesis, The University of California at Irvine, 1998.
- [40] R. Martin, Ph.D. thesis, The College of William and Mary, 1998.
- [41] P. Skubic *et al.*, Phys. Rev. D **18**, 3115 (1978).
- [42] NIST, Photon Cross Section Database, 2006.
- [43] F. Halzen and A. Martin, *Quarks and Leptons* (John Wiley & Sons, Inc, New York, USA, 1984).
- [44] D. H. Perkins, *Introduction to High Energy Physics*, 4th ed. (Cambridge University Press, Cambridge, UK, 2000).
- [45] R. C. Fernow, in *Introduction to experimental particle physics* (Cambridge University Press, Cambridge, UK, 1986), p. 46.
- [46] J. Belz *et al.*, Nucl. Instrum. Methods **A**, 239 (1999).

VITA

Joshua J. Moss

Joshua J. Moss was born in Pittsburgh, Pennsylvania in March of 1977. After graduating from Penn Hills High School in Penn Hills, Pennsylvania, he attended Hiram College in Ohio where he received a Bachelor of Arts in Chemistry in 1999. In the Fall of that year, he entered graduate school at the College of William and Mary and earned a Masters of Science in Physics in December of 2001. This dissertation was defended on April 6, 2007 at the College of William and Mary in Virginia. He is currently a Postdoctoral Research Associate at The Ohio State University working as part of the ATLAS collaboration at CERN.